Dissertation

Iron deposits in the human post-mortem brain: An electron microscopic study

submitted by

Mariella Sele, MSc, BSc

for the Academic Degree of

Doctor of Medical Science (Dr. scient. med.)

at the

Medical University of Graz

Gottfried Schatz Research Centre
Division of Cell Biology, Histology and Embryology

under the supervision of

Prof. Dr. Gerd Leitinger

2020

Declaration and Disclosures

Declaration: I hereby declare that this thesis is my own original work and that I have fully acknowledged by name all of those individuals and organisations that have contributed to the research for this thesis. Due acknowledgement has been made in the text to all other material used. Throughout this thesis and in all related publications, I followed the "Standards of Good Scientific Practice and Ombuds Committee at the Medical University of Graz".

Graz, October 2020 Mariella Sele

Disclosures:

Parts of this thesis have been published in: Mariella Sele, Stefan Wernitznig, Saška Lipovšek, Snježana Radulović, Johannes Haybaeck, Anna Maria Birkl-Toeglhofer, Christina Wodlej, Florian Kleinegger, Stephan Sygulla, Marlene Leoni, Stefan Ropele and Gerd Leitinger: "Optimization of ultrastructural preservation of human brain for transmission electron microscopy after long post-mortem intervals", *Acta Neuropathologica Communications*, (2019); 7:144. All co-authors have agreed to the inclusion of their published data in the dissertation.

Dedicated to my family
and everyone who believed in me

What doesn't kill you makes you stronger, stronger...
Kelly Clarkson (1)

Danksagung

Ich bedanke mich, bei Prof. Leitinger, dem FWF und der Doctoral School for translational molecular and cellular biosciences für die Möglichkeit an diesem spannendem Project zu arbeiten.
Das Weiteren möchte ich den Mitgliedern meines Thesis Committees, Prof. Stefan Ropele und Prof. Michael Khalil, für die Unterstützung während meiner Dissertation meinen Dank aussprechen. Bedanken möchte ich mich bei den Kooperationspartnern in den Pathologien, den Teams um Prof. Lax und Prof. Haybäck sowie Prof. Gössler, für ihren Einsatz und Engagement in diesem Projekt.
Mein herzlicher Dank geht auch an Prof. Huppertz für seine Unterstützung im Laufe meiner Dissertation. Für ihren Rat und Einsatz möchte ich Prof. Heinemann und Prof. Wadsack meinen herzlichsten Dank aussprechen.
Speziell möchte ich mich bei Rudi und Daniel für ihre technische und persönliche Hilfestellung bei jedem Problem bedanken. Für ihren großartigen Einsatz danke ich auch meinen beiden Masterstudenten Max und Manuel.

Ein ganz spezieller Dank geht an meine Freunde im Büro für die tollen Erlebnisse, aber vor allem für die Aufmunterungen in schwierigen Zeiten.
Für ihre Unterstützung und Freundschaft möchte ich mich wärmstens bei Manuela und Monika bedanken. Aus vollstem Herzen danke ich Elisabeth, Lissi und Stefan dafür, dass sie mir alles, was ich über Elektronenmikroskopie weiß, beigebracht haben, aber vor allem, dass sie solch gute Freunde wurden.

Unendlich dankbar bin ich meiner besten Freundin Nadine mit Chris und Zoey, die eine unverzichtbare moralische und emotionale Stütze und eine Quelle der Inspiration in meinem Leben sind.
Bedanken möchte ich mich auch bei Marc für seine liebevolle Geduld und Unterstützung in dieser herausfordernden Zeit meines Doktorats.
Aus tiefsten Herzen muss ich mich bei meiner Familie, meinen Geschwistern Ramona und Marco, aber allen voran bei meiner Mutter Myriam für die bedingungslose Unterstützung und Liebe bedanken. Ohne euch wäre ich nie so weit gekommen!

DANKE!

List of abbreviations

AFS	Automatic freeze substitution
ATP	Adenosine triphosphate
ATUM	Automated tape-collecting ultramicrotome
BSA	Bovine serum albumin
Ca	Calcium
CCD	Charge-coupled device
CN	Caudate nucleus
CNS	Central nervous system
Cu	Copper
DMT1	Divalent metal transporter 1
DNA	Deoxyribonucleic acid
ECM	Extracellular matrix
EDX	Energy-dispersive x-ray spectroscopy
EELS	Electron energy-loss spectroscopy
ER	Endoplasmic Reticulum
FA	Formaldehyde
Fe	Iron
FGM	Frontal grey matter
FLAIR	Fluid-attenuated inversion recovery (MRI sequence)
FLASH	Fast imaging using Low Angle Shot (MRI sequence)
FS	Freeze substation
FWM	Frontal white matter
GA	Glutaraldehyde
GFAP	Glial fibrillary acidic protein
GP	Globus pallidus
GRE	Gradient echo (MRI sequence)
HAADF-STEM	Aberration-corrected high angle annular dark field scanning transmission electron microscopy
HIP	Hippocampus
HPF	High-pressure freezing
HPM	Hybrid freezing method

ICP-MS	Inductively coupled plasma mass spectrometry
IRE	Iron-responsive element
IRP	Iron-regulatory protein
LAMP	Lysosome-associated membrane proteins
LKH	Landeskrankenhaus
MAP	Microtubule-associated proteins
Mg	Magnesium
MRI	Magnetic resonance imaging
MS	Mass spectrometry
MSA	Multiple system atrophy
NTBI	Non-transferrin-bound iron
OGM	Occipital grey matter
Olig2	Oligodendrocyte transcription factor
OWM	Occipital white matter
p53	Phosphoprotein p53 (tumour suppressor)
pFA	p-Formaldehyde
PGM	Parietal grey matter
Put	Putamen
PWM	Parietal white matter
RN	Red Nucleus
SEM	Scanning electron microscope
SN	Substantia nigra
SNR	Signal-to-noise-ratio
TBI	Transferrin-bound iron
TE	Transposable elements
TEM	Transmission electron microscope
TfR	Transferrin receptors
TGM	Temporal grey matter
Th	Thalamus
TWM	Temporal white matter
Zn	Zinc

Content

Zusammenfassung

Eisen ist für den menschlichen Körper von entscheidender Bedeutung, da es verschiedene wichtige Prozesse wie den Sauerstofftransport, die mitochondriale Energieerzeugung oder die Myelin- und Neurotransmittersynthese nutzt. Ferner ist Eisen mit vielen neurodegenerativen und entzündlichen Erkrankungen verbunden, bei denen ein veränderter Eisenstoffwechsel eine Rolle spielen kann. Es ist auch bekannt, dass sich während der Alterung des Gehirns Eisen in verschiedenen Regionen ansammelt, die mit Alzheimer und Parkinson assoziiert sind. Ferritin ist das wichtigste Eisenspeicherprotein im menschlichen Körper und befindet sich hauptsächlich in Leber und Milz, aber auch in Herz und Gehirn. Das Ferritinpartikel besteht aus einer Kugelschale aus Ferritinproteinen und einem Eisenkern, der bis zu einigen tausend Eisenatomen einschließt.

Das Ziel dieser Studie war es, die zelluläre und subzelluläre Verteilung von Ferritin bzw. seines Eisenkerns im menschlichen Gehirn in Bezug auf Gesundheit und Krankheit zu untersuchen. Mehr Wissen über die zelluläre Verteilung von Eisen im menschlichen Gehirn kann weitere Einblick in die Mechanik gewähren, die diesen belastenden Krankheiten zugrunde liegt. Elektronenmikroskopie kann die notwendige Auflösung liefern, um Ferritinpartikel im Gehirngewebe zu lokalisieren. Mit der energiegefilterten Transmissionselektronenmikroskopie (EFTEM) kann der Eisenkern der Ferritinpartikel in der Probenscheibe sichtbar gemacht werden. Diese Befunde können mit der durch Massenspektrometrie (MS) der einzelnen Hirnregionen bestimmten Gesamteisenmenge verglichen werden.

In einem ersten Schritt wurde die Probenvorbereitung hinsichtlich einer besseren Erhaltung der Ultrastruktur des Gewebes optimiert, die Anzeichen eines Abbaus durch autolytische Prozesse zeigt. Daher wurde eine neue Herstellungsmethode, die Hybrid-Gefriermethode, etabliert. Im frontalen Cortex konnte durchschnittlich eine Eisenpartikelkonzentration von 55.6 und in der entsprechenden weißen Substanz 16.9 Eisenpartikel pro Kubikmikrometer beobachtet werden. In den Basalganglien wurde eine höhere Menge von 208.7 Eisenpartikeln pro Kubikmikrometer im Putamen bzw. 149.7 im Globus pallidus gefunden. Der mit EFTEM ermittelte Eisenwert der analysierten Hirnregion korreliert mit den Ergebnissen der Massenspektrometrie, wenn nur die Mittelwerte berücksichtigt werden. Eine Korrelation der MS-Ergebnisse mit den EFTEM-Eisenwerten war aufgrund der hohen Fehlerabweichung der Methoden schwierig.

Die Anzahl der untersuchten Proben war zu gering, um relevante Schlussfolgerungen hinsichtlich eines veränderten Eisenstoffwechsels bei Alzheimer zu ziehen. Weitere Untersuchungen mit einer höheren Probengröße, gesunden und erkrankten, sind wichtig, um mehr Wissen über die Verteilung und den Metabolismus von Eisen im menschlichen Gehirn zu erlangen.

Abstract

Iron is crucial for the human body as it is used for various important processes like oxygen transport, mitochondrial energy generation, or myelin and neurotransmitter synthesis. Furthermore, iron is associated with many neurodegenerative and inflammatory diseases, where an altered iron metabolism may play a role. In addition, it is known that during brain aging, iron accumulates in distinct regions which are associated with Alzheimer's disease and Parkinson's disease.

Ferritin is the major iron storage protein in the human body and is mostly localised in liver and spleen but also in the heart and the brain. The ferritin particle consists of a globular shell formed by ferritin proteins and an iron core which encloses up to a few thousands iron atoms.

The aim of this study was to research the cellular and subcellular distribution of ferritin, specifically its iron core, in the human brain in health and disease, respectively. More knowledge about the cellular distribution of iron in the human brain may provide more insight into the mechanics which underlie these debilitating diseases.

Electron microscopy can provide the necessary resolution to localise ferritin particles in brain tissue. With energy-filtered transmission electron microscopy (EFTEM), the iron core of the ferritin particles can be visualised in the sample slice. These findings can be compared with the total amount of iron of the individual brain regions determined by mass spectrometry (MS).

In a first step, the sample preparation was optimised regarding a better preservation of the ultrastructure of the tissue showing signs of degradation by autolytic processes. Therefore, a new preparation method, the hybrid freezing method, was established.

On average, in the frontal cortex, an iron particle concentration of 55.6 and in its corresponding white matter 16.9 iron particles per cubic micrometre could be observed. In the basal ganglia, higher amounts of 208.7 iron particles per cubic micrometre in the putamen and 149.7 in the globus pallidus, respectively, were found. The iron scores of the analysed brain region determined with EFTEM correlate with the results obtained by mass spectrometry if only the mean values are taken into account. A correlation of MS results with the EFTEM iron values was difficult to reach due to the high range of observational errors of the methods.

The number of samples examined was too small to draw any relevant conclusions regarding an altered iron metabolism in Alzheimer's disease. Further investigations with a

greater samples size, for both healthy and diseased individuals, are important to gain more knowledge about the distribution and metabolism of iron in the human brain.

1 Introduction

People are progressively reaching higher ages, which poses increasing challenges for society as the incidence of age-related diseases like Alzheimer's or Parkinson's diseases rises dramatically. In the population of over 60 years of age, around 1 – 2 % are clinically diagnosed with either Alzheimer's or Parkinson's disease (1–3). With rising age, the number of people affected by Alzheimer's disease increases significantly to 25 – 45 % in the population over 85 (2,4).

The number of patients with Parkinson's disease has doubled in the last generation and is set to increase in the future, due to people getting older, a longer disease duration, and environmental factors (5). The same pattern can be seen when cases of dementia are observed. From 1990 until the year 2016, the number of people with dementia shows an increase of 117 % up to 43.8 million individuals (6).

Unfortunately, the number one risk factor for neurodegenerative diseases is aging (7,8). To date, there is no preventative measure known for AD and also no effective treatment option is available (9).

1.1 Neurodegenerative diseases

In older people, Alzheimer's disease is the most common form of dementia. It is characterised by two pathological entities, β-amyloid protein deposition and tau hyperphosphorylation.

The exact mechanism is still heavily debated, but it is assumed that metal ions like iron, copper, zinc, and aluminium may also play a role in the disease pathogenesis. Due to alteration of the homeostasis, these metal ions may influence the inclusion of phosphorylated tau proteins in neurofibrillary tangles (NETs) and processes of β-amyloid protein deposition in senile plaques (10). Not just Alzheimer's disease, but other neurodegenerative diseases like Parkinson's disease, multiple sclerosis, dementia with Lewis bodies, and Huntington's disease, too, are characterised by a clinical picture described by insoluble protein aggregations which appear to be colocalised with metals like iron (11,12).

The investigation of the signalling network which regulates these diseases also regarding their connection with the transition metals is crucial for the development of drugs to combat these debilitating diseases.

Currently, a few theories regarding defining factors in neurodegenerative diseases are under investigation. First, it has been suggested that mitochondrial dysfunction play a role (13): As neurons have a high energy demand for their function, any mitochondrial defect would have a strong detrimental effect (14). Zeineh et al. (15) state that in the hippocampus of AD patients, microglia-mediated neurodegeneration occurs, which can be detected with MRI.

Another theory for which increasing evidence emerges is that tau pathology can be transmitted (16) as β-amyloid protein depositions are prions which do not require other cofactors or proteins (17). Prions are distinct strains capable of self-replication producing a unique pattern of neuropathology (18–20).

Detection of structural alteration of various organelles in the neuronal profile is an important research step as those may be caused by neuronal diseases (21–23) and therefore represent a possible target for therapy.

In neurodegenerative diseases, often the mechanisms of cell death are dysregulated (24). A special form of programmed cell death is ferroptosis, which is a leading driver not only in neurodegenerative diseases but also in the neuropathology of major psychiatric disorders (25). In the plasma membrane, the polyunsaturated fatty acids are fatally effected by iron-related lipid peroxidation, which is known as ferroptosis, a special version of programmed death defined by the increase of iron (24,26–28).

It is also know that an excessive amount of intracellular iron directly down-regulates the protein p53, and as a consequence, DNA repair, which is mediated through p53, gets disabled (29). Unfortunately, aging leads to increasing iron levels which further damage the DNA and block its repair. This mechanism is defined as ferrosenescence (30). The epigenome is severely damaged due to ferrosenescence by hypomethylation of the DNA and the mobilization of transposable elements (TE)(30–32).

1.2 Iron in the human brain

For cellular processes in the normal metabolism of the brain, iron is essential, as it is used in vital processes like oxygen transport, mitochondrial energy generation, and the synthesis of DNA, myelin and neurotransmitters (33–36). Iron seems to accumulate while people grow older (37,38) up to an age of 30 years due to an increased requirement during the growth process and then stagnate during healthy adulthood (12,34,39). However, the mechanisms of this iron increase during aging are still unclear (40) but it is known that iron deficiency could lead to cognitive and behavioural changes (41).

An inhomogeneous distribution of iron in the brain can be observed whereas an accumulation can be seen predominately in the basal ganglia, which are associated with motor-functions (38,42,43).

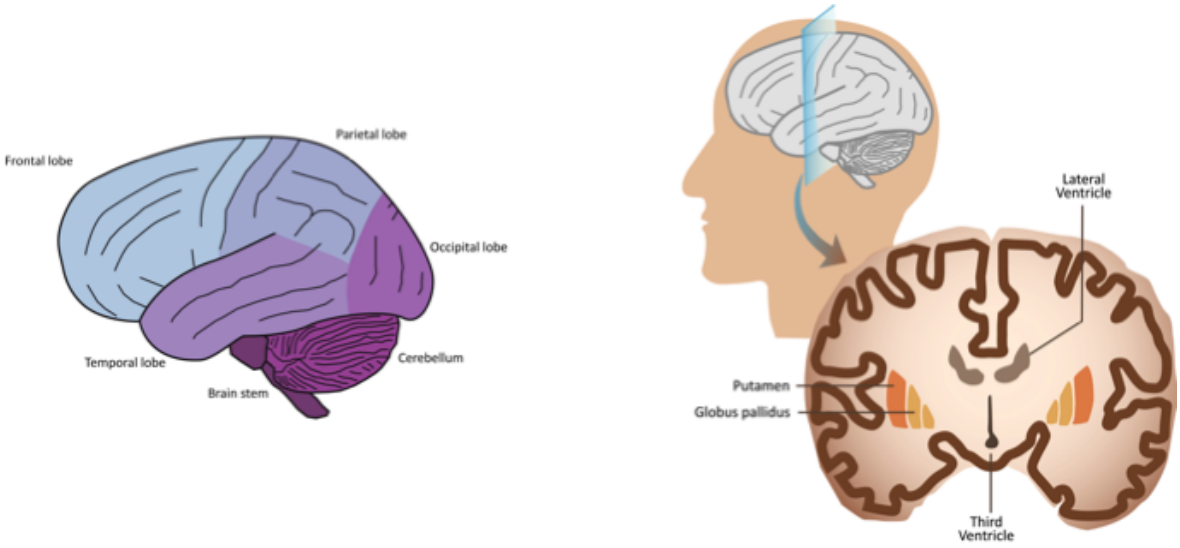

Figure 1: Schematic overview of the different brain regions (left) and schematic display of the brain in the coronal plane to visualise the basal ganglia.

In a study by Wayne Martin et al. (37) with individuals in an age range of 24–79 years, a direct relationship between age and the amount of iron in the putamen (Put) and caudate nucleus (CN) was observed. However, in the globus pallidus (GP) and the thalamus (Th), this connection could not be seen. Great differences in age-related iron content in the putamen could also be seen in a meta-analysis of 20 MRI studies, where the iron amount in the basal ganglia, the red nucleus (RN), and the substantia nigra (SN) were estimated (40). In general, a reliable positive relationship between the iron amount in the basal ganglia and age could be established, whereas the GP showed the smallest difference (40). Already in early adulthood, the iron content in the GP is comparatively high (44), and therefore the enrichment over the remaining lifespan is relatively moderate.

In regions like the basal ganglia and the hippocampus, which are relatively small in volume and have little myelination, a larger amount of iron found in healthy adults (45,46). The aging of a healthy brain is marked by an increase of iron, whereas an excessive accumulation may lead to harmful secondary effects like demyelination and shrinking brain volume (40).

The basal ganglia, consisting of the globus pallidus and the putamen, schematically shown in Figure 1 on the right, are the brain regions with the highest iron content in healthy adults. The globus pallidus has the highest iron concentration with 205 ± 32 mg/kg

followed by the putamen with 153 ± 29 mg/kg (42). Further towards the cortex, the iron concentration declines to 48 ± 14 mg/kg in the frontal white matter and 37 ± 10 mg/kg in the occipital white matter (42). Comparing frontal white and frontal grey matter, Magaki et al. (47) showed that the iron concentration was significantly higher in the white matter than in the grey matter. In a meta-analysis, Schrag et al. (48) did not find any significant difference between an AD group and a control group. It could also be shown that there is a statistically significant difference in the iron concentration between the right and the left hemisphere (42,49) but no gender related differences. In the hippocampus of AD patients, it could be shown that despite an increase in ferritin concentration, the iron concentration did not increase significantly compared to controls (50).

Increased iron level in the brain is suspected to lead to an increased formation of free radicals, which cause oxidative stress and therefore may lead to neurodegeneration (7,37). In addition, some other bioactive metals like copper and manganese have been alleged to play a role in oxidative stress and protein misfolding which may lead to protein aggregation in neurodegenerative diseases (51–53). In a meta-analysis by Schrag et al. (48), several publications published before January 2010 were analysed regarding the amount of iron, zinc, and copper in the neocortical brain regions (hippocampus, frontal, temporal, and parietal lobes) of patients with AD compared to controls. The authors concluded that iron accumulation was not significantly higher in AD patients compared to healthy controls. Only in the putamen (outlier-adjusted), a modest elevation of iron levels of 21.4 % in AD brains could be revealed (48). Furthermore, it was reported not only that the assumption of increased iron levels in AD is a widespread misconception but also that it is a result of a significant citation bias towards the literature claiming an increase (48).

Therapeutic strategies that are targeting iron assume that the accumulation of β-amyloid and therefore the formation of neurofibrillary tangles are facilitated by excessive iron. Despite severe side effects and limitations in long-term application, iron chelators have become a greater focus of interest. A common treatment plan for Alzheimer's disease, despite the lack of robust evidence, is still the interception of metals, especially iron, using chelators (54). While the mechanisms are still heavily discussed, it was described that in case of a systemic iron deficiency or overload, the brain is not overly affected (55,56). Accordingly, it is assumed that the control of iron levels in the CNS is independent from the rest of the body.

Iron in the CNS can be found in the ultrastructure of neurons, astrocytes, and microglia cells, but predominantly in oligodendrocytes (57). In the CNS, oligodendrocytes, counted

among the glial cells, are producing myelin. In the healthy adult brain, they are the cell type with the greatest amount of iron compared to all other cells (58–60). In the white matter, they appear to be organised in rows (61). In the white matter, the iron distribution appears to be organised in patches (60); however, the functional implication is not clear – there appears to be an epigenetic influence (61). In human adults, a continuous maintenance and production of myelin also requires a continuous supply of iron (62). The limitation of iron intake is associated with hypomyelination, which underlines the importance of iron in the myelination process. Interestingly, during development the iron supply of the oligodendrocytes appears to have a temporal aspect, as neurological sequelae still exist despite the fact that iron deficiency in the system is reversed (61). The strong impact of iron shortage on myelination suggests that iron is not only used in the production of lipids or protein but is also important for the metabolism of the oligodendrocytes. The exact mechanism of action of iron deficiency is still unclear. Due to their high demand for energy and ATP, where iron is an essential production factor, the susceptibility to iron deficiency would be explained. In the white matter, it could be seen that microglia begin to accumulate iron before the onset of myelination (60,63). During development, the amount of iron and ferritin in the microglia is higher than in the oligodendrocytes (64). Nevertheless, the iron level in oligodendrocytes remains stable over their lifespan, whereas glial cells show an altered cellular distribution with increasing age (57).

It is proposed that iron, or rather non-transferrin-bound iron (NTBI), enters neurons and astrocytes trough calcium-permeable channels but also through divalent metal transporter 1 (DMT1) and is strongly associated with synaptic activity (65). In neurons, transferrin receptors (TfRs) are expressed at high levels under physiological conditions and can therefore collect a bigger part of iron from transferrin. Commonly, the microglia cells are incorporating the transferrin-bound iron (TBI) with TfRs but also with the dicarboxylic acid receptor as well as presumably the lactoferrin receptor (25). The divalent metal transporter-1 (DMT-19) is upregulated under neuroinflammatory conditions, so that non-TBI can be collected from neurons and glial cells (25). The iron metabolism in the cell is post-transcriptionally controlled by the IRE (iron responsive element)/IRP (iron regulatory protein) system (66–68). In cell culture with reducing condition (like *in vivo*), it could be shown that astrocytes are capable of importing not only Fe(II) but also Fe(III) (69,70). This finding supports the theory that astrocytes are mediating a protective mechanism, as they are able, due to their iron uptake, to buffer the synaptic environment. They are also capable

to enhance this function in the case of neuroinflammatory and neurodegenerative processes (65).

The microglia amount to up to 10-15 % of the glial cells and in the CNS, they are the resident macrophages, which gives them an important role in health and disease in the CNS (71,72). In the various brain regions, the distribution of microglia differs; thus, in the white matter there is significantly more microglia than in the grey mater (73), with an increase in the basal ganglia, SN, the hippocampus, and the olfactory cortex (73,74). Microglia appears to have a central role in aiding the development of oligodendrocytes, and through H-chain ferritin, they may supply the iron for the myelination (61).

1.3 Ferritin and its iron core

The healthy body of a human contains around 4 g of iron, more than half of which is bound in haemoglobin. The rest is located in ferritin, the main iron-storage protein, which is found mostly in liver and spleen, but also in the heart and the brain. In the liver, the iron is distributed nearly homogeneously, whereas in the brain, iron accumulates in distinct structures (41). Nearly all of the non-heme iron, over 90 %, is stored in ferritin (38,40,75). Iron in the striatum, the CN and the Put, is important for neural activity, especially for dopaminergic transmission (7).

The protein ferritin is the main iron-storage protein in the human body. Ferritin has 24 subunits in a 432 symmetry (76), forming a hollow sphere with the capacity to store up to 4500 iron atoms. In vertebrates, the ferritin particle consist of two different subunits, the heavy chain (H-chain) and the light chain (L-chain) subunit, which have different functions (77). In contrast, ferritin isolated from bacteria or plants consists only of the H-chain protein (77). The localisation of the ferritin also changes its configuration, so oligodendrocytes express a combination of heavy and light chain whereas neurons produce predominantly H-chain ferritin and microglia mainly L-chain ferritin (60,78). The light chain subunit of ferritin, which is prevalent in the microglia, is related with iron storage, whereas the H-ferritin contains the catalytic centre and is therefore the dominating subunit in oligodendrocytes and neurons, as these have a high metabolic turnover and iron demand (60,61). As myelination progresses, iron in the oligodendrocytes and the new myelin starts to appear and increase in the temporal process, whereas the concentration of iron in the microglia subsides (64). In an H-ferritin-knockout mouse model, it was shown that H-ferritin is indispensable for life, as the mutation for a complete depletion of H-ferritin turned out to be embryonally lethal (79,80).

In the inner cavity of the ferritin protein shell, the iron atoms are stored as ferrihydrite, which is produced by catalytic oxidation of Fe(II) at the ferroxidase centre in the H-chain. Iron(III) enters the protein as a precursor and is then oxidised with dioxygen or hydrogen peroxide (81,82). With electron microscopy, it could be shown that the diameters of the ferritin-iron cores in the brain (3.5 ± 0.5 nm GP) are smaller than in the liver (6.0 ± 0.5 nm) but also differ in size according to localization in the brain (41). With the aid of aberration-corrected high angle annular dark field scanning transmission electron microscopy (HAADF-STEM), Jian et al. (83) showed that the mineral core in equine spleen ferritin grows like a string of pearls along the inner protein shell. This can lead to half-moon or donut-shaped iron cores. Despite some persisting controversies and mechanisms not being fully elucidated, it is proposed that the iron in ferritin is mobilised through protein degradation in lysosomes (84).

1.4 Electron microscopy

The first transmission electron microscope (TEM) was developed in 1931 by Ernst Ruska, who in 1986 was awarded the Nobel Prize in physics (85) for his ground-breaking invention. Already in 1941, the first biological investigations were carried out with the TEM, when Helmut Ruska could show the first images of bacteriophages. Especially in neuroscience, TEM technologies led to a better understanding of cellular processes, as for instance the organisation of synapses could be investigated (86) or it could be shown that dendrites are sites of synaptic contact (87).

For numerous functional studies of neuronal systems, the high resolution reached by the electron microscope (EM) is essential (88–92). This high resolution is achieved with the use of accelerated electrons under high vacuum directed with electromagnetic lenses, analogous to the visual light and glass lenses of an optical microscope. With the significantly smaller wavelength of the electron beam in relation to the range of visible light, highly magnified images of samples can be generated. The two widely used types of electron microscopes are the transmissions electron microscopes (TEM) and the scanning electron microscopes (SEM). In TEM, the sample needs to be cut ultra-thin, so the electrons can pass through the sample to the detector beneath. By contrast, SEM provides information about the surface of the sample, as electrons which are backscattered or emitted from underneath the surface of the sample are used for imaging. Further information like chemical analysis or a better resolution of the sample can be achieved

with additional correctors, detectors, or filters. With highly aberration-corrected TEMs, resolutions under 50 pm are possible (93).

The transmission electron microscope gave insight into the ultrastructure of the CNS and revealed its complexity (94) as even fine structures like synaptic vesicles or protein aggregations can be visualized. In 1975, Cragg et al. (95) carried out one of the first EM investigations of human cortical synapses in biopsy and post-mortem samples of the frontal and temporal lobes (96). A recent study by Domínguez-Álvaro et al. (97) analysed the morphological alterations of 4722 synapses in AD patients and controls with electron microscopy. In the transentorhinal cortex (TEC) of AD patients, a reduction of the number of synapses that target the spine heads could be observed. In comparison to non-demented people, AD patients showed an increase in the number of fragmented asymmetric synapses.

A totally different approach was developed by Jeff Lichtman, who is not working on the finer detail of the neuronal network but aims to reveal the complete wiring of the mammalian brain, the connectome (98). A connectome has so far only been completely mapped for the nematode *Caenorhabditis elegans* where it consists of 302 neurons and 5000 chemical synapses (99). It is understood that the adult human brain consists of 100 billion neurons and a few trillion synapses (98); nevertheless, a map of circuits in the brain is crucial in order to gain more insight in the transmission of information, how it is physically stored and how diseases alter these structures in the brain. Not only the generation of this huge number of data sets is challenging, but new technologies had to be developed, including serial sectioning techniques like the automated tape-collecting ultramicrotome (ATUM). With this device, thousands of ultra-thin sections on tape can be analysed with a scanning electron microscope (SEM). This technique can be used for large neuronal reconstructions (100) and – with modifications – also for high-throughput image acquisition (101). The handling of big data in EM gains more and more in importance as the images are undergoing a huge increase in number and resolution and therefore in size (102).

With the establishment of cryo-electron microscopy, it became possible to visualise unfixed and unstained vitrified samples that therefore can be investigated in their near-native state. This technique made near-native high-resolution observations of bacteriophages or viruses possible and revealed their structural composition (103). For their development of cryo-electron microscopy, Jacques Dubochet, Joachim Frank, and

Richard Henderson were awarded with the Nobel Prize in chemistry in the year 2017 (104).

1.4.1 Analytical EM

The possibility of analysing the chemical elements in a sample through (analytical EM) was an important step and provided a wide scope of applications in the area of research with biological samples (105–108).

Analytical EM is possible in various forms like energy-filtered TEM (EFTEM), electron energy-loss spectroscopy (EELS), or energy-dispersive X-ray spectroscopy (EDX), to name just a few (see Figure 2).

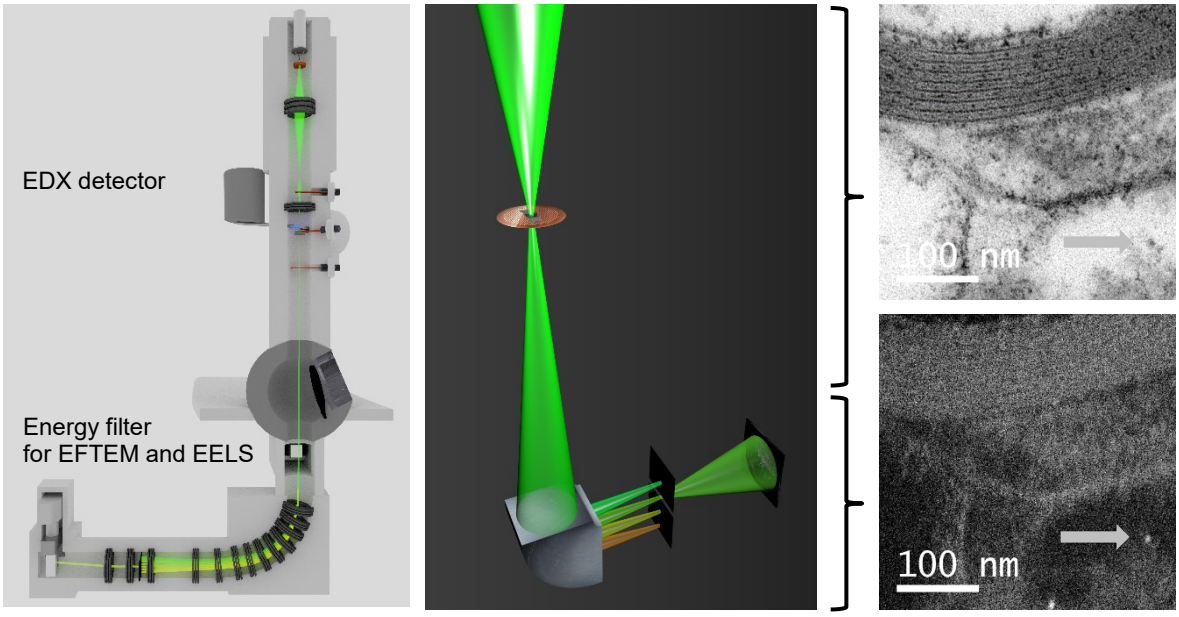

Figure 2: Schematic display of a transmission electron microscope and its beam path (Maximilian Schinagl) and the resulting images (Stefan Wernitznig), reproduced with permission.
Top right: bright field image of human brain tissue, bottom right EFTEM image at iron L edge of the same sample. Grey arrow indicates a ferritin particle in the bright field image as black dot, as the protein shell is more stained than the surrounding cytosol. In the EFTEM image, the arrow indicates the same ferritin particle but the dot is bright, as the measurement at the iron edge gives the localization of iron particles.

Analytical EM can be done with a post-column type filter (also termed magnetic prism) underneath the column of the microscope. When an electron beam hits a thin sample, most of the electrons pass thought the specimen uninterrupted. A few of the electrons are interacting with the sample, resulting in elastic or inelastic scattering. As a result of inelastic scattering, the energy loss of the inner-shell ionization edges, i.e., Fe $L_{2,3}$ reveals chemical information of the atoms in the sample (109,110).

The paths of the electrons are different according to their energy within the magnetic prism in the magnetic sector, which is shaped like an arc. With an energy-selective slit and the help of quadruple and sextuple lenses, the image is focused on the CCD camera (110). With this energy filter, electron energy-loss spectroscopy can be performed, where the interaction of the electron with the sample can be measured through the energy loss of the electrons. Thus the chemical configuration of the sample can be detected (111).

In EFTEM, the chemical information of the EELS is added to the spatial information and results in an elemental map. This is especially important if light elements are investigated of which biological samples mainly consist and which are nearly unavailable with energy-dispersive X-ray spectroscopy. However, one big disadvantage of this method, especially in biological samples, is the beam damage (110). One single EFTEM image cannot be used as a chemical map, as the spectrum always shows a non-element-specific background. Often the three-window technique (111,112) is used to overcome this problem, as the intensity of a quantitative image at a specific excitation edge is proportional to the EELS spectrum intensity. As the name suggests, an image of the scattered electrons is generated at three different energy windows in the spectrum. The non-element-specific background of each pixel in the image is estimated through two images prior (pre-edge) to the element-specific edge. At the element-specific excitation edge, the third image (post-edge) is captured. For each pixel in the image, the estimated background is subtracted from the post-edge intensity and the elemental map results. The intensity of each pixel in these excitation-specific or element-specific image is proportional to the amount of electrons with this excitation energy (110).

The jump-ratio technique, which is calculated from only one pre-edge and one post-edge image, presents an alternative to the three-window technique. As the post-edge image is divided by the pre-edge image, the signal-to-noise ratio is smaller as no background estimation is done. In addition, the image shows fewer drift problems as only two images are used, and they also have a reduced sensitivity to the preserved elastic contrast as this information is lost by the division. The disadvantage of the jump-ratio technique is in general the lack of quantitative information, but it is a good method to distinguish elastic contrast effects from real chemical changes (110).

Aronova et al. (105) adapted the two-window technique by correcting the signal for plural scattering and were able to generate a quantitative EFTEM map of near-physiological calcium concentrations in neurons. In addition to the pre- and post- edge image they also acquired a zero-loss and unfiltered image to estimate the relative thickness of the specimen

in the field of view to correct the intensity for plural scattering in the element-specific range.

1.4.2 Immunolabelling with EM

Labelling of antigens with antibodies can be visualised in the electron microscope by using gold-conjugated secondary antibodies. Atoms with high atomic mass, like osmium or gold, are able to scatter the electron beam strongly, which results in high contrast, so the gold particles attached to the antibody appear as electron-dense or "dark" dots in the image. With this method, the localisation of antigens in the tissue or the cell is combined with high spatial resolution and the possibility of further chemical analysis of the EM.

The sample preparation for immunolabelling is challenging, as the sample has to be fixed and embedded in ways that the ultrastructure is preserved but the epitopes are still recognised by the antibody. Basically, two types of immunolabelling can be distinguished, depending on if the labelling of the sample is done pre-embedding or post-embedding. In the pre-embedding method, the labelling is done before the embedding, while in the post-embedding approach, the labelling is done on sections of the embedded samples. The gold labelling of antigens can be used for relative quantitative determinations, if factors like random systematic sampling with stereological estimation and statistical evaluation of the distribution are considered (113).

Since the method was first described in 1971 (114), countless adapted variants have been established, for example a combination with cryofixation for better labelling rate and structure preservation (115,116).

With immunogold labelling, for example, viral antigens and their position relative to each other like the glycoproteins in the influenza virus can be visualized (117). In another example, one 'hypothetical protein' of the synaptic PSD-95 complex (118) was identified at the postsynaptic density around 33 nm away from the membrane in the forebrain of adult rats (119).

1.5 Post-mortem Interval (PMI)

In histological studies, the focus is on the structure of the tissue and therefore the preservation of the sample has to be perfect for the data to be construed correctly. With a long time lag between the patient's time of death and the fixation of the samples, the autolytic processes are damaging the tissue and the ultrastructure increasingly degenerates the longer the delay. This is especially true for brain tissue as it degenerates very fast due

to the high water content compared to other tissue when human decomposition starts only four minutes after death (120). The accumulation of waste products like lactic acid starts due to the lack of cassation of blood and damages the cell. Furthermore, the reduction of plasma and cytoplasmic pH harms the integrity of the membranes of lysosomes and the cell in general and leads to the release of active endogenous enzymes (121). In organs with a high amount of hydrolytic enzymes and lysosomes, like the liver or the spleen, the autolytic changes occur faster (120,121). Some organelles like the mitochondria are good indicators of the cell condition, as they become elongated and form extensive networks under stress (122), but also they appear to be a defining factor in neurodegenerative disorders like Alzheimer's, Parkinson's, and Huntington's diseases (13,14). A clear attribution of the morphological changes in the ultrastructure to distinctive events becomes even more challenging with an increasing PMI. In comparison to animals which can be easily transported and whose brain can be perfusion-fixed, working with human brain tissue provides often huge logistic challenges, such the fast transport of the corpse to the pathology lab and the autopsy being carried out in a timely manner. In addition, when human samples are used, a delay can occur for ethical reasons (farewell of the deceased). Therefore, it is possible that the time delay, the PMI, can range from a couple of hours to nearly 100 hours (123–127). In this period of time, autolysis goes on despite a slowdown due to the cooling of the corpse and the disintegration of the ultrastructure in the tissue continues. Thus, one main factor for the conservation of the neuronal profile of human brain tissue is the PMI (128). However, a prolonged PMI had little if any effect on the amount of basic protein of the human central myelin (129).

1.6 Sample preparation as a limitation for EM

Sample preparation is the key step in electron microscopy, as the quality of the image depends largely on it. Therefore, various methods, procedures, and equipment have been developed to optimise sample preparation. Electron microscopy can be done at room temperature or at cryogenic temperatures (cryo-electron microscopy), but always requires high vacuum. Accordingly, the samples either have to be dehydrated and embedded in a matrix resistant to the electron beam or frozen in vitreous water to avoid the implosion of the cells and the tissue in high vacuum.

With tissue samples, the standard approach for electron microscopic analyses at room temperature is chemical fixation in a first step after obtaining the tissue. Chemical fixation is mostly achieved with a combination of aldehydes, glutaraldehyde and formaldehyde

(126,130), for the crosslinking of proteins. Often, the sample preparation is followed by post-fixation with osmium tetroxide to stabilise the lipids by binding to conjugated double bonds and also to enhance the low contrast of biological samples that are composed of light elements.

Dehydration with alcohol or acetone to eliminate the water in the sample for embedding in hydrophobic resin is crucial for the preservation of the ultrastructure of the sample. A major part of the lipid extraction happens in this preparation step (131).

Sample preparation heavily depends on the type of analysis required. As for the immunolabelling, the sample had to be fixed very gently so the epitopes of the antigen are still recognised by the antibody. In addition, a more hydrophilic resin has to be used so the antibodies are able to migrate into the slice.

An alternative to the standard chemical fixation is the cryo-fixation (e.g., high pressure freezing, HPF), often used in combination with freeze substitution (FS). The main advantage of high- pressure freezing is the conservation of the near-native structure of the unfixed tissue (132). This has to be achieved without the formation of non-vitreous ice crystals, which would destroy the ultrastructure; this is ensured by the fast freezing rate of the HPM (133,134). The samples in the HPM are frozen by applying 2100 bar and liquid nitrogen, so the vitrification of the sample is faster than the formation of ice crystals.

The preservation of myelin preservation of different animal models with high-pressure freezing in different animal models is excellent (135) in comparison to aldehyde perfusion fixation (136,137).

A crucial step in the processing of the samples regarding the conservation of the ultrastructure of the tissue is dehydration. Temperature and the hydrophilicity of the molecule are the factors that define the size of their hydration shell. This shell keeps the molecules in a non-aggregated state, correctly folded and most notably in aqueous solution. At sufficiently low temperatures, even hydrophobic molecules eventually acquire a hydration shell (138). Dehydration with freeze-substitution is the approach with the least adverse effect on the ultrastructure of the samples thanks to the partially preserved hydration shell at low temperatures. However, the exact mechanisms behind this phenomenon are still not fully understood (139). Diffusion artefacts can also be avoided and the stabilizing compounds in the substitution cocktail can infiltrate the sample slowly and interact when the temperature is slowly raised (139). By using an agitation device during freeze substitution, both substitution and dehydration of the sample are more efficient (140–142). Usually, substitution protocols are time-consuming, but time can be

reduced through an agitation device and still show high contrast even in challenging samples (140–142). HPF and FS and be individual combined and adapted to suit the particular sample and the specific research question. The method can also be used for immunolabelling if the samples are rehydrated ahead of the antibody incubation (116,139). For fluorescence imaging with high en-bloc contrast, Tsang et al. (143) developed a method using a combination of HPF and FS. Other authors combined glutaraldehyde fixation with HPF and observed good preservation of neurons so they could be injected and photooxidised with a fluorophore (144).

1.7 Research question

Since most of the non-heme iron is thought to be stored in ferritin cores, it is postulated that the number of ferritin molecules is higher in brain areas with a high total iron content than in those with low iron content. Furthermore, it is assumed that in samples of patients with Alzheimer's disease, changes in the numbers of ferritins should be observable in the basal ganglia. To verify these postulates, the number of ferritin cores per volume was determined in thin sections of human post-mortem brain samples.

This question was addressed using analytical electron microscopy, as it provides adequate resolution to analyse the distribution of iron stored in ferritin cores in human brain samples at a cellular level. For determining the overall iron content in the brain tissue, mass spectrometry (MS) was applied. For future reference and to relate the ferritin distribution, a magnetic resonance imaging (MRI) iron scan of one hemisphere was carried out.

A major part of this thesis consisted of optimising the sample preparation procedure to determine the number and distribution of ferritins at the ultrastructural level in human post-mortem samples.

With progressing PMI, the ultrastructure of the brain tissue is further degraded. However, tissue preservation is absolutely crucial for the interpretation of the micrographs. Therefore, the preparation procedures of human post-mortem brain tissue for investigation through electron microscopy was optimized. Special attention was paid to improving the preservation of the neuronal profiles beside the myelin sheaths, as long PMIs do not have an effect on the proportion of myelin proteins (129).

With analytical electron microscopy, the number of iron particles and their concentration in the different brain regions was analysed. Furthermore, it was determined if the iron load in the ferritins differed in the different brain regions.

By comparing the ferritin concentration of samples with Alzheimer's disease to healthy

controls, we intended to observe changes in iron regulation. In this regard, the accumulation of copper and zinc in AD was also analysed.

2 Material and Methods

2.1 Human brain tissue

The Institute of Pathology of the Medical University of Graz and the Institute of Pathology of LKH South-West provided small samples taken predominantly from the frontal lobe and the basal ganglia of human post-mortem brains. The samples were included in the study when patients not known to have a neurodegenerative disorder and with no macroscopically detectable lesions were seen. The staging of Alzheimer's disease-related changes in the brain was carried out in accordance with the protocol described by Braak et al. (145). The ethics commission of the Medical University of Graz approved this study (vote 28-549 ex 15/16).

An overview of the human post-mortem samples obtained is shown in Table 1. The acquired tissue was cut into cubes of approximately 1 cm^3 for high-pressure freezing and about 1 mm^3 for standard embedding.

Table 1: Overview of the brain samples of this study

No.	Sample	Year of birth	Sex	PMI [h]	Braak & Braak NFT stage (145)	Comment
1	Fe270217	1945	Male	09:00	I	(146), Case 5
2	Fe171031	1956	Female	15:58	I	(146), Case 1
3	Fe171103	1948	Female	18:05	I	(146), Case 2
4	Fe180206-59	1948	Male	19:50	V	(146), Case 3
5	Fe180206-60	1965	Male	20:55	V	
6	Fe180223	1937	Male	23:40	VI	(146), Case 4
7	Fe180323	1932	Male	20:00	IV	
8	Fe180326	1944	Female	15:30	II	
9	Fe180615	1942	Male	19:00	I	No Putamen
10	Fe181126	1950	Male	14:30	-	LKH West
11	Fe190215	1968	Female	19:00	-	LKH West
12	Fe190314	1946	Male	06:30	-	LKH West

2.2 Sample Preparation for electron microscopy

In Table 2, an overview can be seen of the three different preparation methods for human brain samples for electron microscopy: standard fixation and resin embedding, the newly developed hybrid freezing method with different substitution cocktails, and the preparation for immunolabelling.

Elements of the optimisation process of the sample preparation were published by Sele et al. (146).

Table 2: Comparison of post-mortem brain tissue processing methods for electron microscopy. Parts from (146)

Step	Standard fixation and resin embedding*	Hybrid freezing method (HFM)	High-pressure freezing and freeze substitution	Immunolabelling
1	Prefixed with 2 % formaldehyde + 2.5 % glutaraldehyde in 0.1 M cacodylate buffer for 24 hours at 4 °C		Prefixed with 2 % formaldehyde + 0.1 % glutaraldehyde in 0.1 M phosphate buffer for 24 hours at 4 °C	Prefixed with 2 % formaldehyde + 0.1 % glutaraldehyde in 0.1 M phosphate buffer for 3 hours
2	Vibratome sections at 150 µm, ROI punched out			-
3	Post-fixation with OsO_4 0.1 M cacodylate buffer for 15 minutes at RT			-
4	Washing in 0.1 M cacodylate buffer	High- pressure freezing with hexadecane as cryoprotectant		Washing in 0.1 M phosphate buffer
5	Dehydration in ascending ethanol series	Freeze substitution over 27 hours in different substitution cocktails		Dehydration in ascending ethanol series
6	Intermedium propylene oxide	Washing in acetone		-
7	Resin infiltration with ascending resin series in propylene oxide	Resin infiltration with ascending resin series in acetone		LR White Resin infiltration with ascending resin series in ethanol
8	Resin polymerization at 60 °C for 72 hours in oven			Resin polymerisation at 50 °C for 24 hours in the oven
9	Ultra-thin sectioning at 70 nm and stain grids with lead citrate and platinum blue			
10	Electron microscopic examination of ultra-thin sections			

* For better comparison, the standard resin embedded samples in (146) are also cut with the vibratome

2.2.1 Standard tissue preparation for electron microscopy

For standard embedding, tissue blocks with a size of approximately 1 mm^3 were prefixed with 2 % formaldehyde and 2.5 % glutaraldehyde in 0.1 M cacodylate buffer for three hours at room temperature. Afterwards the samples were postfixed, dehydrated and embedded in TAAB embedding resin (TAAB Laboratories Equipment Ltd, UK) as shown in Table 3. The samples were polymerized at 60 °C for 72 hours.

Table 3: Standard resin embedding for electron microscopy

Step	Substance	Time [h]	Temperature [°C]
Postfixation	2 % OsO_4 0.1 M cacodylate buffer Vibratome sections 1 mm^3 blocks	 0.25 2	RT
Washing	0.1 M cacodylate buffer	2x 0.25	RT
Dehydration	50 % ethanol	0.5	RT
	70 % ethanol	0.5	
	80 % ethanol	0.5	
	96 % ethanol	0.5	
	100 % ethanol	0.25	
	100 % ethanol	0.25	
Embedding	Propylene oxide	1	RT
	Propylene oxide/ TAAB embedding resin (1+1 parts)	3	
	Propylene oxide/ TAAB embedding resin (1+2 parts)	O/N	4
	TAAB embedding resin	1.5	45
	TAAB embedding resin	1.5	45

2.2.2 Embedding for immunolabelling

The samples for immunolabelling were slightly fixed with 2 % formaldehyde and 0.1 % glutaraldehyde in 0.1 M phosphate buffer for three hours at room temperature. Afterwards, the samples were embedded according to Table 4. The tissue samples were put in gelatine capsules for polymerization at 50 °C for 24 hours under oxygen exclusion.

Table 4: Embedding for immunolabelling

Step	Substance	Time [h]	Temperature [°C]
Washing	0.1 M phosphate buffer	2	RT
Dehydration	50 % ethanol	0.25	RT
	70 % ethanol	O/N	4
	80 % ethanol	0.5	RT
	90 % ethanol	0.5	
Embedding	90 % ethanol/LR White resin (1+1 parts)	1	RT
	LR White resin	1	
	LR White resin	1	
	LR White resin	O/N	4

2.2.3 Storage of fixed tissue samples

The human brain samples were prepared with standard embedding at the initial time point. The remaining tissue pieces (~1 mm^3 size) were stored in the buffer used for fixation (0.1 M cacodylate buffer pH 7.4 or 0.1 M phosphate buffer pH 7.4 with sodium azide) at 4 °C. The samples were stored for variable durations as seen in Table 5 and then embedded with the standard method.

Table 5: Storage time of prefixed tissue samples stored in buffer

Tissue samples	Storage time [d]
Fe270217	450
Fe171031	202
Fe171103	197
Fe180206-59	84
Fe180206-60	84
Fe180223	84
Fe180326	47
Fe180323	47

2.2.4 High pressure freezing

With a vibratome (Leica, Austria), the prefixed tissue samples were cut into sections of a thickness of 150 µm. By using a biopsy punch (diameter 4 mm), the region of interest (ROI) was cut out. Afterwards, the ROIs were postfixed for 15 minutes with 2 % osmium tetroxide (Electron Microscopy Sciences, USA) in 0.1 M cacodylate buffer at pH 7.4. The postfixed tissue samples were washed in 0.1 M phosphate buffer and then inserted in a 6 mm diameter aluminium carrier suitable for high-pressure freezing (Engineering Office M. Wohlwend, Switzerland). Either 1-hexadecene or 20 % BSA in bidest. water (Sigma-Aldrich, USA) were used as a filler. The sandwiched tissue was frozen with an HPM100 high-pressure freezer (Leica, USA), with a cooling rate of around 32300 °C per second, dwell time of over 270 ms.

2.2.5 Freeze substitution

For the automated freeze substitution, an AFS2 (Leica, Austria) was used. In addition to the AFS, an agitation device (141) with an operating voltage of 12 V and ethanol as a mediator medium were used to reduce the substitution time. The five different substitution cocktails tested are shown in Table 6. Furthermore, two different temperature programs for the AFS were tested and are shown in Figure 3. The ‘standard’ temperature program holds the temperature (-90 °C, -60 °C, -30 °C) for 8 hours each with a heating rate of 60 °C per hour and 1.5 hours at 0 °C at the end of the program. This results in a total duration of the AFS of 27.5 hours. In the ‘long’ AFS program, -90 °C were held for 48 hours and the samples were warmed up with a heating rate of 4 °C per hour. Including the 1.5 hours at 0 °C at the end of the program, the long temperature program takes 72 hours.

Table 6: Overview of the different freeze-substitution cocktails

	Freeze-substitution media
Cocktail I	2 % osmium tetroxide and 0.2% uranyl acetate in water free acetone
Cocktail II	0.2 % uranyl acetate in water free acetone
Cocktail III	water free acetone
Cocktail IV	0.1 % tannic acid
Cocktail V	1 % water, 2 % osmium tetroxide and 0.2% uranyl acetate in water free acetone

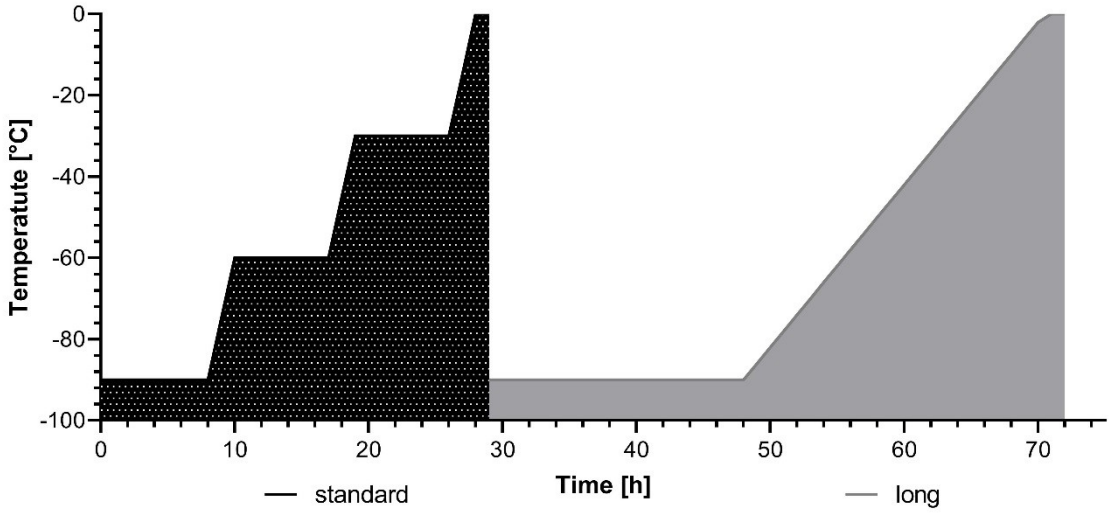

Figure 3: Temperature diagram of the two different AFS

In the substitution with cocktail IV, the sample was exposed to 0.1 % tannic acid during the first eight hours, afterwards carefully washed with cold acetone and the rest of the substitution the samples were in cocktail I. Also tested was a solution of 0.1 % tannic acid, 2 % osmium tetroxide and 0.2 % uranyl acetate in water free acetone.
The samples were carefully taken out of the AFS device and then immediately washed, embedded as described in Table 7, and polymerized at 60 °C for 72 hours.

Table 7: Resin embedding steps after AFS

Step	Substance	Time [h]	Temperature [°C]
Washing	Acetone	3x 0.1	RT
Embedding	Acetone / TAAB embedding resin (2+1 parts)	3	RT
	Acetone / TAAB embedding resin (1+1 parts)	O/N	4
	TAAB embedding resin	2	45
	TAAB embedding resin	2	45

2.2.6 Sectioning

The resin-embedded samples were cut in semi-thin sections of 500 nm, which were stained with 1 % toluidine blue solution (Sigma-Aldrich, USA). This dye was used because it stains the acidic structures like DNA and RNA (147) and it is a specialized method for visualizing myelinated nerve cells (148).

Under the light microscope (Olympus BX63), the region of interest can be selected for trimming. After trimming out the region of interest, the sample was cut in ultra-thin sections of 60 nm on an ultramicrotome (Leica, Austria) and collected on 300 mesh copper grids. Before EM imaging, the sections on the grids were stained with lead citrate and platinum blue, using an Ultrastainer (Leica, Austria). To analyse the sample under the light microscope, one section with a thickness of 500 nm was cut after finishing the ultra-thin sectioning. The section was stained with toluidine blue and cover-slipped.

2.3 EM for ultrastructure analysis

By using the algorithm at https://www.randomizer.org/, the samples were double-blinded to the persons acquiring as well as to those examining the images. An electron microscope, FEI Tecnai G2 20 (Thermo Fischer Scientific, USA), was used at a high tension of 120 kV. From each sample, two sections at three points each an overview image (3x3 images were stitched together) at a magnification of 1 500x (a total of six overview images) were captured with a 2K x 2K CCD camera (Ultrascan 1000, Gatan, USA) and Serial EM software (version 3.6.14, written by David Mastronarde, ©Regents of the University of Colorado). At each of these six acquisition points, three micrographs with a magnification of 6500x were produced using DigitalMicrograph™ software (Gatan, USA), resulting in a total of 18 micrographs at 6 500x magnification for each of the 16 specimens. These images and its analysis were published in (146). With Adobe Photoshop (Adobe Systems, MountainView, USA) contrast and the brightness of the images were adjusted. Parts of these were published in (146).

2.3.1 Energy-filtered transmission electron microscopy (EFTEM)

The FEI Tecnai G2 20 (Thermo Fischer Scientific, USA) is used at a high tension of 200 kV. A Serial-EM script developed by Daniel Kummer and Stefan Wernitznig based on (149) is applied for randomly choosing 10 acquisition points. Each acquisition point of the samples was prepared for EFTEM measuring by 30 minutes exposure to the beam at a magnification of 8 000x. At a magnification of 80 000x, the iron-L-edge EFTEM images were acquired with the 3-window technique: The images were generated with a Quantum 963 GIF (Gatan, USA), a 2K x 2K CCD camera (Ultrascan XP, Gatan, USA) and the following parameters: post-edge at 718 eV, pre-edge 1 633 eV and pre-edge 2 673 eV with a slit of 40 eV and an exposure time of 30 seconds with binning 2. At each of the 10

randomly chosen acquisition points, the field of view was shifted about 0.6 µm in each direction, as is shown in Figure 4. With this approach, 50 images per sample were generated.

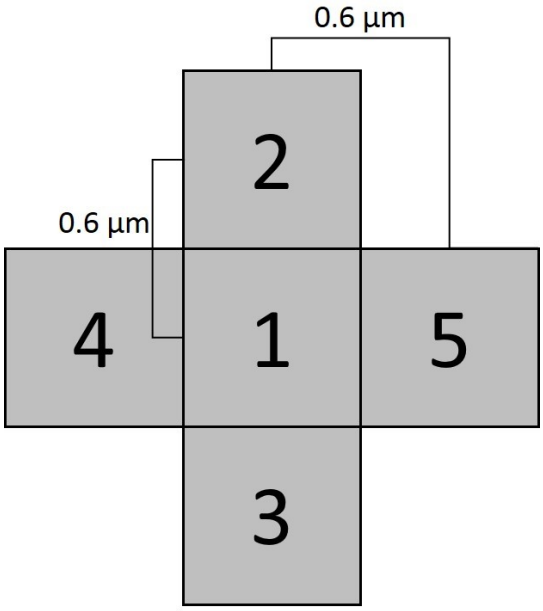

Figure 4: Theoretical EFTEM acquisition pattern

In Table 16, all images used for the evaluation of iron particles are listed. Excluded were images which were not located in the overview image (in overlay) or displayed heavy drift, holes or parts of the grid, as noted in Table 16. The jump ratios were calculated with the post-edge and the pre-edge 2 image in each area.

2.3.2 Immunolabelling of ferritin

The polymerized samples were cut ultra-thin and collected on a 300 mesh copper grid with Pioloform coating. Primary antibodies Anti-Ferritin heavy chain ab81444 from Abcam (Lot ab81444, Abcam, USA) and Anti-Ferritin heavy chain antibody from Bioss (Lot bs-5907R, Bioss, USA) were tested.

As a secondary antibody, anti-rabbit IgG with 10 nm gold (BBI solutions, UK) was used and as a control IgG rabbit c = 15 mg/ml (Lot X0936, Dako, USA). The PBG solution consists of Gibco^{TM} PBS (phosphate-buffered saline, Thermo Fischer, USA) with fish gelatine 0.1 %, 0.1 M glycerine and 0.8 % BSA (bovine serum albumin). The blocking solution consist of 5 % goat serum in PBG with 0.05 % Tween20. The separate steps of the post-embedding immunolabelling process are described in Table 8. Each antibody was

tested in the dilutions 1:10, 1:50, and 1:250. For enhancing the contrast, the samples were stained for 15 minutes with platinum blue and for 7 minutes with lead citrate.

Table 8: Preparation steps of post-embedding imunolabelling

Sample	Negative control	Time [min]
Washing with PBG	Washing with PBG	2x 5
Blocking Solution (goat serum)	Blocking Solution (goat serum)	30
Prim. Antibody	PBG/Tween	120
Washing with PBS	Washing with PBS	4x 5
Sec. antibody	Sec. antibody	60
Washing with PBS	Washing with PBS	4x 5
Washing with bidest. water	Washing with bidest. water	3x 5
Move through bidest. water	Move through bidest. water	-

Further instigations with post-immunolabelling of ferritin in human brain samples were done in the supervised master thesis by Maximilian Schinagl (150).

2.4 Isolation of ferritin

In a first step, ferritin was isolated from pig brain, and after establishing the purification procedure, human brain tissue was used. The isolation was performed in the master thesis by Manuel Hündler that was supervised by the author of this thesis (151).

In a first step, brain tissue was homogenized and ferritins were separated by heat precipitation. In a further step, the protein separation was carried out with a linear glycerine gradient in density-gradient centrifugation. The characterisation of the isolated ferritin particles was undertaken with TEM and negative contrast. On carbon-coated 400 mesh copper grids, 5 µL of the protein suspension was applied and allowed to settle for 1 minute. For negative contrast, the protein on the grid was stained with 5 µL of 1 % uranyl acetate solution for 30 seconds.

2.5 Mass spectrometry (MS)

The chemical analysis of the metals iron, copper, and zinc in the brain samples was performed at the Institute of Chemistry – Analytical Chemistry for Health and Environment at the University of Graz by Prof. Walter Gössler.

The brain tissue was dried until constant mass with a Gamma 1-16 LSC freeze-dryer (Martin Christ GmbH, Osterode am Harz, Germany). The chemical digestion of the samples was carried out in quartz vessels in nitric acid at 250°C for 30 minutes in a

microwave-heated autoclave, UltraCLAVE III (EMLS, Leutkirch, Germany). The elements were determined with an Agilent 7700x inductively-coupled plasma mass spectrometer (Agilent Technologies, Waldbronn, Germany). The iron concentrations were measured at a mass-to-charge ratio (m/z) of 56 using helium as a collision gas to reduce polyatomic interferences. With the certified bovine muscle (RM 8414, NIST), the accuracy of the measured concentration was confirmed.

2.6 Magnetic resonance imaging (MRI)

Prof. Stefan Ropele from the Division of General Neurology at the Medical University of Graz carried out the magnetic resonance imaging of the right hemisphere of the acquired human brain samples.

Magnetic resonance relaxation is affected by the presence of paramagnetic iron. The highest sensitivity has been demonstrated for the transversal relaxation rate R_2^* (= $1/T_2^*$), which shows a linear dependency over the entire physiological range of iron concentration in the brain. R_2^* was assessed in the post-mortem brain samples on a 3.0 Tesla whole body system (MAGNETOM Prisma, Siemens Healthcare, Erlangen, Germany) which is located in the Department of Radiology at the Medical University of Graz. During the measurements, the brain samples were immersed in Galden^{TM} to reduce background signal and unwanted susceptibility artefacts from air bubbles at the surface of the samples. R_2^* mapping was done with a spoiled multi-echo 3D FLASH sequence (TR/FA = 68 ms/20°, echo spacing = 4.9 ms) at an in-plane resolution of 500 μm^2. A high SNR was achieved by using a wrist array coil for signal reception.

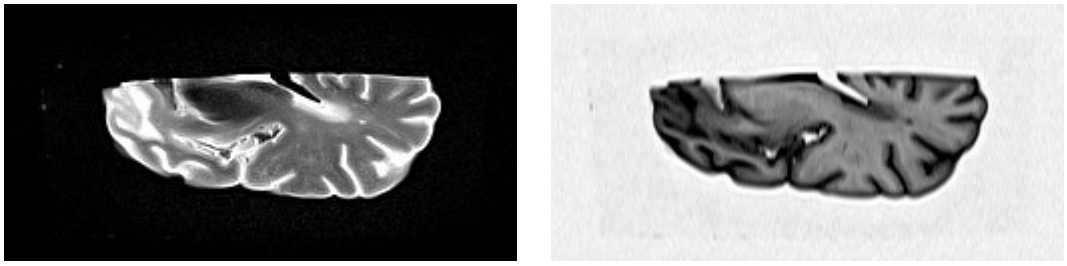

Figure 5: Axial slices from corresponding T_2- (left) and T_1- (right) weighted sequence at the level of the lateral ventricles. Note that only one hemisphere was imaged. Images provided by Prof. Stefan Ropele and reproduced with permission.

Additionally, a fast FLAIR sequence and a T_1-weighted true inversion recovery sequence were acquired for ruling out brain abnormalities and for providing an anatomical reference

for regional analysis. R_2* was obtained by fitting a single-exponential decay function into the signal intensities obtained at the individual echo times in the predefined regions.

The right hemisphere of the human brain samples was used to acquire the magnetic resonance image, see examples in Figure 5 and Figure 6.

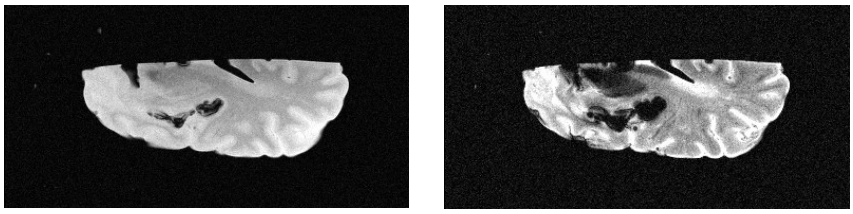

Figure 6: First (left) and last (right) echo of the 3D FLASH sequence. Note the signal intensity drop in the caudate nucleus due to the presence of iron (ferritin). Images provided by Prof. Stefan Ropele and reproduced with permission.

2.7 Evaluation

2.7.1 Statistics

The statistical analyses in this thesis were done with GraphPad Prism (version 8.0.2) and IBM® SPSS® Statistics (version 25). The one-way ANOVAs were followed by a post-hoc analysis (Scheffé) with a significance level of $p = 0.05$. In the box plots, the data are shown with Tukey whiskers. A simple linear regression was used to compare the EFTEM and MS results.

2.7.2 Blinded ultrastructural study

In a double-blinded approach, four different persons rated every sample. The questionnaire used for the evaluation of ultrathin-sections and for semi-thin sections can be found in Table 17 and Table 18.

2.7.3 Evaluation of the myelin sheath thickness (g-ratios)

The g-ratio is the ratio of outer diameter of the myelinated axon (diameter of the myelin sheath) and the inner diameter (diameter of the axon). The g-ratios were analysed with a plug-in (©Ingo Bormuth) for ImageJ (version 1.44, Wayne Rasband, National Institutes of Health, USA), which calculates the ratio on the basis of manually drawn axon and myelin sheath borders, respectively. The software is freeware and available at (http://gratio.efil.de, https://imagej.nih.gov/ij). For each sample (cases 1-4 and cocktails I-III) in all of the six overview montages, 10 axons were randomly selected, drawn and calculated. Parts were published in (146).

2.7.4 Density of myelinated axons in brain tissue

In the overview montages (magnification 1 500x), consisting of nine images with an image size of 129.5 µm², the numbers of myelinated axons in the image were counted. For each of the samples, either five (standard embedding, case 4; cocktail I, case 2) or six images (remaining samples) were used for calculating the density of the myelinated axons. The number of axons per square micrometre is defined as axon density. Parts of this data were published in (146).

2.7.5 Myelin sheath quality

Samples from cases 1-4 were prepared with cocktails I-III as described in (146). With the software ImageJ, a grid of 1024 points with random offset was laid on the 18 images per sample. In addition, a grid consisting of 100 points was tested in one sample.

When a point fell on a myelin sheath, it was categorized in the following three classes: “intact” (blue) – a compact wrapping of the myelin sheath layers can be seen, “disbanded” (cyan) – the myelin sheaths shows space between their single layers, and “unspecified” (green) axons – either insufficient contrast or they were not cut in cross section. Parts of this data were published in (146).

2.7.6 Iron density

A CellProfiler™ (version 3.1.8) pipeline (152) developed in cooperation with Daniel Kummer was used to identify the iron cores of the ferritin in the EFTEM images semi-automatically. The iron map was generated from the 3-window EFTEM images at a magnification of 80 000x and a pixel size of 1 842 px/nm.

The Images are analysed using CellProfiler™ as follows. In a first step, the iron maps are smoothed with a Gaussian filter to reduce noise. Then the object of interest (iron) is identified with the adaptive thresholding method Otsu. The CenterPoints of these objects were used as seeds for an object detection using a watershed algorithm to identify iron objects in a further smoothed image. Objects with an overly large area were excluded and the objects within the right dimensions regarding eccentricity and the maximal and minimal diameter were filtered according to their radial intensity distribution based on Zernike magnitude. The pipeline output consisted of the original iron map, the binary map of the identified object, the overlay of the included and excluded objects with the iron map and the object measurement data. The detailed description of the CellProfiler™ pipeline can be found in Table 19.

2.7.7 Iron distribution

In the free graphic program GIMP (version 2.10.12, © Spencer Kimball, Peter Mattis and the GIMP Development Team), an overlay of the EFTEM images (80 000x) in the bright field overview images (6 500x) was done as seen in Figure 7. When there was overlap between two EFTEM images, one of the two was excluded.

The dimensions of the overview images at a magnification of 6 500 are 8.08 µm x 8.08 µm (5 324 x 5 324 pixel) which results in an area per image of 65.29 μm^2. The EFTEM images and the calculated iron map at a magnification of 80 000 have dimensions of 555.76 nm x 555.76 nm (1024 x 1024 pixel) with an area per image of 0.314 μm^2.

To qualify the number of ferritin cores manually, the jump ratio and the iron map of each location were compared and those ferritins were counted that were clearly visible in both the jump ratio and the iron map.

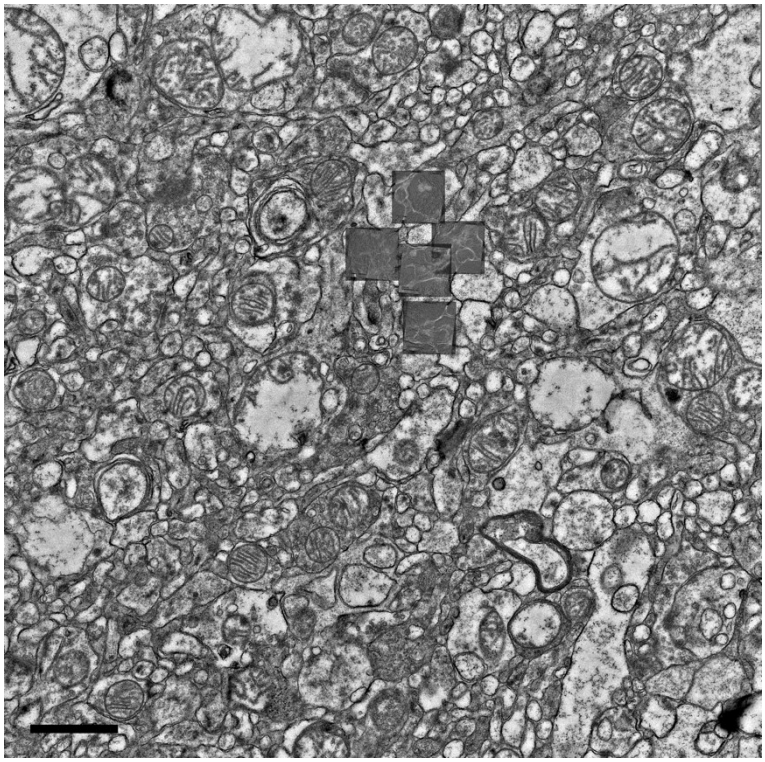

Figure 7: Overlay of bright field overview image (6 500x) with EFTEM images (80 000x); scale bar 1 µm

3 Results

3.1 Sample overview

In total, twelve human brain samples with a PMI range of 6.5 – 24 hours and with Braak & Braak NFT staging from I – VI could be collected. The natural autolysis of the brain tissue dismantled the ultrastructure. For this reason, one main task was the optimisation of the preparation method (standard embedding vs. HFM) to facilitate analysis (e.g. iron with EFTEM) with the electron microscope. Another vital part was the transformation of a visual impression from electron microscopic image into objective numbers.

Not every analysis was done with every brain or brain region; therefore, an overview of the samples is shown in Table 9. The optimisation of the sample preparation was done with samples with a PMI range of 16 – 24 hours to observe changes in the tissue over a longer PMI period. For the analysis of iron particles, samples with the shortest possible PMI (range of 6.5 – 20 hours) were selected. As the ultrastructure dismantles over time and the identification of iron particles became more difficult.

Table 9: Sample overview of all acquired brain samples primarily involved in this study; samples marked with question mark indicate that Braak & Braak NFT staging is still under investigation. The samples labelled with x indicate that analysis was done and minus means that analysis was not carried out.

No.	Sample	Region	PMI [h]	Braak & Braak NFT stage (145)	Myelin quality; p. 57	g-ratios; p. 60	Axon density; p. 59	Iron particle/µm³ (automatic); p. 62	Iron particle/µm³ (manual); p. 62	MS [mg/kg]; p. 69	MRI
1	Fe270217	FGM	9	I	-	-	-	48.9	41.9	36	x
	Fe270217	FWM	9	I	-	-	-	31.8	0.0	76	x
	Fe270217	Put	9	I	-	-	-	153.8	168.8	176	x
	Fe270217	GP	9	I	-	-	-	620.4	529.7	116	x
2	Fe171031	FGM	16	I	x	x	x	34.3	29.7	20	x
	Fe171031	FWM	16	I	x	x	x	32.9	12.6	82	x
	Fe171031	Put	16	I	x	x	x	57.6	39.4	61	x
	Fe171031	GP	16	I	x	x	x	89.0	82.7	91	x
3	Fe171103	FGM	18	I	x	x	x	25.9	15.3	20	x
	Fe171103	FWM	18	I	x	x	x	99.9	4.7	35	x
	Fe171103	Put	18	I	x	x	x	206.4	213.8	60	x

	Fe171103	GP	18	I	x	x	x	18.8	5.5	40	x
4	Fe180206-59	FGM	20	V	-	-	-	-	-	-	x
	Fe180206-59	FWM	20	V	-	-	-	-	-	-	x
	Fe180206-59	Put	20	V	-	-	-	-	-	-	x
	Fe180206-59	GP	20	V	-	-	-	-	-	-	x
5	Fe180206-60	FGM	21	V	-	-	-	-	-	-	x
	Fe180206-60	FWM	21	V	-	-	-	-	-	-	x
	Fe180206-60	Put	21	V	-	-	-	-	-	-	x
	Fe180206-60	GP	21	V	-	-	-	-	-	-	x
6	Fe180223	FGM	24	VI	x	x	x	-	-	108	x
	Fe180223	FWM	24	VI	x	x	x	-	-	51	x
	Fe180223	Put	24	VI	x	x	x	-	-	147	x
	Fe180223	GP	24	VI	x	x	x	-	-	167	x
7	Fe180323	FGM	20	IV	-	-	-	22.5	14.3	33	x
	Fe180323	FWM	20	IV	-	-	-	22.7	3.8	45	x
	Fe180323	Put	20	IV	-	-	-	291.9	265.4	189	x
	Fe180323	GP	20	IV	-	-	-	143.8	112.8	55	x
8	Fe180326	FGM	15.5	II	-	-	-	109.8	60.4	28	-
	Fe180326	FWM	15.5	II	-	-	-	62.2	12.1	53	-
	Fe180326	Put	15.5	II	-	-	-	82.0	45.8	144	-
	Fe180326	GP	15.5	II	-	-	-	59.4	38.2	-	-
9	Fe180615	FGM	19	I	-	-	-	-	-	22	-
	Fe180615	FWM	19	I	-	-	-	-	-	23	-
	Fe180615	-	19	I	-	-	-	-	-	-	-
	Fe180615	GP	19	I	-	-	-	-	-	144	-
10	Fe181126	FGM	14.5	?	-	-	-	40.2	24.4	22	-
	Fe181126	FWM	14.5	?	-	-	-	62.2	31.8	23	-
	Fe181126	Put	14.5	?	-	-	-	614.0	545.1	122	-
	Fe181126	GP	14.5	?	-	-	-	64.1	2.2	272	-
11	Fe190215	FGM	19	?	-	-	-	-	-	35	-
	Fe190215	FWM	19	?	-	-	-	-	-	48	-
	Fe190215	Put	19	?	-	-	-	-	-	78	-
	Fe190215	GP	19	?	-	-	-	-	-	59	-
12	Fe190314	FGM	6.5	?	-	-	-	271.3	203.5	25	x
	Fe190314	FWM	6.5	?	-	-	-	183.4	53.1	52	x
	Fe190314	Put	6.5	?	-	-	-	267.7	182.3	91	x
	Fe190314	GP	6.5	?	-	-	-	382.9	276.8	38	x

3.2 Optimisation of sample preparation

Sample preparation for electron microscopy varies widely with regard to the requirements of application and the sample properties.

The standard in-house embedding method consists of chemical prefixation with aldehydes, postfixation with osmium tetroxide, dehydration with ethanol, and embedding in an epoxy resin named TAAB embedding resin. This standard method was intended to be optimised, given that for the localisation of iron or ferritin particles, the preservation of the ultrastructure of the tissue needs to be as good as possible. Different combinations of pre-, post- and cryofixations as well as different substitution variants were therefore tested. All variations of the embedding method were compared to the standard embedding method. Parts of the optimisation procedure for sample preparation were published in Sele et al. (146).

3.2.1 Chemical prefixation

Samples from the same brain tissue were prefixed either with a hard mixture with more glutaraldehyde (GA) or with a soft mixture that contains little GA. In addition to the GA, both fixation media contained the same amount of formaldehyde (FA). In both samples, the individual wrappings of the myelin sheaths can be identified, see Figure 8.

The tissue prepared with the soft fixation medium with 0.1 % glutaraldehyde showed fewer preserved myelin sheath, as parts of the myelin sheaths appeared to have been torn out. In a general impression, the sample displayed a rather washed-out look with fewer details visible in the ultrastructure compared to the ones fixed with the hard medium. They also appeared to have less contrast than the hard-fixed ones, which further underlines the washed-out look of the softly-fixed samples. The hard-fixed brain tissue samples showed more intact myelin sheaths and details like microtubules in the axon could be seen more clearly. The myelin sheaths in the sample with only 0.1 % GA in the fixation medium had missing parts which appeared to be ripped out. On these grounds, the human brain tissue samples were subsequently prefixed with 2 % FA and 2.5 % GA.

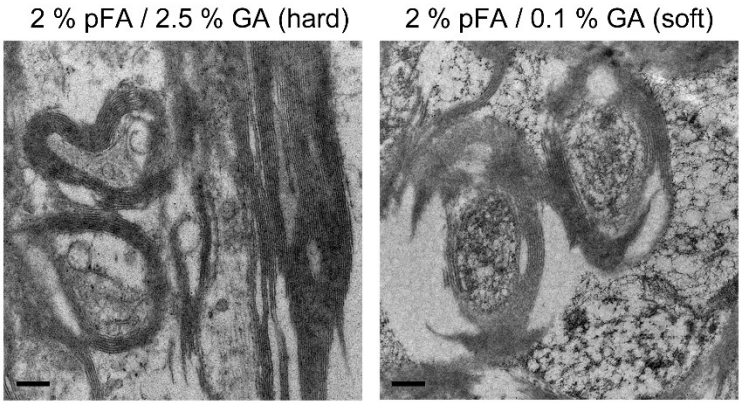

Figure 8: Comparison between the two different tissue fixation media, sample Fe270217;
Left: The sample prefixed with the higher concentration of glutaraldehyde showed fewer gaps in the wrapping of the myelin sheaths than the sampled fixed with less GA on the right side. Both fixation media contained the same amount of FA. Scale bars 0.2 µm

3.2.2 Postfixation

For further stabilisation of the ultrastructure, predominantly the myelin sheaths with their high content of lipids, postfixation with osmium tetroxide, a cross-linker for lipids, was tested. Therefore, samples postfixed before cryofixation were compared to the non-postfixed samples. It was revealed that postfixation is a key factor in the optimisation of the preservation of the myelin sheaths in the neuronal tissue, as can be seen in Figure 9.

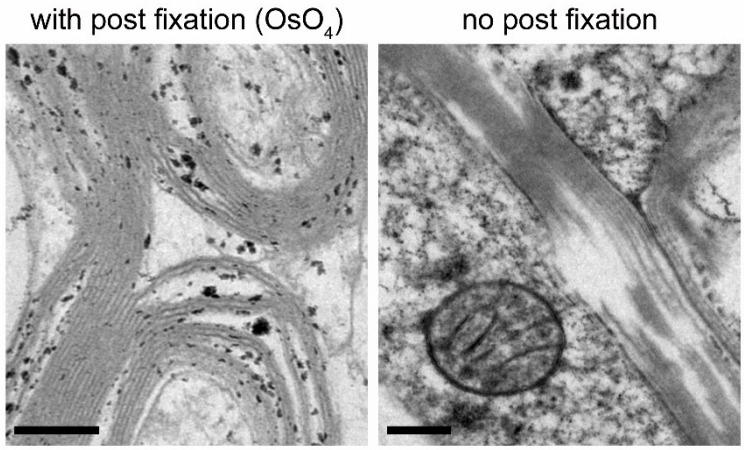

Figure 9: Electron microscopic images of the human brain sample Fe270217 prepared with and without osmium trioxide as post fixation before cryo-fixation with HPF (146).
In the sample with postfixation displayed on the left side, the individual layers of the myelin sheaths are clearly visible, compact, and have only minor gaps compared to the sample displayed on the right. However, protein with good accessibility displayed stronger staining, clearly visible in the left image. The samples were both processed with the substitution cocktail I. Scale bars 0.2 µm

The particular layering of the myelin sheaths can be easily recognised, displayed on the left side of Figure 9. In the right panel, the myelin sheaths of the non-postfixed samples have

missing or ripped-out parts compared to the compact ones of the postfixed samples. Therefore, the neuronal tissue subsequently was prefixed with a high amount of GA and afterwards postfixed with osmium tetroxide for better preservation of the myelin sheaths.

3.2.3 Filler substance

After fixation (pre- and postfixation), the samples are high-pressure frozen. The carriers of the HPM100 are filled with the fixed sample and an inert filler substance to displace air. As filler substances, both a 20 % BSA solution as well as 1-hexadecene were tested, see Figure 10.

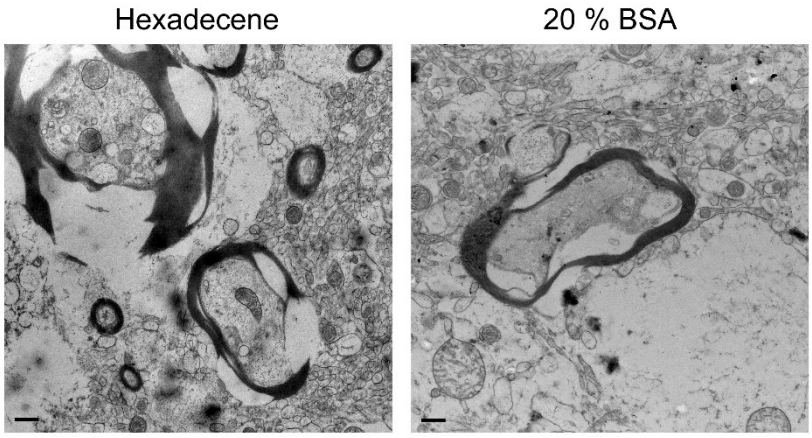

Figure 10: Comparison of the same sample (Fe270217) high-pressure frozen with two different filler substances. In the left panel, the sample displayed was prepared with hexadecane, and better detail preservation can be seen, whereas in the right panel, after using BSA, the structures appeared to be washed out and showed lower contrast. Scale bars 0.5 µm

The samples frozen with either filler substance showed disbanded and damaged myelin sheaths, albeit the preparation with hexadecene appeared to have slightly more contrast. Furthermore, hexadecene was more agreeable in handling and application.
Thus, subsequently hexadecane was used as a filler for high-pressure freezing of fixed brain samples.

3.2.4 High-pressure freezing (HPF)

Usually cryofixation, e.g. high-pressure freezing, is done with native tissue (without fixation and postfixation) to maintain the original tissue ultrastructure without any artefacts (e.g. cross-linking of proteins or lipids due to fixation). However, due to the softness of the brain, especially for tissue with longer PMI, prefixation was necessary to be able to cut a piece to size suitable for HPF.

3.2.5 Freeze substitution (FS)

Dehydration in organic solvent (acetone) was carried out at cryogenic temperature in a so-called freeze-substitution process. During this process, the high-pressure frozen samples have to be gently warmed up without damage to the tissue ultrastructure for embedding at room temperature. The warm-up was done with automated freeze substitution (AFS). For the optimisation of this preparation step, different temperature programs and agitation devices (here usually to speed up to enhance affectivity of substitution) were tested. Furthermore, various substitution cocktails were investigated regarding the effect on the preservation of the ultrastructure, especially the myelin sheaths.

3.2.5.1 Temperature program

The frozen samples were either processed with the in-house standard AFS temperature program, where the temperature increase was staircase-shaped with a total duration of 27 hours, or with a longer version, with a long dwell time in the beginning and an isocratic increase of the temperature, which resulted in a total duration of 72 hours. The details of the temperature programs are described in Figure 3.

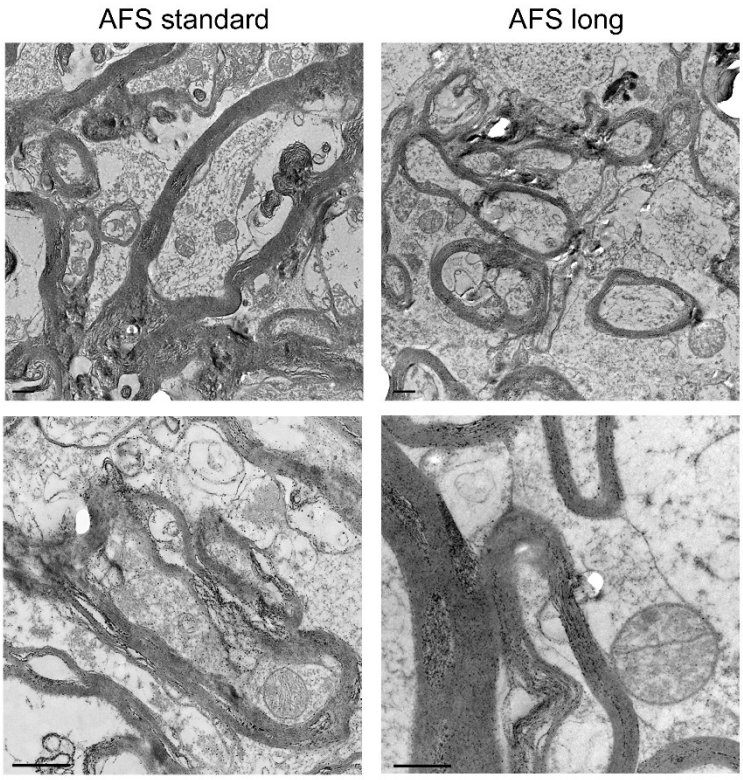

Figure 11: Comparison of high-pressure frozen samples (Fe270217) with the same substitution cocktail but one with the standard FS temperature program and once with a long version. Left column: sample prepared with the standard AFS with 2 500x and displayed beneath. In the right column, images of the sample processed with the long AFS and 6 500x beneath. Scale bars 0.5 µm

The finer structures like microtubules in the axon are more clearly visible in the standard AFS than in the extended version. In addition, the layers of the myelin sheaths become slightly more apparent in the standard version. Hence, the timesaving standard AFS temperature program was used subsequently.

3.2.5.2 Agitation

Cryosubstitution is usually a time-consuming step in the sample preparation, and sample agitation is known to enhance this step (153). The high-pressure frozen brain samples were prepared with a magnetic force-driven agitation module that can be inserted in the cryochamber of the automated freeze substitution device (140–142). The 24 V motor of the device, through free rotation of the rotor blade with its magnets and the sample tube holder with a magnetic element on top, allows the frozen samples in the substitution cocktail to be in motion (140).

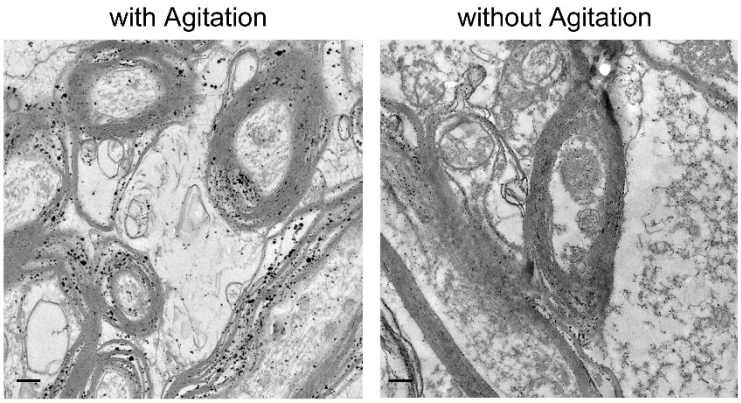

Figure 12: Electron micrographs of the sample Fe270217 prepared with substitution cocktail I with and without the use of an agitation module. In the sample prepared with the agitation device (left side), the individual layers of the myelin sheaths appeared to be better preserved than in the preparation without the usage of the agitation device (right side). The proteins with good accessibility showed stronger staining. Scale bars 0.2 µm

The samples prepared with the FS under agitation can be seen in Figure 12 on the left. It can be characterised with an increase in distinguishability of the finer structures like the filamentous material in the pre- and postsynaptic zone with its vesicles and protein complexes. Further, the membranes appear to be uninterrupted, smoother, and with higher contrast, especially the membranes forming the synaptic vesicles.

3.2.5.3 Substitution cocktails

Different substitution cocktails (I-V, described in detail in Table 6) were tested with the aim of improving the quality of tissue preservation. The two cryosubstitution cocktails, cocktail IV with tannic acid and cocktail V with water added to cocktail I, showed no decisive improvement in the structural preservation of the neuronal tissue. Therefore, only cocktails I-III and the standard resin preparation were compared in a systematic and comparable manner to elaborate the method with the best ultrastructural preservation of the brain samples.

The ultrastructure of the brain tissue is dismantled over time due to irreversible natural autolysis, but what is left needs to be preserved as effectively as possible. Therefore, a key factor is the post-mortem interval of the brain tissue. The myelin sheaths appeared to be a structure that degrades relatively late in the autolysis; hence the focus of the structural analysis was laid there.

In preliminary tests, water and tannic acid were added to the substitution cocktail as is often recommended for neuronal tissue. Micrographs of the so prepared samples are displayed in Figure 13. In the sample substituted with tannic acid in the cocktail, the myelin sheaths showed huge gaps in their wrapping. Overall, the finer structures were not clearly visible and in total the ultrastructure gave a washed-out appearance. However, the contrast was satisfactory, especially compared to the preparation with cocktail V, Figure 13 right side. Therefore, both cocktails were not tested any further, as they showed no improvement regarding tissue preservation.

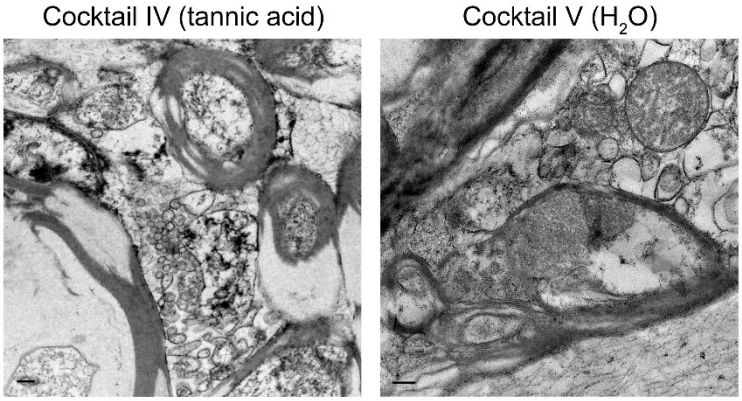

Figure 13: Preliminary test with tannic acid (cocktail IV) and water (cocktail V) added to the freeze-substitution cocktail. Tissue of the frontal white matter of specimen Fe270217 was processed with cocktail IV with contained tannic acid (left side); the myelin sheaths showed gaps but the contrast in the sample was satisfactory. The samples prepared with cocktail V which contained water (right side) did not show improved preservation of the myelin sheath and the contrast was low. Scale bars 0.2 µm

The samples prepared with the HFM, cryofixation, of postfixed samples and cryosubstitution with cocktail I, appeared to preserve the tissue best (compare Figure 14 A-D and Figure 14 E-H). Further, with respect to standard embedding, the samples prepared with cocktail I generally showed a considerably improved quality of myelin sheath preservation regardless of the PMI.

Although the myelin sheaths showed remarkable resistance against autolysis even in samples with longer PMIs, the condition of the finer ultrastructural details appeared to be more sensitive to the PMI; an illustrative example are the microtubules in the axons.

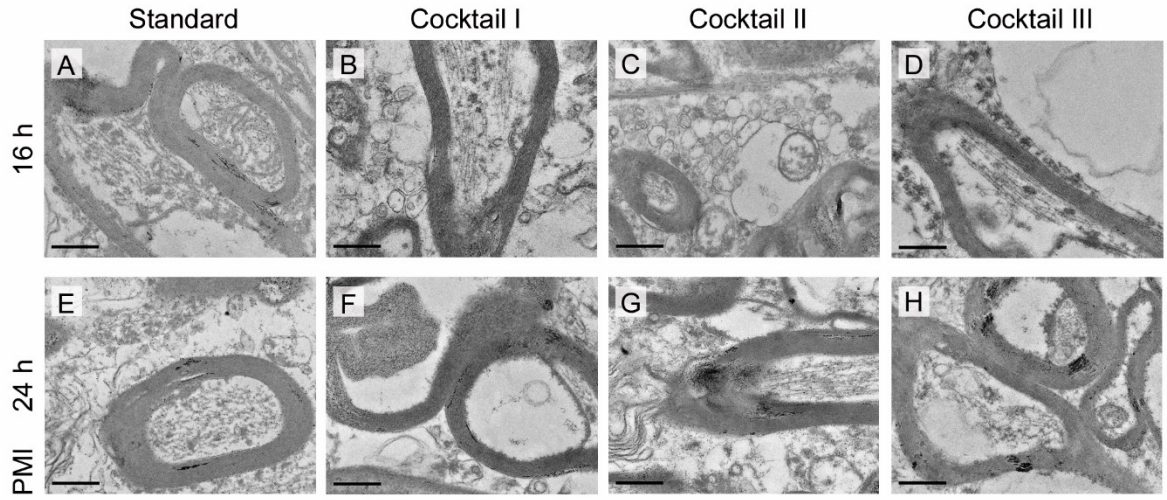

Figure 14: Electron micrographs of human brain samples with different PMIs and cryosubstitution cocktails at 6 500x magnification (146).
(A-D) Frontal lobe from Fe171031 (PMI 16 h), (A) prepared with standard embedding method showing two myelinated axons. (B) After hybrid freezing with freeze substitution one, the myelinated axons have tightly wrapped myelin sheaths with clearly visible microtubules inside the axons and a strong overall contrast. (C) and (D) Samples prepared with substitution cocktail II (C) and cocktail III (D) exhibiting lower contrast and less preserved myelin sheaths than (B). (E-H) Frontal lobe samples from Fe180223 (PMI 24 h), (E) prepared by standard embedding, (F) processed with cryosubstitution cocktail I (hybrid freezing, HFM), (G) hybrid freezing with cocktail II, and (H), hybrid freezing with cocktail III. (F) shows the strongest contrast, but the myelin sheaths exhibit only a slight increase in preservation between (E) and (F) and no clear change in preservation in samples (G) and (H). Scale bars 0.5 µm

The hybrid freezing method (HFM) consisting of chemical fixation (pre- and postfixation), cryofixation (HPF), and cryosubstitution was developed to optimise the preservation of human brain tissue for electron microscopic analysis. This was primarily compared to the standard resin embedding; moreover, also different cryo-substitutions cocktails were tested.

3.3 Ultrastructure of the post-mortem brain

In a double-blinded study with four researchers performing the evaluation and four brains each, the four brain regions (FGM, FWM, Put, GP) and different preparation methods (standard embedding. HFM and different substitution cocktails) were analysed regarding their ultrastructure preservation. The evaluation was done with semi-thin sections (SD) in light microscopic and ultra-thin sections (UD) in electron microscopic images on the basis of a questionnaire (Table 17 and Table 18).

3.3.1 Storage of samples

The stability of the prefixed brain tissue samples was checked by comparison of samples which were initially (at the autopsy date) processed with the standard embedding method

with stored samples of the same tissue. For this procedure, the remaining prefixed tissue was stored at 4 °C in buffer and embedded again to be re-examined. The storage period ranged between around 1.5 months up to over one year.

For the evaluation of the preservation quality of the ultrastructure of the fixed and stored neuronal tissue, the scores of questions UD3, UD4, and UD9-27 were added up and the sums plotted in Figure 15.

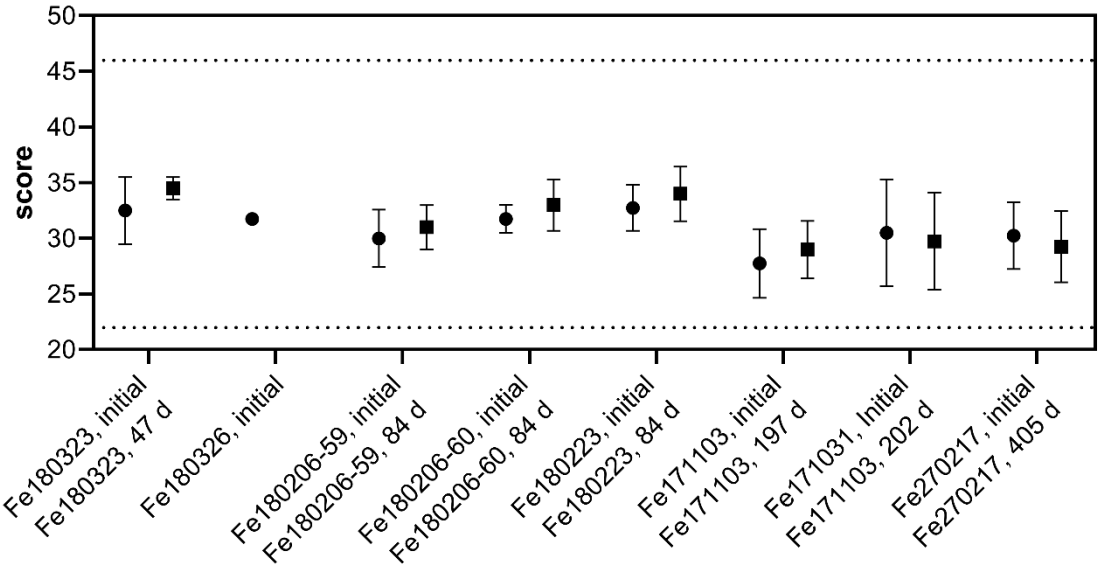

Figure 15: Comparison of the same samples treated with standard embedding initially (dots) and after storage (squares). Lines at the best possible score (46 points) and the worst possible score (22 points). The mean and standard deviation for all evaluators are shown. The value of stored Fe180326 is not available.

No significant differences in the ratings could be determined when the initial score was compared with the score of the stored samples. Therefore, no adverse effects regarding the duration of storage on the ultrastructure could be recognised. Subsequently storage of the prefixed samples in cacodylate puffer at 4°C in the fridge was continued.

3.3.2 Brain under the light microscope

The signs of autolysis are clearly visible even under the light microscope, as can be seen in Figure 16. Most striking are the light dilations around the glia cells and the vessels, which strongly increase with a rising PMI.

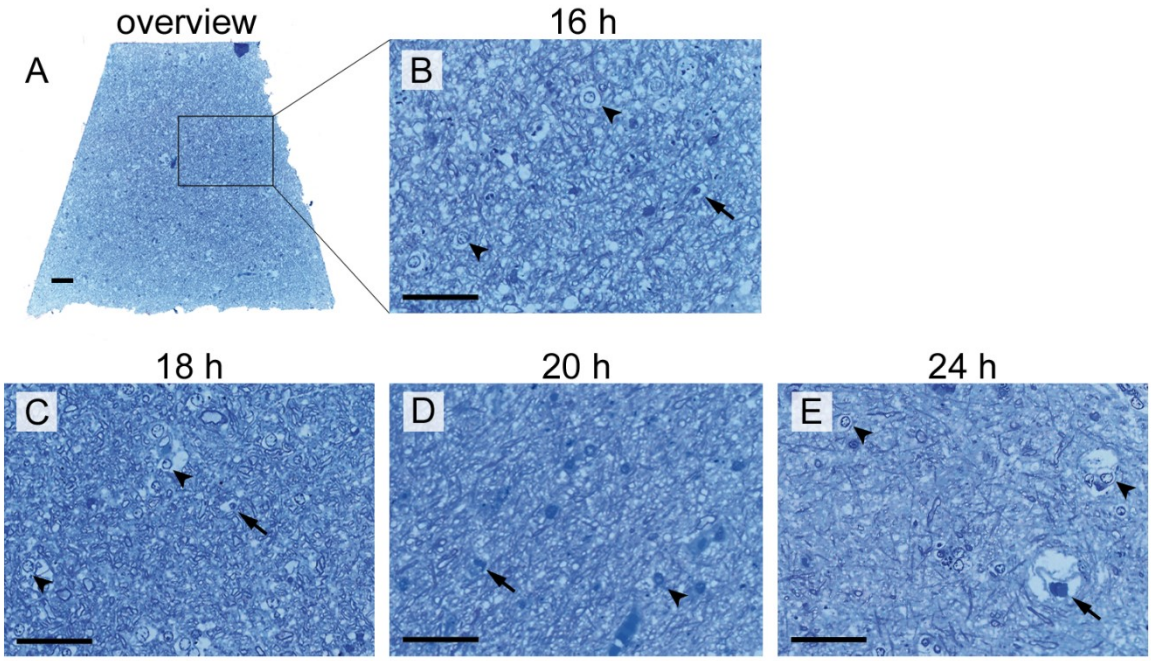

Figure 16: Semi-thin sections of human brain samples under the light microscope (146).
Four samples were prepared with cryosubstitution cocktail I, and after cutting ultra-thin slices 500 nm thick, semi-thin slices were dyed with toluidine blue. The arrows indicate vessels with a light halo and the arrowheads glia cells with halo.
Fe171031, PMI 16 h, frontal grey matter; the zoom-in is indicated with a black square and shown in (B). (C) Fe171103, PMI 18 h, frontal white matter. (D) Fe180206-59, PMI 20 h. frontal white matter. (E) Fe180223, PMI 24 h, frontal white matter. Scale bars 20 µm

In Fe171031, the sample with the shortest PMI (16 h), the neuronal tissue appeared to have a denser organisation. However, the organisation of the tissue appeared to become diffuse and loosen more and more with a rising PMI. Some cellular components degraded beyond recognition and appeared as vacuole-like structures that became more and more apparent with rising PMI (Figure 16 and Figure 18). This is clearly visible in sample Fe180223 with a PMI of 24 h (Figure 16 E or Figure 18 D) where barely any structural details are recognisable in the enclosing matrix and the vacuole-like structures are enlarged and high in numbers.

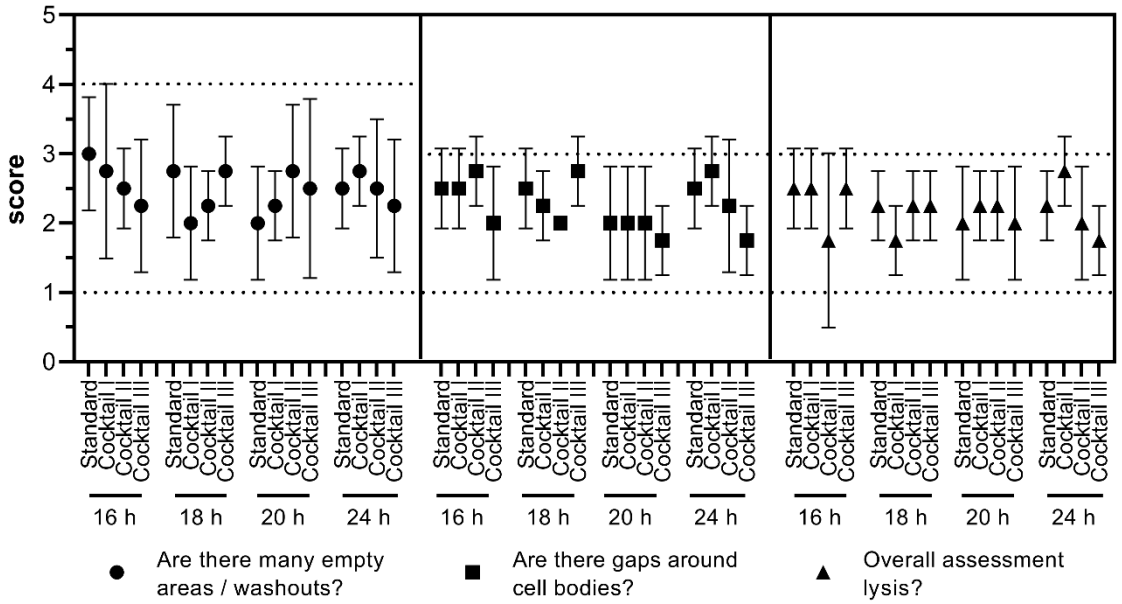

Figure 17: Analysis of the semi-thin sections under the light microscope by all four evaluators.
The dots represent question SD7 with a worst possible score of four, the squares represent question SD8 and the triangles represent question SD9 with a worst possible score of three each. The mean and standard deviation for all evaluators are shown.

Semi-thin sections of the embedded samples of the frontal white matter from the cases Fe171031 (PMI 16 h), Fe171103 (PMI 18 h), Fe180206-59 (PMI 20 h) and Fe180223 (PMI 24 h) were evaluated under the light microscope. The scores of questions SD7-9 regarding autolysis signs are shown in Figure 17. The fluctuation rates of the scoring were very high and therefore no trend in the evaluation of the ultrastructure of the samples prepared with the different substitution cocktails could be observed. This is in stark contrast with the visual observations in the images.

3.3.3 Brain under the electron microscope

The light microscopic impression of the degradation of the ultrastructure including a growing number of vacuole-like structures with an in increasing PMI was even stronger in the EM, as can be seen in Figure 18 D and H.

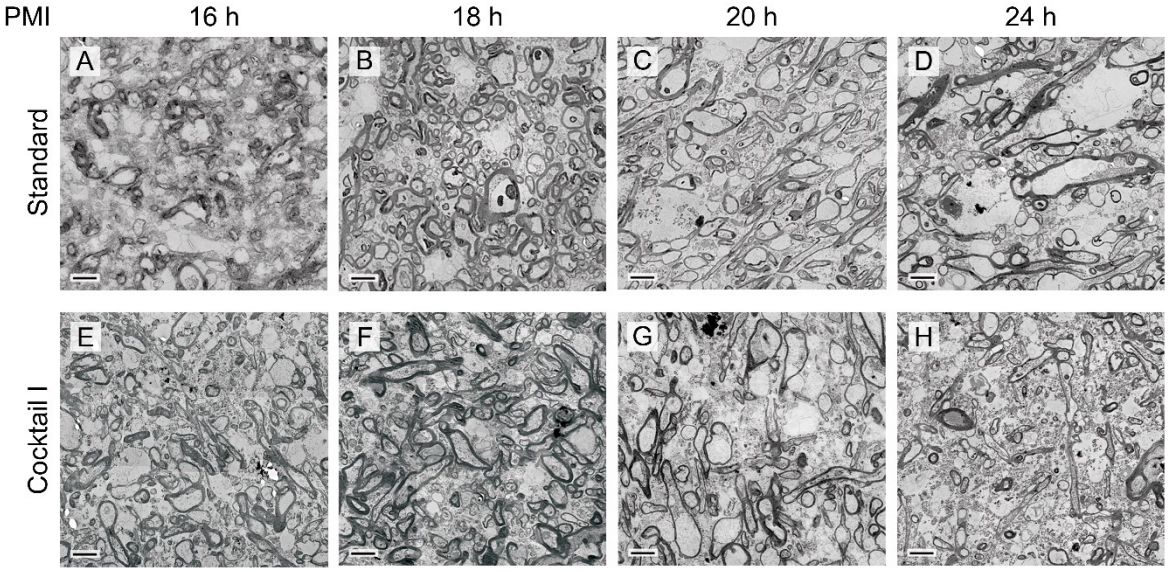

Figure 18: Overview images of brain tissue with different PMIs and prepared either with standard preparation method or with hybrid freezing (146). Nine images with magnification of 1 500x were merged together (3 x 3 montages) for an overview image for all samples (Fe171031 PMI 16 h, Fe171103 PMI 18 h, Fe180206-59, PMI 20 h, Fe180223 PMI 24 h, all frontal withe matter). Top row (A-D): Samples processed with standard embedding and rising PMI, Bottom row: same samples but prepared with the hybrid freezing method (cryo-substitution cocktail I). Scale bars 1 µm

Autolytic processes starting after the death of the patient are responsible for this significant structural degradation. Enlargements of the mitochondria and the coarse ER accompanied by a loss of its ribosomes are further consequences of autolysis. The washed-out look of the cytoplasm and the lack of compartments are due to the chromatin becoming more and more coarse, as shown in Figure 19.

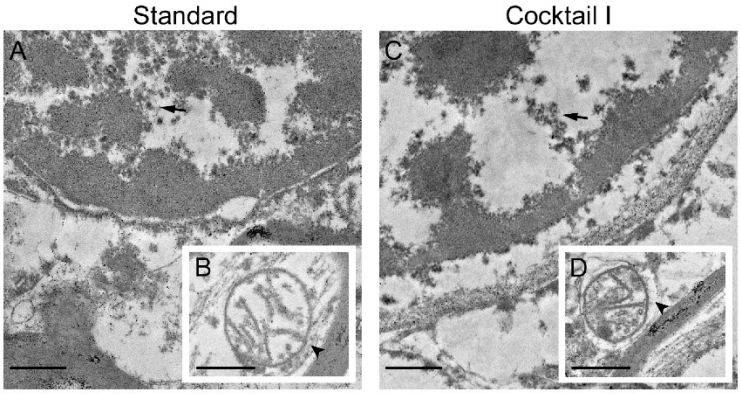

Figure 19: Comparison of EM micrographs from human brain tissue as examples of autolysis either processed with standard embedding or HFM (146). In tissue from Fe180223 with a PMI of 24 h, signs of autolysis can be seen in both preparation methods, for example in (A) and (C), coarse chromatin of the nuclei (arrows) and swollen mitochondria (B and D, arrow heads). Scale bars 0.5 µm

In samples with longer post-mortem time, the cell organelles and compartments were hardly or not at all recognisable and the appearance of vacuole-like or blank membrane bubbles increased. Compared to the samples processed with the standard embedding method, in the ones prepared with the HFM (cocktail I) finer details in the ultrastructure can be seen, which results in a generally denser organisation and enhanced preservation (compare Figure 14 A-D with E-H).

In addition, images of the ultra-thin section from the four cases Fe171031 (PMI 16 h), Fe171103 (PMI 18 h), Fe180206-59 (PMI 20 h), and Fe180223 (PMI 24 h) with the four different methods of processing applied were evaluated in a double-blinded process. For the evaluation, the scores of questions UD3, UD4, and UD9-27 were summed up, as shown in Figure 20.

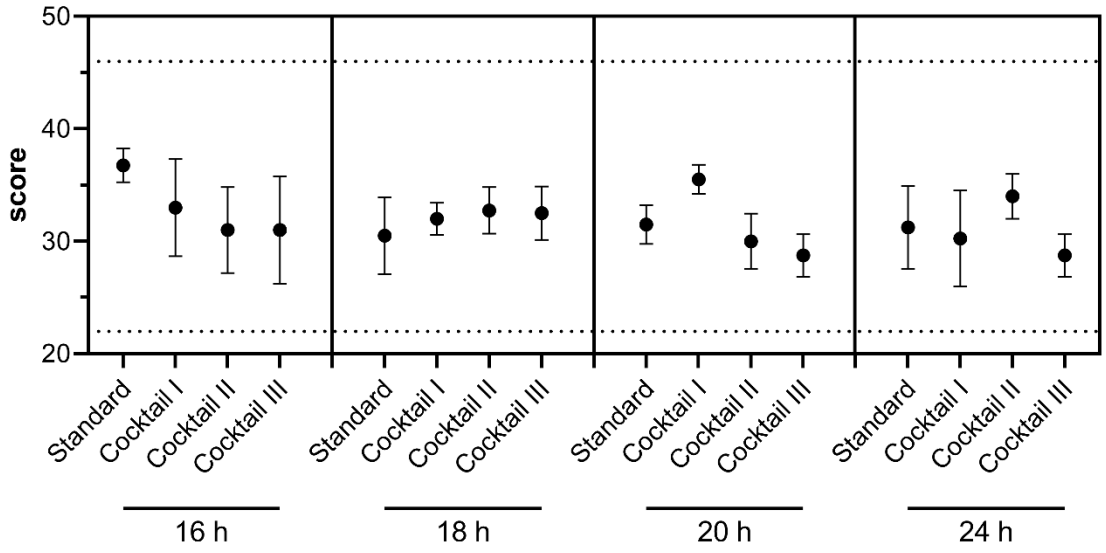

Figure 20: Evaluation of the blinded structural analysis of the samples prepared with the different substitution cocktails.
Lines at the best possible score (46 points) and the worst possible score (22 points). The mean and standard deviation for all evaluators are shown.

In all evaluated specimens except in sample Fe171103 (PMI 18 h), where the standard embedding method had the highest rates, preparation with substitution cocktail III scored best in the blinded evaluation, although the relatively high fluctuation rate in the scores limits the significance of the outcome, which should be approached critically.

3.4 Characterisation of the post-mortem brain

For the assessment of the quality of the preparation but also the tissue samples (general condition, autolysis. etc.), the condition of the myelin sheaths was analysed.

With different approaches, findings from electron microscopy as a visual method were translated to numeric values for comparison. The myelin sheath quality was analysed with a point-counting method. The variation of the thickness of myelin sheaths was measured in g-ratios, and the quality of the brain tissue was assessed through the density of myelinated axons in the tissue.

3.4.1 Myelin sheath quality

For the assessment of the quality of the myelin sheaths, a point-counting method (154) was used. In a first step, a grid pattern with 100 and one with 1024 points were overlaid with the same 18 images (Sample Fe171031-FWM, standard embedding). Thus, the amount of points falling on the myelin sheath were categorized and evaluated, as shown in Figure 21. Due to the big differences in the amount of the well-preserved (5.1 %) and in the unspecified myelin sheaths (3.9 %) determined with both approaches, the analysis with a 1024-point grid was deemed more precise and used for the further analysis.

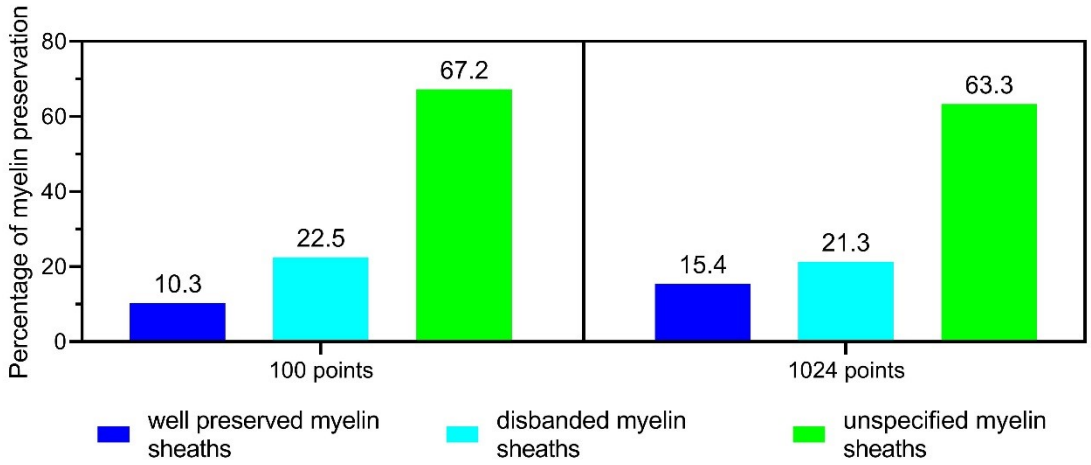

Figure 21: Comparison of the same sample evaluated with a 100- and 1024-point grid pattern to analyse the quality of the preserved myelin sheaths.
The amount of the well-preserved myelin sheaths is represented in blue, the amount of the disbanded in cyan, and the mass of the unspecified myelin sheaths is shown in green.

In a second step, samples produced by hybrid freezing method (HFM) were compared with samples treated with the standard embedding method, focussing on the quality of the myelin sheath preservation. Therefore, the 1024-point-pattern was overlaid with the EM images and the amount of well-preserved, disbanded, and unspecified myelin sheaths was estimated for all four procedures. In total, 68 121 points out of 294 912 were counted and categorized in 288 images.

The apparent influence of the PMI on the quality or on the preservation of the myelin sheaths can be seen in Figure 14. The analysis of the myelin sheaths with the point-counting method points in the same direction. The higher the PMI of the sample, the lower the fraction of well-preserved myelin sheathes. When the HFM (cryosubstitution cocktail I) was applied, the amount of well-preserved myelin sheaths distinctively increased compared to the standard preparation method in all of the cases except in Fe171103, where it remained equal.

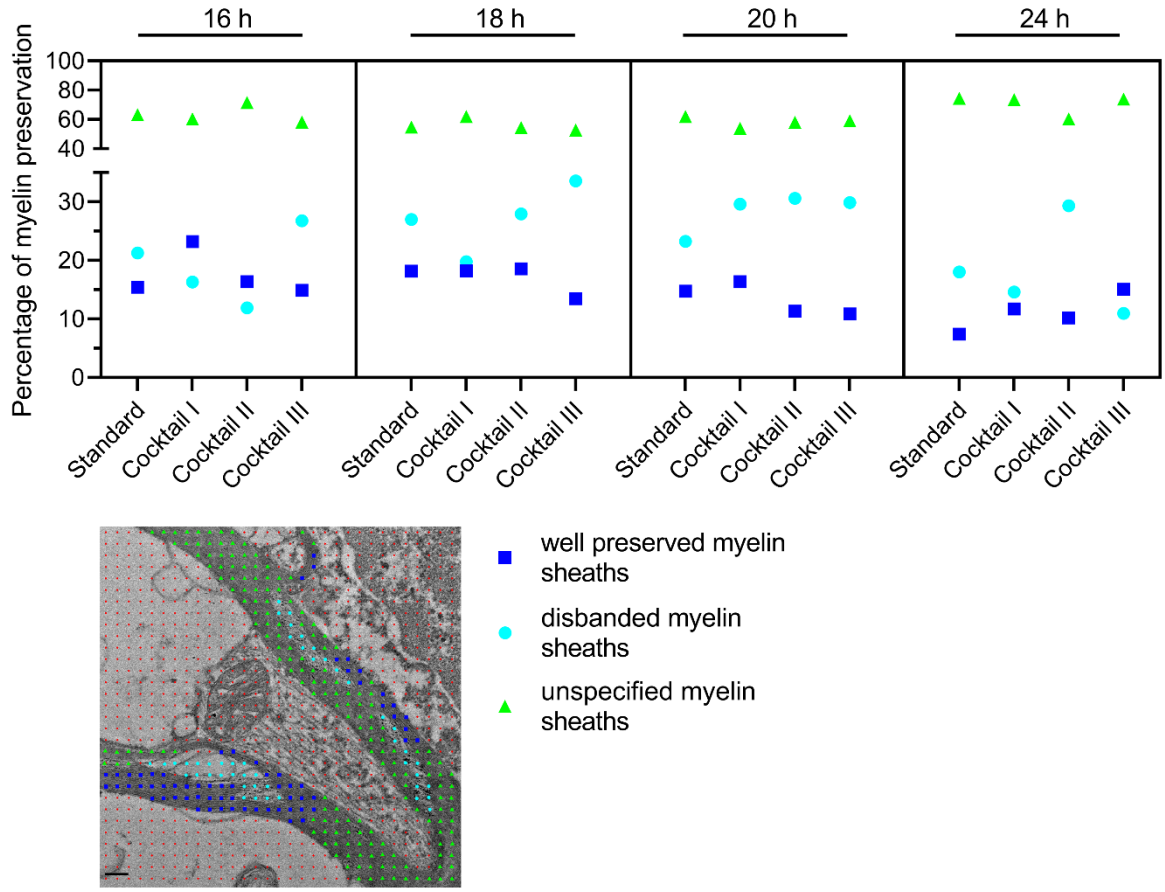

Figure 22: Analysis of the different substitution cocktails regarding the quality of the preserved myelin sheaths and the standard embedding method (146).
Top: The blue squares represent the amount of well-preserved, cyan dots the disbanded, and light green triangles the unspecified myelin sheaths in 18 images per sample; Bottom: An exemplary EM image with the categorized myelin sheaths (colour-marked) and the 1024-point grid pattern in red; scale bar 0.2 µm.

In sample Fe171031, the one with the shortest PMI, a stark increase in well-preserved myelin sheaths by 7.8 % could be observed in contrast to classic embedding. On the other hand, the proportion of disbanded myelin sheaths showed a decline of 4.9 % compared to the HFM when standard embedding had been used for the samples.

The preparation method seemed to have no significant influence on the well-preserved myelin sheaths in sample Fe171103, where only a slight decrease can be seen after

applying cocktail III (Figure 21, second panel). Conversely, the amount of disbanded myelin sheaths decreased by 7.2 % when cocktail I was used instead of the standard method.

The specimens with the longest PMI, Fe180206-59 with 20 h and Fe180223 with 24 h, revealed only a slight increase (1.7 % respectively 4.3 %, Figure 21 right side) in the amount of well-preserved myelin sheaths and generally a lesser incidence when cocktail I was used for preparation.

3.4.2 Density of myelinated axons in brain tissue

Two facts were revealed when the densities of the myelinated axons in the white matter of the frontal lobe were compared. In Figure 23, it can be seen that firstly the axon densities decreased with a longer PMI of the specimen, and secondly, the density of the myelinated axons appeared to be significantly higher than in the hybrid-frozen samples (Figure 23).

For a comparison of the two embedding methods, the HFM and the standard embedding, over 6 000 myelinated axons in an image area of around 6 000 µm² were counted. Significant differences regarding the density of the myelinated axons were revealed by one-way ANOVA, with standard embedding: (F(33.212); p = 0.000) and with cocktail I: (F(22.943); p = 0.000).

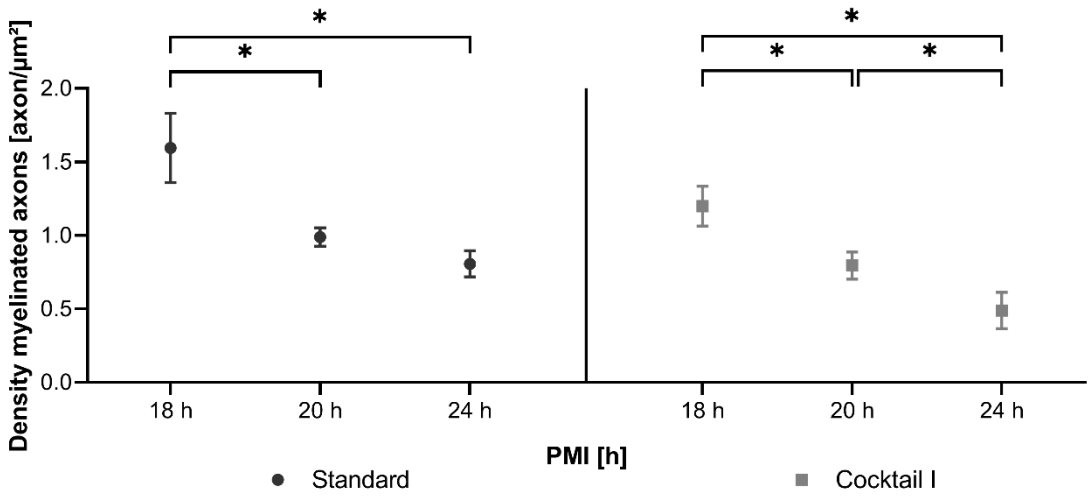

Figure 23: Analysis of the density of myelinated axons in the human frontal lobe with different PMIs prepared with standard embedding and cryosubstitution cocktail I (146).
Mean and standard deviation values of the number of myelinated axons per square micrometre image are shown. One-way ANOVA with Scheffé post-hoc analysis revealed a significant difference *($p < 0.05$) between the standard embedding and cryo-substitution cocktail I.

The samples prepared with standard resin embedding revealed the following axon densities (mean values ± standard deviation). In Fe171103 (PMI 18 h): 1.59 ± 0.22, in Fe180206-59 (PMI 20 h): 0.99 ± 0.06, and in Fe180223 (PMI 24 h): 0.80 ± 0.08. However, when the same samples had been prepared with the HFM method, consisting of cryosubstitution with cocktail I, the following axon densities could be measured: for Fe171103 (PMI 18 h): 1.20 ± 0.12, in Fe180206-59 (PMI 20 h): 0.80 ± 0.08, and 0.49 ± 0.11 for Fe180223 (PMI 24 h).

3.4.3 Evaluation of myelin sheath thickness (g-ratios)

The g-ratio is commonly used both as a structural and a functional index of the optimal axonal myelination. It is defined as the ratio of the inner axonal diameter to the total outer diameter (155) and was measured for each sample. The g-ratios differed significantly between the individuals. In all four sample preparations, a significant difference in the g-ratios of Fe171103 and Fe180206-59 could be seen. Figure 22.

The samples prepared with standard resin embedding showed the following mean values ± standard deviation of the g-ratios: Fe171031 (PMI 16 h) 0.59 ± 0.12, Fe171103 (PMI 18 h) 0.62 ± 0.12, Fe180206-59 (PMI 20 h) 0.70 ± 0.15, and Fe180223 (PMI 24 h) 0.67 ± 0.12. When the same samples were substituted with cocktail I, Fe171031 had g-ratios of 0.61 ± 0.12, Fe171103 0.64 ± 0.10, Fe180206-59 0.70 ± 0.11, and Fe180223 0.65 ± 0.12. When cocktail II was used, the g-ratios were 0.65 ± 0.12 for Fe171031, 0.62 ± 0.12 for Fe171103, 0.73 ± 0.12 for Fe180206-59, and 0.68 ± 0.12 for Fe180223. When cocktail III was applied, the g-ratios were 0.63 ± 0.14 in Fe171031, 0.61 ± 0.13 in Fe171103, 0.69 ± 0.10 in Fe180206-59, and 0.67 ± 0.12 in Fe180223.

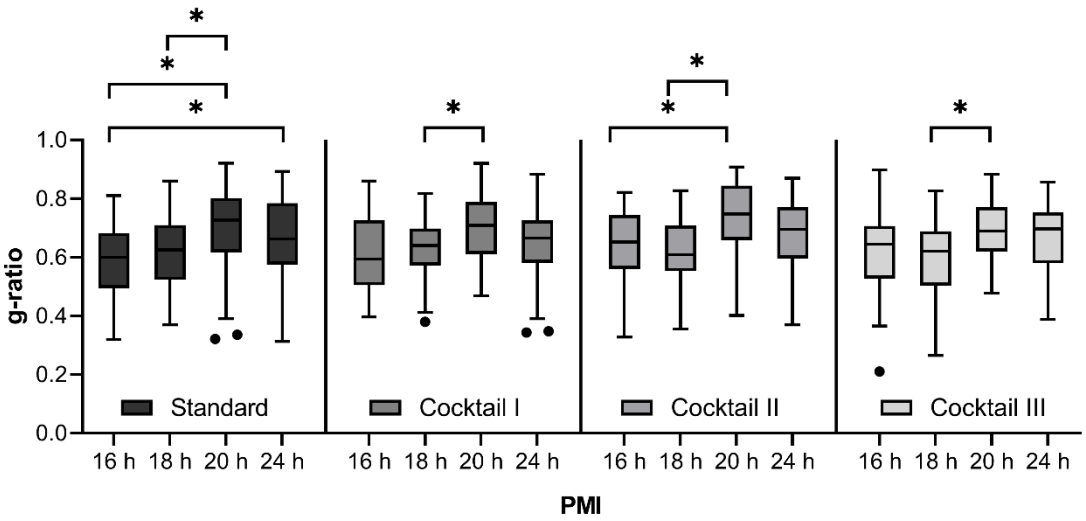

Figure 24: Analysis of g-ratios in the human frontal lobe with different PMIs and variable substitution cocktails compared to standard embedding (146).
Boxplot with Tukey whiskers. ANOVA Scheffé post-hoc analysis revealed a significant difference *($p < 0.05$) between seven samples.

When the samples of the same case had been prepared with different substitution cocktails, no statistically significant differences could be observed. The one-way ANOVA provided the following results: Fe171031: ($F(3.232) = 1.957$; $p = 0.121$); Fe171103: ($F(3.213) = 0.515$. $p = 0.673$); Fe180206-59: ($F(3.231) = 0.448$. $p = 0.719$), and Fe180223: ($F(3.226) = 0.418$. $p = 0.740$).

3.5 Analytical EM

A feasibility test with commercial ferritin isolate from human liver was done with EELS spectroscopy to observe the energy edge of iron in ferritin.

The samples prepared with HPM clearly showed the best ultrastructural preservation of brain tissue. Unfortunately, the samples prepared with HFM were extremely delicate to handle due to their brittleness. Furthermore, they were so sensitive to the electron beam that element analysis with the electron microscope was virtually impossible. For this reason, the samples with standard embedding were used for analytical EM.

3.5.1 Iron measured with EELS

In a feasibility test, purified human liver ferritin (Sigma-Aldrich, USA) was analysed with EELS spectrometry, as shown in Figure 25. The iron in the ferritin showed a strong peak at the iron L_2 edge at 721 eV and with the 3-window method, it was possible to generate an iron map of the image.

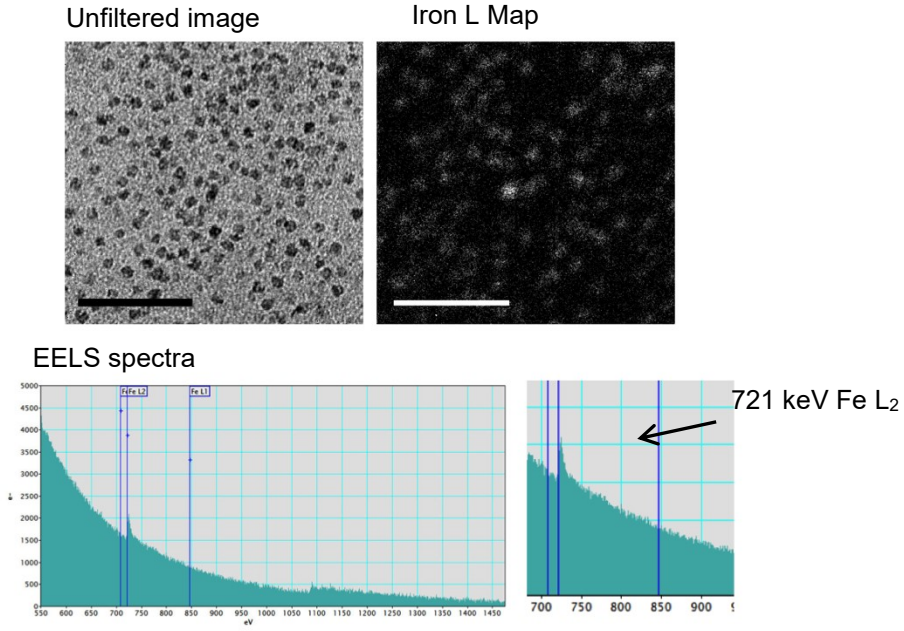

Figure 25: Human liver ferritin (Sigma-Aldrich) analysed with EELS and EFTEM. Data generated in cooperation with Stefan Wernitznig.
Left: In the unfiltered image, the ferritin particles appear differently dark due to their iron content; Right: Iron Map generated with the 3-window method at the L-edge, where iron atoms appear as light dots. Scale bars 50 nm.

3.5.2 Iron measured with EFTEM

With energy-filtered TEM images at the characteristic energy edge of iron, the core of the ferritin particles in the neuronal tissue could be visualised (see Figure 26). For the generation of the iron map, the 3-window technique was used. First a post-edge image was acquired followed by the two pre-edge images, and after spatial drift correction between the images, the elemental map and jump ratio are computed.

The particles with the right size, shape and brightness were interpreted and counted as iron cores of ferritin, indicated with blue circles in the right image in Figure 26.

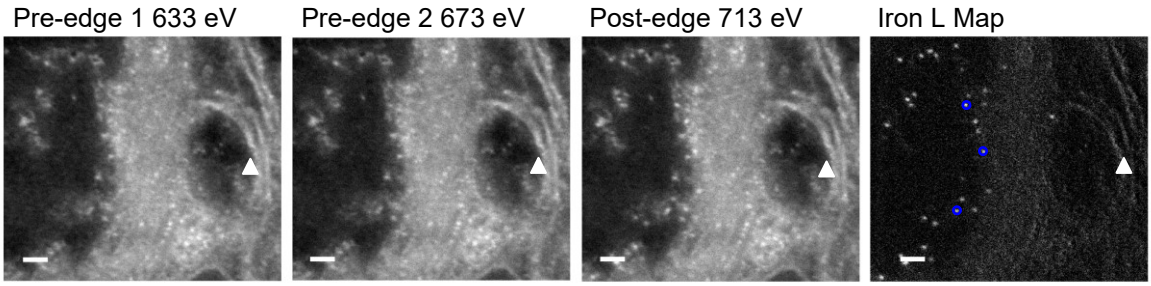

Figure 26: Visualisation of the EFTEM 3 images for iron in human brain tissue. From left to right: Micrographs with magnification of 80 000x at Pre-edge 1, Pre-edge 2, Post-edge and the Iron L Map. The images show an axon with its myelin sheath, which is showing lamellae splitting (white triangles) with iron particles at its edge; three of the 27 iron particles are indicated with blue circles. Scale bars 50 nm

3.5.3 Immunolabelling of ferritin and iron measurement

In a preliminary test, post-embedding immunolabelling with anti-ferritin heavy chain antibodies was carried out in human brain samples. In a first step, samples of the basal ganglia Fe270217 were tested with the standard immunolabelling fixation and embedding. Two anti-ferritin heavy chain antibodies of two different manufactures (Abcam. and Bioss) were used. Both antibodies showed specific labelling of ferritin particles, and the concentration of 1:50 of the primary antibody resulted to be efficient for both antibodies. In a first visual analysis of the labelling rate, the Abcam anti-ferritin antibody appeared to have a higher labelling rate (see Figure 27).

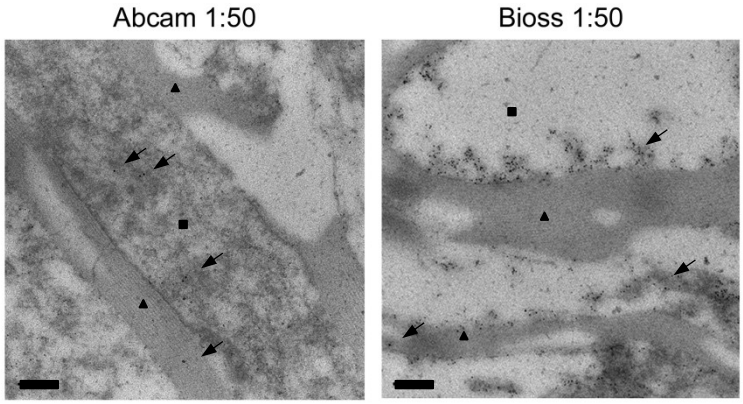

Figure 27: Immunolabelling of globus pallidus treated with anti-ferritin heavy chain primary antibody and 10 nm gold-conjugated secondary antibody, indicated with black arrows, myelin sheaths with triangles, axon cytoplasm with squares. Scale bars 0.2 µm; Left: GP treated with Abcam antibody 1:50; Right: GP treated with Bioss antibody 1:50.

In a second step, the immunolabelling protocol was further developed and systematically tested in the context of the master thesis by Maximilian Schinagl, whom the author of this

thesis supervised (150). With EDX measurements displayed in Figure 28, gold particles (area 1, red box) could be found in close proximity to iron clusters (areas 1 & 2, blue boxes), which indicates that a ferritin particle had been labelled with gold, providing further evidence for the specificity of the antibody.

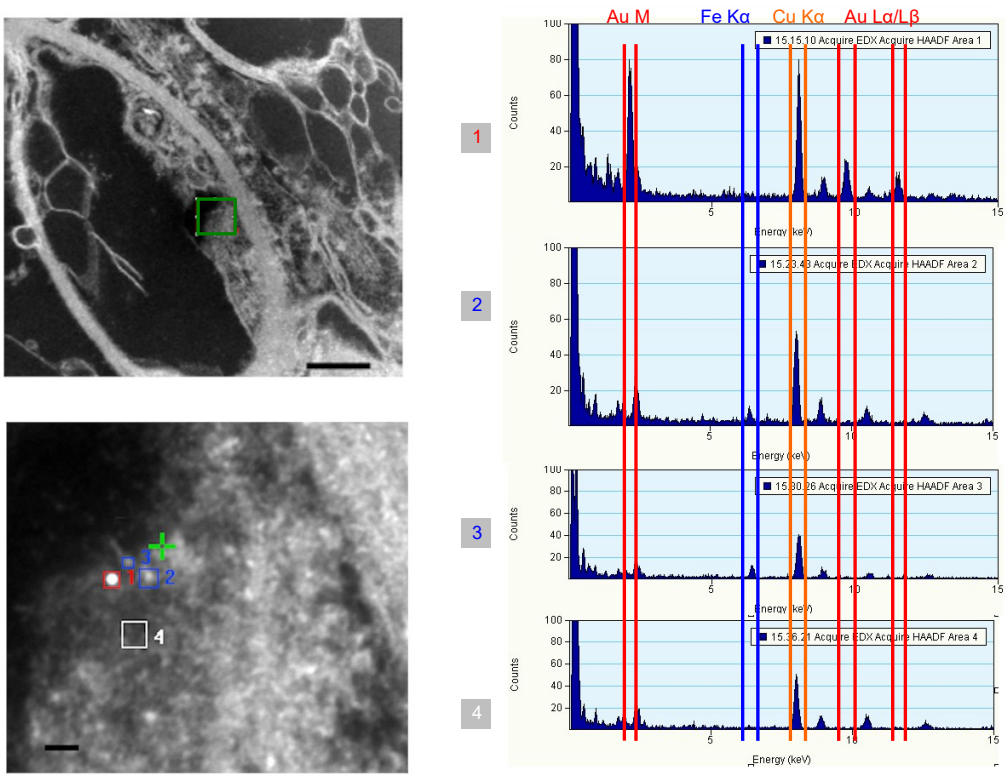

Figure 28: Top: HAADF overview, zoom-in area marked with green square, scale bar 500 nm; Bottom: HAADF image zoom-in with marked spots (1-4) for EDX measurements, scale bar 25 nm; Right: EDX measurements: Area 1 (red box) with strong characteristic peaks at 9.7, 2.1 and 11.4 eV indicating a gold particle; Areas 2 and 3 (blue boxes) are indicating iron particles with a peak at 6 eV, Area 4 (white box) as background area shows strong copper signal at 7.5 eV; data by Maximilian Schinagl (150) and Stefan Wernitznig, reproduced with permission.

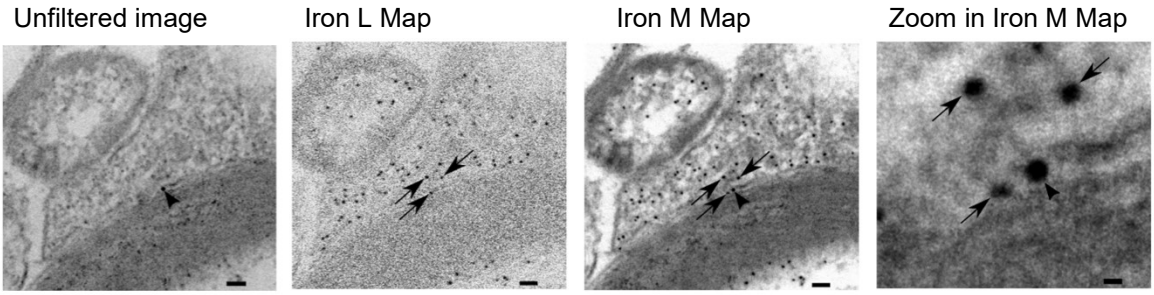

Figure 29: Images unfiltered and filtered at the Iron L and Iron M edge (signal inverted). Iron particles are indicated by black arrows and gold particles by arrowheads. Scale bars 50 nm; zoom-in scale bar 10 nm. Unfiltered Image: In the image, the dark gold dot from the secondary antibody is well visible. Iron L Map: At this energy range, the gold particles are no longer visible. Iron M Map: At this energy range, the iron and gold atoms can be seen. Zoom-in Iron M Map: Gold and iron particles can be seen in close proximity. Data by Maximilian Schinagl (150), reproduced with permission.

The master thesis by Maximilian Schinagl (150) showed that for better contrast, the sample should be treated with 0.1 % osmium during sample preparation (compare Figure 29 with Figure 27). The best labelling rate in the systematic tests was found with the antibody from Bioss in a 1:50 dilution. The Abcam antibody showed a lower labelling rate in the same dilution. In addition, the labelled samples were only lightly stained, with 30 seconds exposure to lead citrate, which made them better suitable for automated gold particle counting.

3.5.4 Iron particles in the brain

Iron particles were counted in 800 micrographs originating from seven brain samples, and in each case, four brain regions were investigated. The detailed list can be found in Table 16. First the number of ferritin cores was determined automatically from iron maps with the Cellprofiler™ program. Then, each map was manually compared to its corresponding jump ratio, resulting in a manual count of the ferritins that were clearly visible in both iron map and jump ratio. The detailed list with the inclusion and exclusion criteria for Cellprofiler™ can be found in Table 19.

The highest total mean concentration of iron particles was observed in the basal ganglia, GP and Put, although a higher mean iron level was found in the putamen. These regions were followed by the frontal cortex and the white matter with the lowest concentration. In general, the calculated concentration of iron particles was lower when manually counted than with the automatic count. Furthermore, the range of the counted iron particles was wider when they were identified and counted by software instead of manually, as is summarised in Table 10. In total, 1730 iron particles were identified and counted in all

measured samples. In Figure 30, concentrations of the iron particles are regionally grouped for each brain. The highest concentration of iron particles was observed in the globus pallidus of Fe270217, followed by the putamen of sample Fe181126. Both samples had an over 520 iron particles per cubic micrometre. By far the lowest concentration of iron particles was found in the frontal white matter of specimen Fe270217.

Table 10: Iron particle concentrations (median values and ranges) counted manually and automatically in Iron Maps and Jump Ratios in each brain region. The evaluated samples are indicated in the column marked with N.

		Automatic Iron particles/µm³			Manual Iron particles/µm³		
	N	Median	Min	Max	Median	Min	Max
FGM	227	40.2	22.5	271.3	29.7	14.3	203.5
FWM	155	32.9	22.7	183.4	12.1	0.0	53.1
Put	200	206.4	57.6	614.0	182.3	39.4	545.1
GP	217	89.0	18.8	620.4	82.7	2.2	529.7

In case Fe270217, the highest concentration of iron particles was found in the basal ganglia, mostly in the GP rather than the Put and in the frontal cortex more than in white matter. In all samples, the concentration of iron particles per cubic micrometre was higher in the frontal grey matter than in the white matter. In case Fe171103, the highest concentrations of iron particles were found in the putamen and the globus pallidus. Only half as many ferritin cores were counted in the putamen of Fe180323 than in the globus pallidus. In the basal ganglia of this specimen, the general iron concentration per cubic micrometre was very low compared to other cases. The second-highest concentrations of iron particles of all samples were found in the putamen of Fe181126, whereas in the GP, only a few particles were found. In the frontal cortex and in the GP, the concentrations of iron particles are nearly equal.

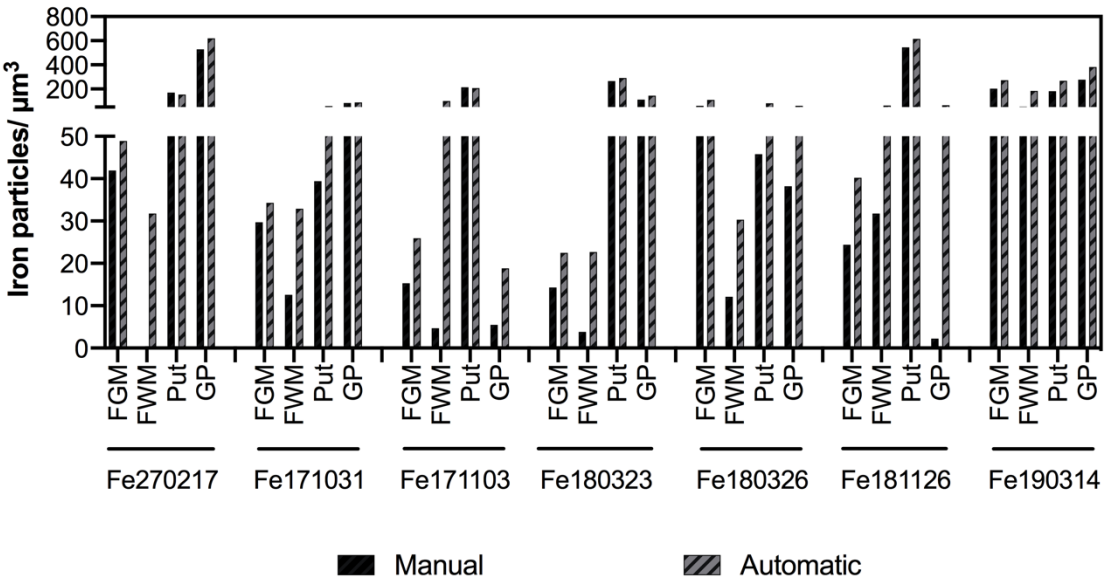

Figure 30: Comparison of the concentration of iron particles per square micrometre in different human brain regions, counted automatically from Iron Maps (grey-black striped bars) and manually counted (black bars).

3.6 Ferritin isolation

In the context of the master thesis by Manuel Hündler, who was supervised by the author of this thesis, an isolation and purification procedure for human brain ferritin was developed (151) and initial size measurements were performed. With bright-field transmission electron microscopy and negative staining (see Figure 31), the purity of the samples was checked. The analysis of the images revealed a mean maximal diameter of 4.8 ± 2.1 nm for the ferritin iron core in the frontal lobe and 5.2 ± 2.2 nm in the occipital lobe.

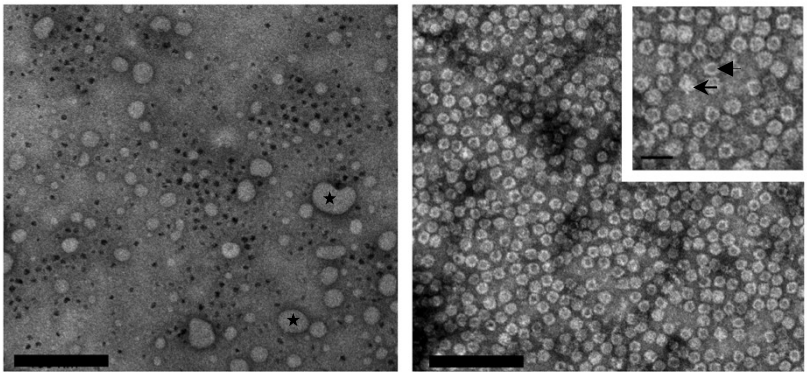

Figure 31: Images of isolated human brain ferritin (frontal lobe, Fe230318) at 50 000x magnification. Scale bar 100 nm. Left: Bright-field image with dark ferritin particles and big light artefacts (stars) from the preparation. Right: Negative staining of the sample, zoom-in: the protein (ferritin, light arrow) appears light and the iron core dark (full arrow), scale bar 25 nm. Data by Manuel Hündler (151) and reproduced with permission.

For the calculation of the mean diameter, over 2 450 particles were measured, showed in Figure 32. The minimal and maximal diameters of the particles were measured to give a better representation of the size and of the orientation and plane of the particles. The various filling stages of the iron in the ferritin particles can be seen in Figure 31 in form of the differently shaped dark cores within the light protein shell in the negative staining image.

For an analysis of stability of the particles, the ferritin isolate of the occipital lobe (Fe180326) was measured initially and after storage at 4 °C for two months. The initial maximal diameter was 5.4 ± 1.6 nm and the minimal diameter of 3.7 ± 1.4 nm, respectively (151).

After the master thesis by Manuel Hündler had been completed (151), the isolated human ferritin was stored and measured again. The ferritin particles showed a maximal diameter

of 4.4 ± 1.8 nm and a minimal diameter 2.9 ± 1.3 nm, respectively. After storage, a decrease of approximately 20 % in diameter size has been observed.

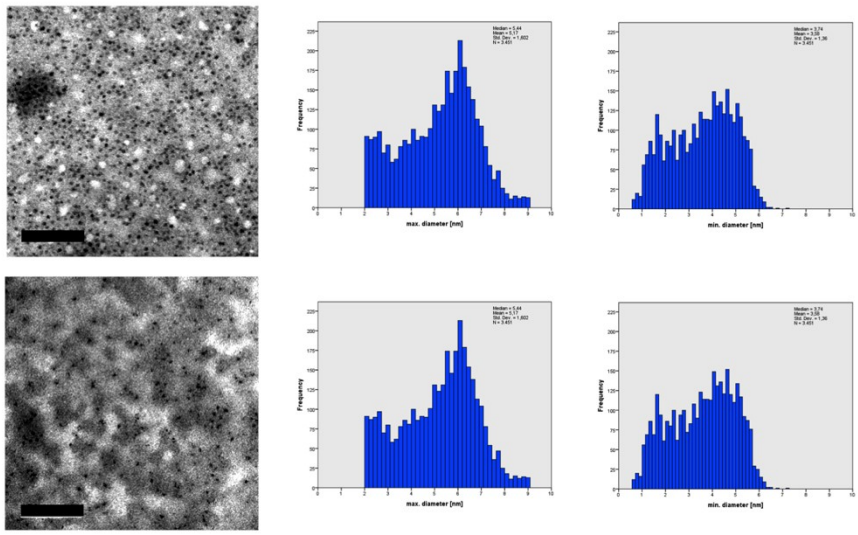

Figure 32: Evaluation of ferritin particles regarding their size, isolated from the frontal lobe (Fe230318); Scale bar 100 nm. Top: Image and distribution of Fe230318 after isolation. Data by Manuel Hündler (151) and reproduced with permission. Bottom: Image and distribution of Fe230318 after two-month storage at 4°C.

For comparison, isolated human liver ferritin (Sigma-Aldrich) was measured and showed a maximal diameter of 5.4 ± 1.6 nm and minimal diameter of 3.7 ± 1.4 nm, respectively. Furthermore, equine spleen ferritin (Sigma-Aldrich) was measured, revealing a maximal diameter of 4.5 ± 1.6 nm and a minimal diameter of 3.1 ± 1.3 nm, respectively.

3.7 Mass spectrometry (MS)

The brain tissue samples were analysed by mass spectrometry at the Institute of Chemistry – Analytical Chemistry for Health and Environment at the University of Graz by Prof. Walter Gössler.

The median concentrations of the five measured elements calcium (Ca), copper (Cu), iron (Fe), magnesium (Mg), and zinc (Zn) were calculated based on wet tissue weight and are summarized in Table 10. In general, in the human brain magnesium had by far the highest concentration with a maximum in the basal ganglia and caudate nucleus and further in the white matter samples. The minimum amount was found in cortical grey matter and the substantia nigra. A similar mean concentration in the brain was found for iron. The mean calcium concentration in all brain regions was in the same range except in the parietal grey matter where the mean concentration was clearly higher. Zinc and copper had the lowest

concentration in the human brain among the measured elements. In the basal ganglia and the caudate nucleus, the maximum amount of zinc could be found, followed by the cortical grey matter, and the minimum was in the white matter samples. The same pattern was shown for the distribution of copper in the brain, except that the maximum amount was in the substantia nigra. The highest mean iron concentration was measured in the basal ganglia and the caudate nucleus, whereas the lowest mean concentration was found in temporal and parietal grey matter, as shown in Table 11.

The concentrations of all measured trace elements, Ca, Cu, Fe, Mg and Zn, of all brain regions are shown in detail in Table 15 in the appendix.

Table 11: Measured brain regions grouped according to their iron amount (mean and SD) in mg/kg wet tissue weight.

	Iron		
	Mean	SD	N
Put	106.63	58.55	9
CN	101.88	57.38	3
GP	88.62	80.62	9
SN	73.49	75.03	3
FWM	41.71	19.13	10
OGM	41.38	14.92	10
OWM	39.18	14.42	10
FGM	37.79	24.61	10
PWM	37.33	2.82	2
TWM	31.69	2.28	2
PGM	25.89	4.33	2
TGM	20.34	0.75	2

3.7.1 Accuracy and reliability of measurement

For ensuring the accuracy and reliability of the ICP-MS measurements of the trace elements Ca, Cu, Fe, Mg and Zn, reference material was measured and the results are shown in Table 12. The measured trace element concentrations of the reference material are in good agreement with the data of the producer.

Table 12: The concentration of 3 measurements of standard bovine muscle tissue specimen (RM 8414, mg/kg dry weight) compared to the certified values.

	Standard specimen values [mg/kg]			Certified values [mg/kg]	
	Mean	SD	Recovery rate [%]	Mean	SD
Ca	155	5	107	145	20
Cu	2.71	0.09	96	2.84	0.45
Fe	68.9	2.1	97	71.2	9.2
Mg	998	47	104	960	95
Zn	146	6	103	142	14

3.7.2 Wet-to-dry mass ratio

In the last column of Table 13, the measured wet-to-dry mass ratios of the different brain regions are shown and graphically displayed and ranked in Figure 33. The grey matter regions and the caudate nucleus showed the lowest values compared to the white matter, where the water content is higher. The lowest wet-to-dry mass ratios were found in frontal and occipital white matter, whereas the highest ratios could be found in temporal and parietal grey matter.

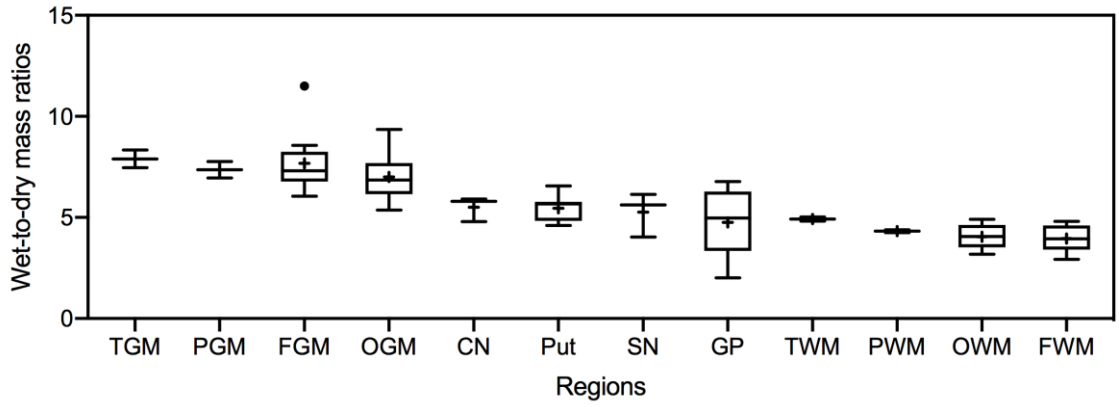

Figure 33: Tissue wet-to-dry mass ratios in different brain regions; box plot with Tukey whiskers and mean indicated with a plus symbol.
TGM, temporal grey matter; PGN, parietal grey matter; FGM, frontal grey matter; OGM, occipital grey matter; CN, caudate nucleus; Put, putamen; SN, substantia nigra; GP, globus pallidus; TWM, temporal white matter; PWM, parietal white matter; OWM, occipital white matter FWM, frontal white matter.

3.7.3 Trace elements in the human brain

The measured trace element concentrations grouped per brain are compared to the published concentration range described in Krebs et al. (43) and displayed in Figure 34 and Figure 35.

In sample Fe270217 with Braak & Braak NFT stage I, the magnesium amount in the frontal and occipital cortex was higher than the range described in Krebs et al. (43), whereas in all other regions the amount was within that range. Only in the frontal cortex and the occipital white matter, the calcium amount was lower than the range described in Krebs et al. (43). The concentrations of copper and zinc of all brain regions were within the range.

In brain Fe171031 in the frontal lobe and in the occipital lobe, the magnesium amount was above the range described in Krebs et al. (43) and in the temporal white matter as well as in the globus pallidus, it was substantially lower. The calcium concentration of the frontal white matter and the putamen was higher than the range described in Krebs et al. (43). In the frontal cortex, the substantia nigra, and (moderately) in the putamen, the copper amount was below the range. In all brain regions except the temporal white matter where it was below the range, the zinc content was within the expected range.

In sample Fe171103, the amount of magnesium in the frontal and occipital cortex was higher than the published range, whereas in the corresponding white matter, the levels were rather low, like in the substantia nigra. Calcium levels were lower except in the occipital cortex and the putamen. In the substantia nigra and the caudate nucleus, the copper concentration was lower than the range described in Krebs et al. (43). The amounts of zinc in the frontal lobe, the occipital cortex, and the putamen were within the range. In all other regions, the levels were too low.

In Fe180223, the sample with the highest Braak & Braak NFT stage of VI, magnesium and zinc levels were higher than the range described in Krebs et al. (43) only in the frontal cortex. The calcium levels were lower only in the occipital lobe. Apart from the globus pallidus, where the concentration was lower than the expected range, copper levels in all other regions were within the range.

In sample Fe180323 with a Braak & Braak NFT stage of IV, the amount of magnesium in the frontal and occipital cortex were higher than the expected range. In all regions, calcium levels were below and the zinc levels within the range. In the basal ganglia and the red nucleus, the copper concentration was below the range.

In sample Fe180326 with a Braak & Braak NFT stage of II, magnesium levels in the frontal cortex were higher and in the occipital white matter lower than the range described in Krebs et al. (43). In the whole frontal lobe, the occipital white matter and the caudate nucleus, calcium concentrations were lower and in the putamen higher than expected. In all brain regions, the measured copper and zinc levels were within the range.

No abnormalities could be observed in the measured trace element values in sample Fe180615 with Braak & Braak NFT stage I.

The magnesium content in sample Fe181126 with an unknown Braak & Braak NFT stage was higher than the published range in the frontal cortex and lower in the occipital white matter. The frontal cortex and the globus pallidus had a lower amount of calcium than the range described. Copper and zinc contents were within the range in all measured brain regions.

The iron amount in the basal ganglia in Fe190215 with an unknown Braak & Braak NFT stage was exceptionally low, whereas the iron amount in the occipital white matter was uncharacteristically high. Calcium levels in the frontal and occipital grey matter were higher than in other samples.

In sample Fe190314 with an unknown Braak & Braak NFT stage, the basal ganglia showed a low iron amount. Especially in the globus pallidus, the iron and calcium levels were extremely low.

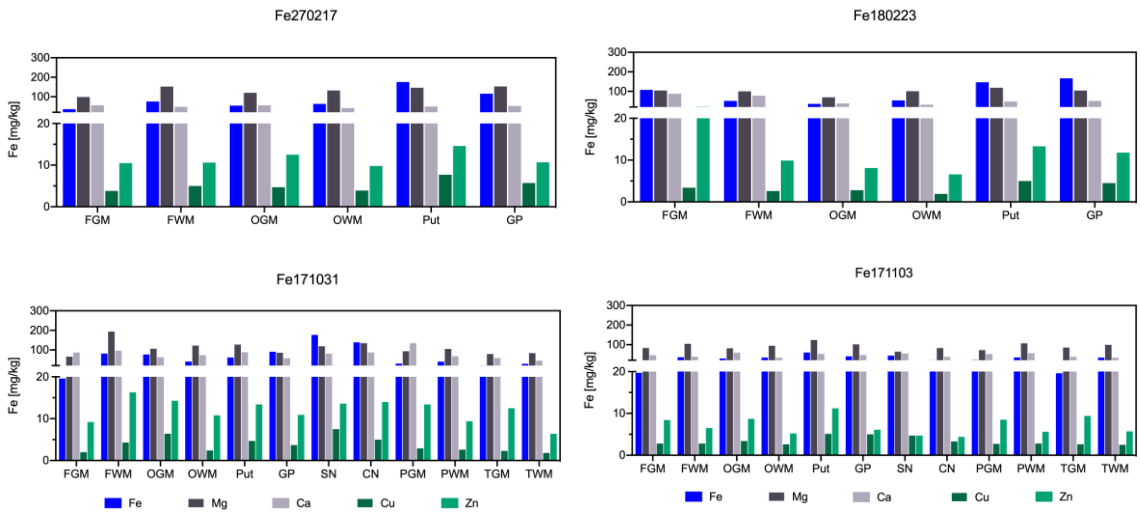

Figure 34: Visualization of the mass spectrometry analyses of all measured brain regions and all trace elements for samples Fe270217, Fe180223, Fe171031 and Fe171103.

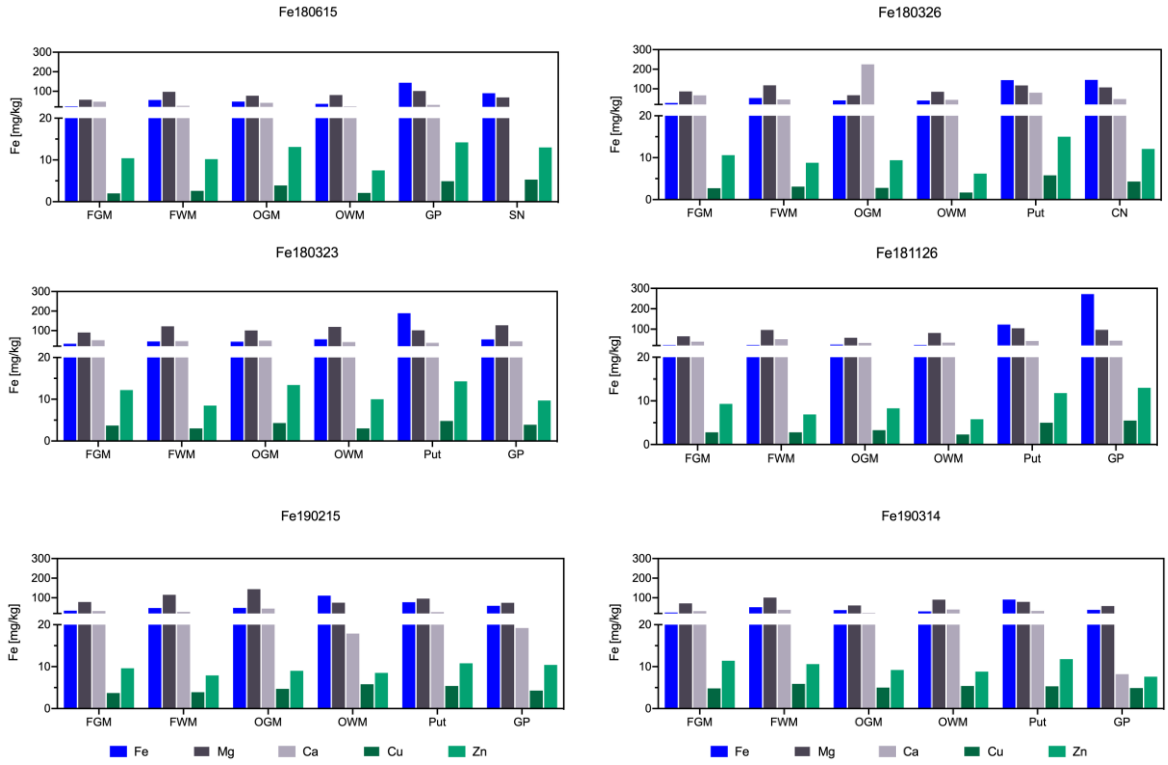

Figure 35: Visualization of the mass spectrometry analyses of all measured brain regions and all trace elements for the samples Fe10323, Fe180326, Fe180615, Fe181126, Fe190215 and Fe190314.

Table 13: Element concentrations (median values and ranges) measured with mass spectrometry for each brain region by wet tissue weight. The wet-to-dry mass ratios of the same brain regions (median and range) are shown in the last column.

	n	Fe [mg/kg]			Mg [mg/kg]			Ca [mg/kg]			Cu [mg/kg]			Zn [mg/kg]			Wet-to-dry mass ratio		
		Median	Range		Median	Range		Median	Range		Median	Range		Median	Range		Median	Range	
			Min	Max		Min	Max		Min	Max		Min	Max		Min	Max		Min	Max
FGM	10	26.6	19.6	107.7	80.6	56.8	104.5	48.9	32.0	87.7	3.12	1.95	4.75	10.5	8.4	21.6	7.31	11.51	6.05
FWM	10	51.8	22.9	81.7	109.9	96.3	193.7	45.8	25.6	96.0	3.05	2.61	5.91	9.4	6.5	16.3	3.94	4.81	2.93
OGM	10	42.0	24.3	76.5	79.3	58.0	144.2	46.9	23.2	225.2	4.07	2.79	6.38	9.3	8.1	14.3	6.85	9.36	5.37
OWM	10	40.7	22.6	110.8	92.5	75.3	132.3	37.4	17.9	73.3	2.50	1.65	5.78	8.0	5.2	10.8	4.06	4.90	3.18
Put	9	122.1	59.6	189.4	110.8	79.4	672.4	45.4	27.4	229.0	5.05	4.69	35.66	13.4	10.8	67.1	5.68	6.56	4.60
GP	9	90.8	38.4	271.6	101.5	58.1	496.5	45.8	0.0	170.8	4.69	3.66	18.70	11.3	6.1	34.8	4.97	6.77	2.02
SN	3	90.3	44.0	176.5	91.4	64.1	118.7	67.6	54.2	81.1	6.09	4.68	7.50	9.1	4.7	13.6	5.62	6.14	4.03
CN	3	139.2	20.8	145.6	107.4	82.8	134.3	47.8	37.5	86.8	4.31	3.29	5.04	12.1	4.4	14.0	5.79	5.92	4.80
PGM	2	25.9	21.6	30.2	82.8	72.2	93.5	93.3	52.2	134.3	2.80	2.69	2.90	10.9	8.5	13.4	7.36	7.76	6.96
PWM	2	37.3	34.5	40.2	106.0	104.9	107.0	62.1	56.2	68.1	2.68	2.58	2.78	7.5	5.6	9.4	4.32	4.39	4.25
TGM	2	20.3	19.6	21.1	82.0	78.9	85.0	48.0	37.7	58.3	2.47	2.34	2.60	11.0	9.4	12.5	7.90	8.33	7.46
TWM	2	31.7	29.4	34.0	91.5	83.7	99.4	39.2	33.2	45.2	2.16	1.77	2.55	6.1	5.7	6.4	4.92	5.03	4.82

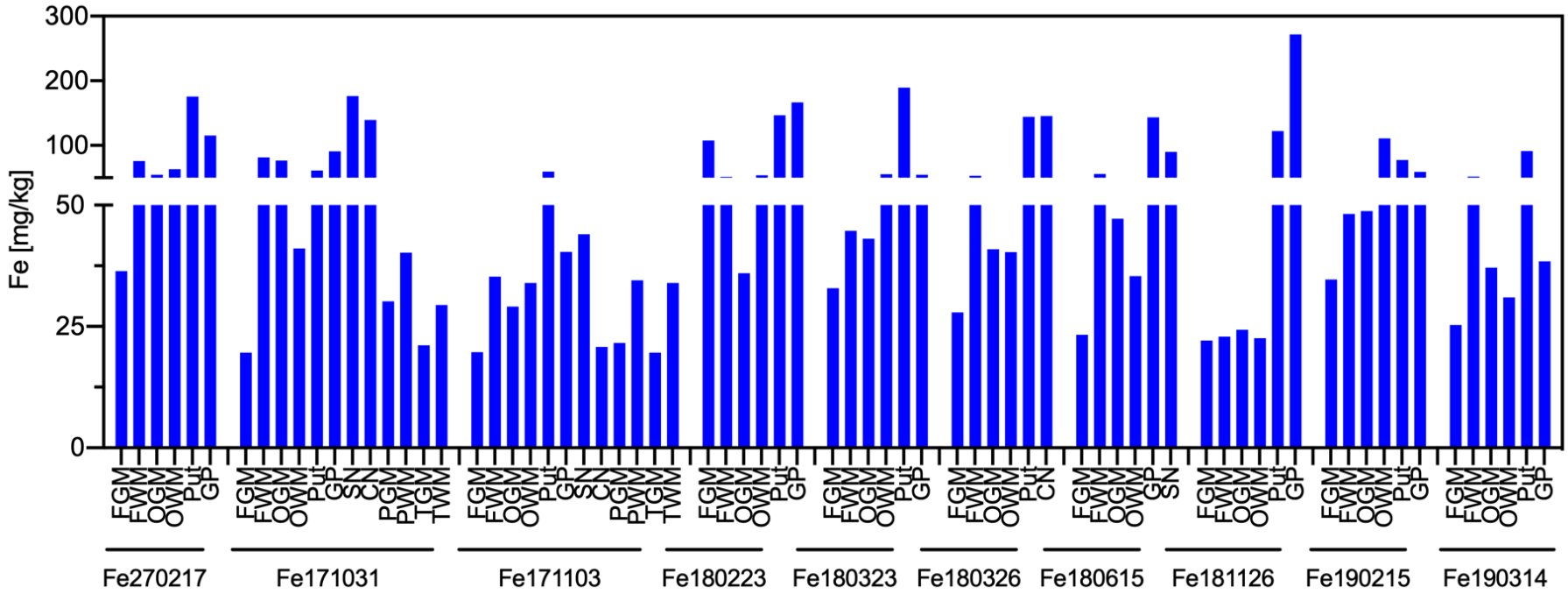

Figure 36: Mass spectroscopy results of all measured samples grouped by samples.

3.7.4 Iron in the human brain

The mean iron concentration of all seven measured brain samples sorted by regions are shown in **Fehler! Verweisquelle konnte nicht gefunden werden.**.

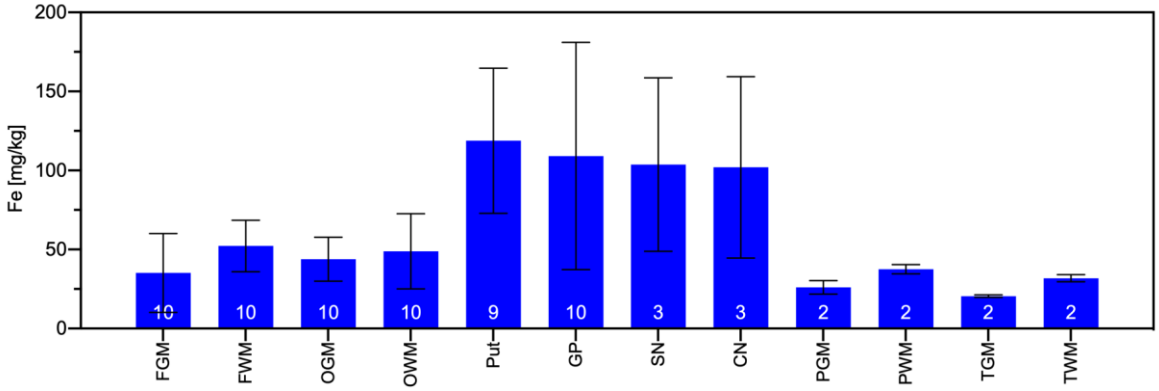

Figure 37: Iron concentration values (mean, SD and sample size) of different brain areas, determined with mass spectrometry

In the globus pallidus of Fe270217, the iron concentration was lower in comparison with the observed ranges in Krebs et al. (43) while it was higher in the frontal cortex and the occipital white matter .Compared with the observed ranges in Krebs et al. (155), sample Fe171031 showed a higher iron level in the occipital cortex and a significantly lower iron level in the basal ganglia. In the substantia nigra and the caudate nucleus in sample Fe171103, the measured iron levels were significantly reduced compared to the literature (155). In the sample with the highest Braak & Braak NFT stage, Fe180223, the iron concentration was higher than the value given in reference only in the frontal cortex (155). Only in the globus pallidus of sample Fe180323, the iron levels were significantly lower than those described in the literature (155). In all measured brain regions of sample Fe180326, the iron concentrations were within the range given in reference (155).

In the iron values of sample Fe180615, no abnormalities could be observed. In sample Fe181126, the iron amounts in the frontal white matter and the thalamus were slightly below and in the globus pallidus slightly above the range given in reference (155).

In the frontal lobe and in the occipital grey matter of sample Fe190215, the iron amount is within the ranges reported in the literature (155). The iron values in the basal ganglia were extremely low, nearly at cortex level. Furthermore, sample Fe190314 had extremely low iron values in the basal ganglia. In all other measured regions, the iron amount was within the range stated in the literature (43).

3.7.5 Comparison of MS and EFTEM results

In Figure 38, the mean concentration of iron particles detected with EFTEM versus the total mean iron amount determined with mass spectrometry for each brain region, the frontal cortex and its corresponding white matter, the putamen and the globus pallidus showed a linear correlation ($R^2 = 0.81$, $p = 0.1027$) when only the mean values are taken into account. Although this correlation can just be observed if the mean values of the brain regions are compared, an intra-regional correlation cannot be seen.

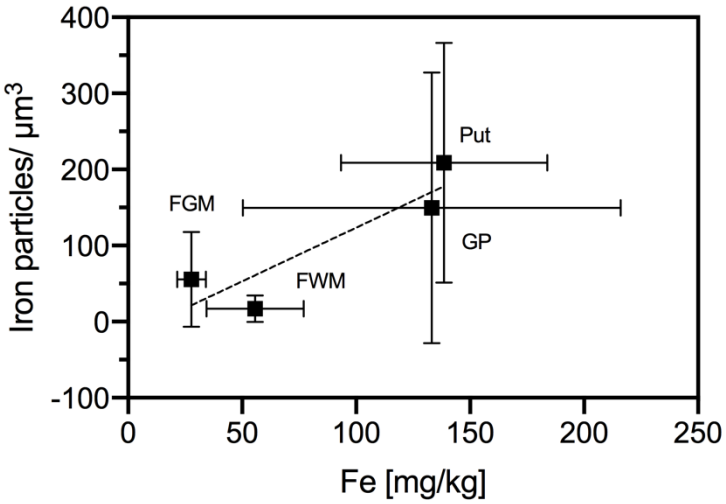

Figure 38: Comparison of the mean concentration of iron particles detected with EFTEM with the total mean iron amount determined with mass spectrometry in seven brains for four brains regions each. The dashed line is the linear regression $R^2 = 0.8051$, $p = 0.1027$. In FWM, the SD was too small to be displayed.

A comparison of the samples with mass spectrometry results and an iron particle count is shown in Table 14.

Table 14: Comparison of the samples with MS and EFTEM results. Samples marked with a question mark refer to Braak & Braak NFT staging being still under investigation.

Case	Brain region	Braak & Braak NFT stage	Fe [mg/kg]	Iron particles/µm^3
Fe270217	FGM	I	36.4	41.9
	FWM	I	75.8	0.0
	Put	I	175.8	168.8
	GP	I	115.5	529.7
Fe171031	FGM	I	19.6	29.7
	FWM	I	81.7	12.6
	Put	I	61.3	39.4
	GP	I	90.8	82.7
Fe171103	FGM	I	19.7	15.3
	FWM	I	35.3	4.7
	Put	I	59.6	213.8
	GP	I	40.4	5.5
Fe180323	FGM	IV	32.9	14.3
	FWM	IV	44.7	3.8
	Put	IV	189.4	265.4
	GP	IV	54.8	112.8
Fe180326	FGM	VI	27.9	60.4
	FWM	VI	53.2	12.1
	Put	VI	144.4	45.8
	GP	VI	-	38.2
Fe181126	FGM	?	22.1	24.4
	FWM	?	22.9	31.8
	Put	?	122.1	545.1
	GP	?	271.6	2.2
Fe190314	FGM	?	25.3	203.5
	FWM	?	52.0	53.1
	Put	?	37.1	182.3
	GP	?	31.0	276.8

4 Discussion

The most important point for any analysis using electron microscopy is the best possible preservation of the ultrastructure, high contrast, and resilience against the electron beam. The best microscope is useless if the subcellular structure to be investigated is not well enough preserved in the preparation to be analysed in detail or even identified. This is especially true if special analyses with the microscope are undertaken like analytical electron microscopy (156) or immunolabelling (116,139).

4.1 Optimisation of sample preparation

Starting point for the optimisation of tissue embedding was the in-house standard embedding protocol. Due to the long PMIs of the samples resulting in a badly damaged ultrastructure of the human brain tissue samples, an improvement of sample preparation would make further analysis less problematic.

4.1.1 Fixation

In the sample preparation for electron microscopy, chemical fixation, mostly consisting of formaldehyde (FA) and glutaraldehyde (GA), is commonly used (157,158). The aldehydes are linking the amino groups of the proteins with methylene bridges (159), thus stabilising the tissue. Caused by this cross-linking, proteolytic enzymes are rendered inactive, although this process is relatively slow (158).

However, an advantage of chemical fixation is the achievable sample size, which is mainly limited by the diffusion rate of the chemicals. Furthermore, the fixation solution can be used independently of the location. Therefore, the time delay from the autopsy to the start of the fixation process can be reduced compared to the cryofixation.

Stabilisation of lipids occurs in a postfixation step with osmium tetroxide, where osmium is added to the conjugated double bonds with simultaneous introduction of heavy metal atoms for enhanced contrast.

What is important for the sample quality when HPF is used is that the sample has to be completely frozen before ice crystals in the cells can be formed (160,161). This is especially challenging in tissue with a high water content, like brain tissue (162) or cell cultures. In order to ensure an efficient temperature and pressure transfer in high-pressure freezing (163), two different filler substances were tested, with hexadecene (164) showing better results compared to a BSA solution.

4.1.2 High-pressure freezing (HPF)

The main advantage of cryofixation, e.g. high-pressure freezing or plunge freezing, with following freeze substitution is the better preservation of the native state of the cell or tissue, as chemical artefacts and their consequences are not introduced. Fixation artefacts can be avoided because the fixation is done physically (frozen) and not chemically (e.g. aldehydes, osmium tetroxide). In addition, with the very low temperatures of the substitution, artefacts like tissue shrinking during dehydration can be reduced. One limiting factor for HPF, particularly when tissue is used, is the limiting space of maximally 200 µm in the carriers, requiring the tissue to be cut to this size. Due to the softness, based on its high water and lipid content and the PMI, this is highly challenging for unfixed brain tissue. The ideal situation for the tissue to be frozen within seconds after the autopsy.
Combining the advantages of standard chemical fixation with those of cryofixation and freeze substitution, a new hybrid freezing method (HFM) was created. As quickly as possible after the autopsy, the brain tissue was first chemically fixed in an aldehyde solution, then cut into 150 µm-thick slices, postfixed with osmium tetroxide, cryofixed with HPF, and afterwards freeze-substituted. By using the HFM, not only a better preservation of the myelin sheaths could be achieved but also a higher contrast in comparison to the standard method consisting of a chemical fixation and dehydration at room temperature. The combination of chemical fixation, cryofixation and freeze substitution is not new (144), but in the HFM, postfixation with osmium tetroxide before HPF and the optimization of the substitution cocktail enhance the preservation of the neuronal tissue.

4.1.3 Freeze substitution with different Substitution cocktails

By applying a substitution cocktail with a combination of osmium tetroxide and uranyl acetate, not only the preservation of the ultrastructure, in particular the myelin sheaths, was improved but also the contrast of the samples was enhanced. This cocktail in connection with postfixation beforehand showed superior results compared to the other cryosubstitution cocktails tested. Despite postfixation of the samples with osmium tetroxide, the osmium tetroxide is again needed in the freeze substitution mixed with uranyl acetate. With the usage of an agitation device (141), the duration of the substitution process could be reduced with the same quality in relation to the protocol of Sosinsky et al. (144) due to the continuous agitation of the samples in the substitution cocktail. In addition, a longer temperature program with a long initial dwell time was tested, although

it did not improve preservation of the ultrastructure and was demanding in its handling (refilling the Dewar bottle with liquid nitrogen during the operation).

Especially when working with human tissue, biosafety is a crucial point, as it is known that certain pathogens like *Mycobacterium tuberculosis* are still viable even after an overnight treatment with 2 % glutaraldehyde (165). Therefore, the application of osmium tetroxide might also lower the infection risk.

One central point for the quality of the sample preparation is dehydration. In this process, cellular components (139) can be extracted and shrinking tissue (136) can introduce artefacts and significant damage to the ultrastructure. The low temperatures of freeze substitution are partially able to preserve the hydration shell of the proteins (139) which makes these dehydration processes far less damaging to the ultrastructure. As it turned out, the cocktail which contained the combination of osmium tetroxide and uranyl acetate was, compared to the other solutions, the one which best preserved the ultrastructure and produced the highest contrast. It is hardly surprising that uranyl acetate enhances contrast, as Weibull et al. (166) state that it stabilises lipids against extraction. It is worth noting that, despite postfixation of the samples with osmium before the HPF, the addition of osmium tetroxide in the substitution cocktail is necessary to achieve good structure preservation. For the preservation of the myelin sheaths, the quantity of osmium applied in the preparation appeared to be important. Often in the freeze substitution of neuronal tissue, the cryosubstitution cocktails contain either tannic acid (135,136,144) or some amount of water (143,163). These additions are supposed to enhance the quality of the preparation regarding structural preservation and contrast, neither of which could be confirmed in the preliminary tests.

4.2 Ultrastructure of the post-mortem brain

For the assessment of the ultrastructural changes in the brain samples, a double-blinded evaluation was carried out. As EM is a visual method, it is difficult to standardise findings without measurements. Furthermore, the area that was analysed by EM was relatively small and it was challenging to compare findings with other non-spatially resolved analytic methods. To exclude the effect of personal bias and individual interpretation (167) as best as possible, four different evaluators with considerable difference in experience, ranging from a few months to decades, were requested to score how well structures in electron microscopic images of the various brain samples had been preserved. Unfortunately, these evaluations generated inconclusive results due to strong fluctuations in the rating of the samples.

4.2.1 Sample storage

The brain tissue was stored at 4 °C after fixation in cacodylate buffer and was embedded on the date of the autopsy and after storage. The duration of storage varied from around 1.5 months to over one year. In the ultrastructural analysis of the tissue samples, no adverse effects regarding the preservation of the ultrastructure could be discovered.

4.2.2 The brain under the microscope

Despite every effort in the optimisation of the sample preparation, like using the hybrid freezing method, the ultrastructural preservation mainly depended on the PMI of the samples (128). This is especially relevant in biopsy samples of the human brain (168). Xu et al. (169) described a rise in vacuole-like structures devoid of any structural material as a sign of increasing autolysis. These structures can be increasingly observed in samples with longer post-mortem intervals.

4.3 Characterisation of the post-mortem brain

The observations from the electron microscopic images as a visual method are converted into a numeric value. The quality of the preservation of the ultrastructure, with special focus on the myelin sheaths, was evaluated regarding the overall myelin-sheath quality with a point-counting method, counting the density of myelinated axons in brain tissue, and an analysis of myelin sheath thickness (g-ratios).

4.3.1 Myelin sheath quality

With the HFM, the quality of myelin sheath preservation could be further increased in samples with short PMIs. With a rising PMI, the effect of the HFM appeared to become smaller. These findings are consistent with the statement by Glausier et al. (128) as they report that the PMI did not change the number of intact myelin sheaths. However, the myelin sheaths displaying lamellae splitting showed a positive correlation with the PMI, although this was not statistically significant.

4.3.2 Density of myelinated axons in brain tissue

It can be further observed that with an increasing PMI, the density of the neuronal tissue clearly decreases. Liu and Schumann (170) could show that the close connection between higher PMI and lower axon densities becomes even stronger. Their samples with a PMI of 36 hours displayed a density of 0.14–0.19 axons/µm² (temporal lobe) (170). Ideally, the PMI of the samples would be zero to avoid the effects of autolysis altogether. Unfortunately, this is not possible due to practical (e.g. logistics, autopsy, etc.) and ethical reasons (farewell of the deceased). Nevertheless, some scientists (171,172) advise against the usage of samples with longer PMIs than seven or eight hours. It seems that all samples prepared with the HFM had a significantly lower axon density compared to their counterparts with standard embedding, which seems to be puzzling at first. During dehydration at room temperature, it is known that tissue can shrink up to 2 % (173), and therefore the density of axons wrongly appeared to be higher. Thus it can be assumed that samples prepared with the hybrid freezing method may be closer to their original or native state than samples prepared with standard embedding.

4.3.3 Evaluation of myelin sheath thickness (g-ratios)

The different preparation methods seemed to have no significant effect on the g-ratios of the brain tissue. Furthermore, it could be observed that the variability between individuals

appeared to be the decisive factor for the g-ratios rather than the preparation method. The question if those significant differences are caused by the diversity of the individuals could not fully be clarified due to the low sample size. As Glausier et al. (128) showed, the g-ratio is significantly associated with the PMI. In addition, no significant differences in the g-ratios were found by Liu and Schumann (170) in their comparison of frozen and formalin-fixed human tissue.

4.4 Hybrid freezing method

In a first step, the focus was placed on the optimisation of the sample preparation process to achieve better ultrastructure preservation in the human brain samples. These matters gained in importance when it began to emerge that the brain samples obtained had very long PMIs. While the goal was to acquire spatially-resolved information on ferritin particles or their iron cores regarding their localisation in the individual cell compartments, this would be nearly impossible without an excellent preservation of these cell compartments or ultrastructure in general. With the newly developed hybrid freezing method, preservation of the myelin sheaths seemed significantly better than with standard embedding. Unfortunately, these samples were very delicate to handle due to their brittleness, as could also be seen under the electron microscope. In preparation for the energy-filtered images, samples were exposed to a reduced electron beam for some time to reduce spatial drift between the images during the long exposure times of the imaging. The samples were very sensitive and could hardly withstand even this energy-reduced electron beam. Despite greatest efforts, it was impossible to use the hybrid-frozen samples for EFTEM imaging. As a consequence, samples with standard embedding had to be used for analytical electron microscopy, as they were able to tolerate the electron beam much better. A significant drawback is that even if the iron cores are found in the EFTEM image, a clear attribution to the relevant cell compartment turned out to be challenging.

4.5 Analytical EM

Energy-filtered TEM relies on electron energy-loss spectroscopy and allows identifying elements due to the change in the kinetic energy of the electrons, which happens when they interact with the sample. It is especially suitable for lighter elements and could also be used to determine the chemical state of atoms. In combination with high resolution electron microscopy, the morphology of ferritin iron cores can be analysed (83,174).

Some metals atoms even show a particularly sharp resonance due to their white lines, e.g. the iron $L_{2,3}$ edge at 707 eV (175) or calcium at the $L_{2,3}$ edge with 348 eV (176,177) at their EELS core edges. With STEM EELS, Aronova et al. (106) could show in the human visual cortex that electron-dense particles along the lines of Gennari contained 1740 ± 580 Fe atoms, which is consistent with the R2* MRI image and a ferritin particle.
EFTEM was used for the localisation of ferritin on a cellular and sub-cellular level through the iron core of the particle. By using a random systematic sampling approach for image acquisition, observation bias was avoided as much as possible. Furthermore, identification and counting of the iron particles were done both manually and automatically.

4.5.1 EFTEM Image Acquisition

Especially due to generally very long exposure times in this study of 30 seconds per image, the images in series (two images before and one at the element-specific energy edge) consequently tend to have a big spatial drift between the individual images that can only partially be corrected. Usually in three-window technique, the two pre-edge EFTEM images are used for background estimation. The calculated background is subtracted from the post-edge image, and the resulting core-loss intensity image or elemental map shows the distribution of the element (178). The intensity of the pixel in the calculated element map is proportional to the amount of the measured element and could result in effective concentration maps (179,180). It should be noted that due to background calculation extrapolation errors and the statistic fluctuations of the elemental map generation, further statistical variations are introduced (178,181). The poor electron yield of the core-losses and the additional noise due to background extrapolation are reasons why EFTEM images are rich in noise by their nature. This problem is aggravated by the drift occurring during the almost unavoidable long EFTEM acquisition times (182). One approach to attempt better drift correction has been described by Heil et al. (183) as they use elastically filtered images instead of the EFTEM images for the calculation of the drift, which would be independent of the SNR. Especially in beam-sensitive materials, it is generally preferred to limit the number of EFTEM images acquired (106). However, when the image numbers are very high, the time effort to calculate the element maps of a series of elastic images is huge. Reduction of the knock-on damage will limit applications like STEM-EELS or EFTEM, and the susceptibility of the specimen to radiation damage might make the lowering of the beam voltage necessary (106). Therefore, sample preparation and image

acquisition should be further optimised as many sample slices showed considerable drift in the electron beam during the EFTEM measurement.

4.5.2 Immunolabelling of ferritin

Preliminary tests regarding the Immunolabelling of ferritin were carried out in preparation for a double immunolabelling, pre-embedding immunolabelling against ferritin in combination with a second, post-embedding immunolabelling against different cell types.
First, two anti-H-chain-ferritin antibodies were tested for immunolabelling in conventionally embedded human brain tissue. The samples showed only moderate contrast and structure preservation, but the labelling with both antibodies was successful. In a first visual assessment of the labelling efficiency, the antibody from the manufacturer Abcam appeared to be better. Optimisation of preparation and labelling was studied in the master thesis by Maximilian Schinagl (150). This included contrast, enhancement with a low amount of osmium tetroxide, made the establishment of automated gold-particle count for immunolabelled samples possible.
Testing a possible double labelling against ferritin and different cell types will be a project for another master thesis. Interesting targets for double labelling would be astrocytes containing glial fibrillary acidic protein (GFAP) associated with intermediate filaments (184) or oligodendrocytes with oligodendrocyte transcription factor Olig2, which is required for oligodendrocyte differentiation (185,186). Neurons or dendrites could be assessed via brain microtubule-associated proteins (MAPs i.e. MAP2) (187–189), and lysosomes could be targeted with lysosome-associated membrane proteins (LAMP) (190) or also by Cathepsin D, which is an acid protease that is active in intracellular protein breakdown (191,192). Furthermore, also a combination with cyropreparation (115,116) could be interesting, as this combination makes a structure preservation and immunolabelling possible.

4.6 Mass spectrometry

With ICP-MS, various brain regions of six brain samples at different Braak & Braak NFT stages were analysed regarding their concentration of calcium, copper, iron, magnesium, and zinc. In addition, the wet-to-dry ratios of the samples were also evaluated, being a key factor for determining the concentration of trace elements, as the samples are dry-frozen, measured, and then calculated with the wet mass recorded for comparison. Therefore, the ratio between wet tissue and dry tissue weight significantly influences the results. The

regions of cerebral cortex in general have a higher water content according to Krebs et al. (43), which could be verified with the data in this study.

4.6.1 Comparability of the MS measurement

Special attention should be paid to the fact that most previous analyses of trace elements were done with formalin-fixed tissue (43,48,193), in contrast to the native and unfixed samples used in this study. In general, tissue in pathology or in tissue banks (48,194,195) is fixed in neutral buffered formalin and thus can be stored for years. The formaldehyde displaces the water in the tissue until a steady state is reached, which can take weeks for a whole brain or hours for a small piece. For example in the study of Krebs et al. (43), the brain tissue spent an average of 58 days in formalin fixation prior to sample preparation for MS. However, various studies report that the fixation of tissue with formalin has an effect on the concentration of trace elements (193,196–198). In these studies, mostly a decrease or leaching of the trace elements in the tissue was described. According to Gellein et al. (197), the leaching is dependent on several factors, like the type respectively the strength of bonding of the trace element in the tissue and the duration of the fixation. Schrag et al. (193) analysed various brain regions and concluded that the effects of fixation differ between brain regions and elements. They described a wide variance in the concentrations and stated that the iron amount in formalin-fixed brain tissue is reduced by 40 % and the zinc concentration even by 75 % (48,193). They assume that this drastic decline is caused by leaching and tissue dehydration. Although Krebs et al. (43) fixed their analysed tissue as whole brains and measured the formalin solution before and after fixation, finding only negligible amounts of iron, they still could not exclude a leaching effect of other elements.

As the samples in this study were native and unfixed when measured, a comparison is difficult as predominantly formalin-fixed brain samples are analysed certainly due to their ready availability. Despite the formalin-fixed samples the trace element concentration measured were predominantly compared to the study of Krebs et al. (43). The congruities regarding the selected brain regions, measured trace elements and methods of analysis were high, and with their great sample size and validation of methods, their results are robust. Furthermore, the samples were tested by the same institute and with the same measurement parameters, which increases the comparability.

As only one case with Braak & Braak NFT stage VI was acquired and measured with MS, no conclusions regarding the regulation of Alzheimer’s disease could be drawn.

4.6.2 Iron in the human brain

As expected, the highest amounts of iron were found in the basal ganglia and the substantia nigra (38,43,199,200), but when the samples were compared by regions, the mean iron content in the regions of cerebral cortex was slightly higher and the content in the basal ganglia is slightly lower than those described in the literature (39,155–15).

Compared with the literature (38,43,199,200), the iron levels were higher in the regions of cerebral cortex and lower in the basal ganglia. A possible explanation may be the very small sample size of this study compared to other research. This is particularly evident in the very high variability of the measured iron concentration. The standard deviation for GP and SN is almost the same as the mean value and for Put, CN, FWM, and FGM it corresponds to half of the mean value. One factor that could also be taken into account, given that the samples in this study are native, is the presence of blood with it heme-iron. However, other authors have stated that the heme-iron in the brain is negligible (43) as the brain iron is mainly attributed to ferritin and hemosiderin (42). Like in other studies (43,47,199,200), tissues from frontal white and grey matter were measured separately. However, the separation of white and grey matter is much easier in fixed than in native tissue. Thus a connection with the other tissue could influence the measurement, as the iron concentration in FWM is higher as in FGM. The fluctuations in the iron concentration can also be explained by the patchy iron distribution in the white matter (60).

The concentrations were moderately higher when compared to Magaki et al. (47) (3.2 times mean, 2.5 times median), which is higher than the findings of other studies, ranging between 1.4–1.7 times (38,43,199).

4.6.3 Trace elements in the human brain

In this study, the highest amounts of magnesium were found in the basal ganglia, nucleus caudate and the cortical white matter samples and the lowest concentration in the cortex samples, which is in good agreement with (43) but the opposite of the findings of Harrison et al. (201). However, for other elements, the data are comparable with this study, thus systemic errors should not be present. The calcium concentrations measured in the brain samples were mostly consistent with the literature (43,202). The highest mean amount of copper was found in the substantia nigra, again in accordance with the literature (43,202,203).

Zinc was predominantly observed in the basal ganglia, whereas in the study of Krebs et al. (43) the highest amount was found in the substantia nigra. However, the sample size was very small and consequently, the results are statistically less robust.

4.6.4 Comparison of MS and EFTEM results

Samples were compared with EFTEM and mass spectrometry data. A linear correlation of these two datasets can only be seen when mean values (without SD) of the brain regions are compared (R^2 = 0.81, p = 0.1027); if the error values are taken into account, the correlation is only moderate (R^2 = 0.25, p = 0.0001). Due to the very small number of samples and the large fluctuation range of the measurement results, no statistically significant correlation can be established between the iron content measured by mass spectrometry and the iron content determined with analytical EM.
Furthermore, was the sample size too small to correlate the iron score with Braak & Braak NFT stages, as other studies had done (204).

4.7 Ferritin isolation

It is known that ferritin diameters vary strongly also between the different brain regions, like in the GP 3.5 ± 0.1 nm, SN 3.7 ± 0.1 nm, HIP 3.1 ± 0.2 nm (50). Furthermore, ferritin iron core diameters of 4.8 ± 2.1 nm could be observed in the frontal lobe and 5.2 ± 2.2 nm in the occipital lobe (151). The ferritin diameters measured in this study are clearly bigger than those described in literature. One factor may be that the lighter fractions of the ferritin particles, which are filled with less iron and thus smaller in size, were discarded in favour of a higher purity of the isolated ferritin fraction in the last preparation step.
Jian et al. (83) measured with high-resolution electron microscopy (with HAADF) in equine spleen a ferritin diameter of 7.5 nm at 12 million times magnification. This is around 40 % bigger compared to the 4.5 ± 1.6 nm measured at 50 000 times magnification. In isolated human liver ferritin a maximal diameter of 5.4 ± 1.6 nm could be measured, whereas Galazka-Friedman et al. (50) measured a ferritin diameter of 6.05 ± 0.5 nm, which is 12 % bigger in size.

4.8 MRI

It could be shown that ferritin and hemosiderin are affecting the MR signal from brain tissue due their paramagnetic properties (205). As it is challenging to distinguish heme from non-heme iron sources with MRI (206,207) special iron-sensitive sequences like a

spoiled multi-echo 3D FLASH sequence, Gradient echo T_{2*}, or susceptibility-weighted imaging were developed to observe the iron level in the brain of patients with AD (48). In the last years, several studies could show that with MRI, the iron levels in the brain are a useful biomarker for AD. They revealed that only in the putamen the iron amounts are increased (208–210) due to AD, which is consistent with studies using other technologies like mass spectrometry (43,48). Unfortunately, the increase of iron in the putamen is not specific for Alzheimer's disease and therefore not very helpful in diagnosing this disease (48). Also in multiple system atrophy (MSA) high amounts of iron in the posterolateral putamen and SN could be observed (211–213). It was also shown in MSA that the increased iron accumulations are associated with an increased ferritin level (203,214). However, it is difficult to compare data because iron is usually detected in tissue using very different methods (215).

The MR images of the brain are difficult to compare with EM findings due to the different size of the analysed volume. The MRI provides insight into the iron distribution of the whole hemisphere while the EM can only provide information on the iron distribution in the range of a few cubic nano- or micrometres. But the observed distribution of ferritin or the iron is important for the development of iron sequences in the MR, as the magnetic shielding of a ferritin particle localised in the axon tubuli is different from that of ferritin in the myelin sheath.

Due to their paramagnetic properties, engineered ferritin nanocages are tested as natural contrast agents in magnetic resonance imaging (216,217).

4.9 Challenges in methodology and approach

In general, EM investigations are extremely time-consuming due to their long sample preparation which, depending on the method, takes between 1.5 and 2.5 weeks until the sample reaches the microscope. Even with the aid of a script for unbiased random systematic sampling (149), which navigates the microscope to the recording positions, the recording protocol for one sample took in total 13 hours (of which 5 hours were for sample exposure to the beam usually done overnight; thus, an overnight period plus 7 hours were measurement time, 1 hour for acquiring overview images). Therefore, it will be necessary to develop better or more automated protocols so that more samples could be analysed in a timely manner.

Furthermore, the analysis of the iron particle should be improved in the future as automatic counting produces too many false-positive results and manual evaluation is extremely

time-consuming. In addition, an important consideration is the personal fluctuation in the evaluation of images. As the double-blind scoring in this study showed, even with a questionnaire and meetings of the evaluators for the classification of structures, the fluctuation in their ratings were huge. Therefore, an improvement of automatic evaluation would be recommended for the future.

Taking into account all circumstances and the sample size, any differences of the regulation or distribution in AD could not be observed, as the sample size of tissue from diseased patients was substantially too small to draw any conclusions.

4.10 Comparison of healthy and diseased brains

Heiko and Eva Braak (36,145,218) developed a staging of Alzheimer's disease-related neurofibrillary changes in human brain tissue with immunocytocehmical methods. Alzheimer's disease is characterised through intra-neuronal lesions which consist of neurofibrillary tangles (NFTs) and neuritic plaques (NPs) (145). Braak and Braak categorized the disease propagation of Alzheimer's disease in six stages. The stages are distinguished with respect to the location and severity of the neurofibrillary changes of the neurons. The transentorhinal stages I-II are medically silent cases without symptoms. In the limbic stages III-IV, an incipient stage of Alzheimer's disease can be seen, and in the neocortical stages V-VI Alzheimer's disease is fully developed (218).

From the nine samples with Braak & Braak NFT staging, five samples were in stages I-II, one in stage IV and three samples in stages V-VI. But electron microscopic analyses were so far only done in three samples with stage I, one with stage II, und one with stage IV (and two without a staging). Therefore, due to low sample size and high personal variability in the human brain, any conclusions regarding the distribution and regulation changes of ferritin or iron in the brain of Alzheimer patients cannot be drawn.

It is known that in the AD cortex, iron was found in Aβ-plaques, microglia (219), and in cortical layer III-V with very pronounced tau pathology (204). The meta-analysis by Tao et al. (220) and other studies (221) share the opinion that the iron level is increased in the cortex of AD patients, which could not observed in this study.

4.11 Conclusion

The aim of this thesis was to analyse different regions of the human post-mortem brain with low and high iron amounts regarding the number of ferritin cores per volume.

For a visual analysis of the distribution of ferritin in the human brain, only the resolution of the electron microscope is sufficient. In combination with energy filters beneath the microscope, the iron core of the ferritin particles can be mostly visualized.

With mass spectrometry, the total amount of five trace elements (Ca, Cu, Fe, Mg, and Zn) was determined. As the samples in the MS analysis in this study were native and most of the published data are from formalin-fixed tissue, the comparison was challenging. The mean iron concentrations of all seven samples were higher in the cortex and lower in the basal ganglia than described before (43). The other measured trace elements were within the normal range although the results are moderately meaningful due to the very small sample size and the high variability of the measurements. A magnetic resonance (MRI) iron scan of one hemisphere of each human brain sample was also performed in order to compare the scan data with the other measurements in order to improve the iron sequences in the future.

With the establishment of a new hybrid freezing method for human brain samples for electron microscope (146), even in samples with long post-mortem intervals the myelin sheaths could be better preserved than with classical embedding. Compared to the standard embedding method, the tissue samples prepared with the HFM had better contrast, apparently less shrinking, and better preservation of the cellular and sub-cellular details of the myelin sheaths. Unfortunately, these samples were also more brittle and sensitive in handling. Especially when exposed to the electron beam for a long time for analytical EM, they were too delicate to withstand, so the samples with standard embedding had to be used for analytical EM.

For size determination, the ferritin particles were isolated from human brain tissue and analysed under the electron microscope. The determined sizes of the ferritin particles were around 10 % higher compared to the literature (151).

On average, in the frontal cortex an iron particle concentration of 55.6 and in its corresponding white matter 16.9 iron particles per cubic micrometre could be observed with analytic EM. In the basal ganglia, a higher amount of 208.7 in the putamen and 149.7 iron particles per cubic micrometre in the globus pallidus, respectively, were found. A correlation of the iron concentration determined by EFTEM and mass spectrometry

could only be observed if the mean values of each brain region are compared, which is, however, not statistically significant.

It turned out to be very challenging to acquire sufficient human brain samples, therefore the sample size in this study was very limited, which also significantly limited its informative value. Consequently, no differences in the iron regulation in samples with Alzheimer's disease could be observed.

References

1. Samii A, Ransom BR, Nutt JG. Early onset Parkinson's disease [1]. Rev Neurol. 2004;
2. Yesavage JA, O'Hara R, Kraemer H, Noda A, Taylor JL, Ferris S, et al. Modeling the prevalence and incidence of Alzheimer's disease and mild cognitive impairment. J Psychiatr Res. 2002;
3. Venda LL, Cragg SJ, Buchman VL, Wade-Martins R. α-Synuclein and dopamine at the crossroads of Parkinson's disease. Trends Neurosci. 2010;33(12):559–68.
4. Bird TD. Genetic aspects of Alzheimer disease. [Review] [113 refs]. Genet Med. 2008;10(4):231–9.
5. Ray Dorsey E, Elbaz A, Nichols E, Abd-Allah F, Abdelalim A, Adsuar JC, et al. Global, regional, and national burden of Parkinson's disease, 1990–2016: a systematic analysis for the Global Burden of Disease Study 2016. Lancet Neurol. 2018;17(11):939–53.
6. Nichols E, Szoeke CEI, Vollset SE, Abbasi N, Abd-Allah F, Abdela J, et al. Global, regional, and national burden of Alzheimer's disease and other dementias, 1990–2016: a systematic analysis for the Global Burden of Disease Study 2016. Lancet Neurol. 2019;18(1):88–106.
7. Zecca L, Youdim MBH, Riederer P, Connor JR, Crichton RR. Iron, brain ageing and neurodegenerative disorders. Nat Rev Neurosci. 2004 Nov;5(11):863–73.
8. Ward RJ, Zucca FA, Duyn JH, Crichton RR, Zecca L. The role of iron in brain ageing and neurodegenerative disorders. Lancet Neurol. 2014 Oct 1;13(10):1045–60.
9. Belaidi AA, Bush AI. Iron neurochemistry in Alzheimer's disease and Parkinson's disease: targets for therapeutics. Journal of Neurochemistry. Blackwell Publishing Ltd; 2016. p. 179–97.
10. Wang P, Wang ZY. Metal ions influx is a double edged sword for the pathogenesis of Alzheimer's disease. Ageing Res Rev. 2017;35:265–90.
11. Khalil M, Teunissen C, Langkammer C. Iron and Neurodegeneration in Multiple Sclerosis. Mult Scler Int. 2011;2011:1–6.
12. Ndayisaba A, Kaindlstorfer C, Wenning GK. Iron in neurodegeneration - Cause or consequence? Front Neurosci. 2019;13(March):1–15.
13. Beal MF. Mitochondria take center stage in aging and neurodegeneration. Ann

Neurol. 2005;58(4):495–505.

14. Palmer CS, Osellame LD, Stojanovski D, Ryan MT. The regulation of mitochondrial morphology: Intricate mechanisms and dynamic machinery. Cell Signal. 2011;23(10):1534–45.
15. Zeineh MM, Chen Y, Kitzler HH, Hammond R, Vogel H, Rutt BK. Activated iron-containing microglia in the human hippocampus identified by magnetic resonance imaging in Alzheimer disease. Neurobiol Aging. 2015 Sep;36(9):2483–500.
16. Iba M, Guo JL, McBride JD, Zhang B, Trojanowski JQ, Lee VMY. Synthetic tau fibrils mediate transmission of neurofibrillary tangles in a transgenic mouse model of alzheimer's-like tauopathy. J Neurosci. 2013;33(3):1024–37.
17. Stöhr J, Watts JC, Mensinger ZL, Oehler A, Grillo SK, DeArmond SJ, et al. Purified and synthetic Alzheimer's amyloid beta (Aβ) prions. Proc Natl Acad Sci U S A. 2012;109(27):11025–30.
18. Collinge J, Clarke AR. A General Model of Prion Strains and Their Pathogenicity. Science (80-). 2007 Nov 9;318(5852):930–6.
19. Prusiner SB. Nobel Lecture: Prions. Proc Natl Acad Sci. 1998 Nov 10;95(23):13363–83.
20. Kaufman SK, Thomas TL, Del Tredici K, Braak H, Diamond MI. Characterization of tau prion seeding activity and strains from formaldehyde-fixed tissue. Acta Neuropathol Commun. 2017;5(1):41.
21. Zigmond M, Rowland L, Coyle J. Neurobiology of brain disorders: biological basis of neurological and psychiatric disorders. 1st Editio. Academic Press; 2015.
22. Giacci MK, Bartlett CA, Huynh M, Kilburn MR, Dunlop SA, Fitzgerald M. Three dimensional electron microscopy reveals changing axonal and myelin morphology along normal and partially injured optic nerves. Sci Rep. 2018;8(1):1–12.
23. Nasrabady SE, Rizvi B, Goldman JE, Brickman AM. White matter changes in Alzheimer's disease: a focus on myelin and oligodendrocytes. Acta Neuropathol Commun. 2018;6(1):22.
24. Yang WS, Stockwell BR. Ferroptosis: Death by Lipid Peroxidation. Trends in Cell Biology. 2016.
25. Morris G, Berk M, Carvalho AF, Maes M, Walker AJ, Puri BK. Why should neuroscientists worry about iron? The emerging role of ferroptosis in the pathophysiology of neuroprogressive diseases. Behav Brain Res. 2018 Apr;341:154–75.

26. Dixon SJ, Lemberg KM, Lamprecht MR, Skouta R, Zaitsev EM, Gleason CE, et al. Ferroptosis: An Iron-Dependent Form of Nonapoptotic Cell Death. Cell. 2012 May 25;149(5):1060–72.
27. Yang WS, Kim KJ, Gaschler MM, Patel M, Shchepinov MS, Stockwell BR. Peroxidation of polyunsaturated fatty acids by lipoxygenases drives ferroptosis. Proc Natl Acad Sci U S A. 2016;113(34):E4966–75.
28. Yang WS, Sriramaratnam R, Welsch ME, Shimada K, Skouta R, Viswanathan VS, et al. Regulation of ferroptotic cancer cell death by GPX4. Cell. 2014;
29. Shen J, Sheng X, Chang ZN, Wu Q, Wang S, Xuan Z, et al. Iron metabolism regulates p53 signaling through direct Heme-p53 interaction and modulation of p53 localization, stability, and function. Cell Rep. 2014;7(1):180–93.
30. Sfera A, Bullock K, Price A, Inderias L, Osorio C. Ferrosenescence: The iron age of neurodegeneration? Mech Ageing Dev. 2018 Sep;174(November):63–75.
31. Sturm Á, Ivics Z, Vellai T. The mechanism of ageing: Primary role of transposable elements in genome disintegration. Cell Mol Life Sci. 2015;72(10):1839–47.
32. Orr WC. Tightening the connection between transposable element mobilization and aging. Proc Natl Acad Sci. 2016 Oct 4;113(40):11069–70.
33. Bulk M, Van Der Weerd L, Breimer W, Lebedev N, Webb A, Goeman JJ, et al. Quantitative comparison of different iron forms in the temporal cortex of Alzheimer patients and control subjects. Sci Rep. 2018;8(1).
34. Stankiewicz JM, Brass SD. Role of iron in neurotoxicity: A cause for concern in the elderly? Vol. 12, Current Opinion in Clinical Nutrition and Metabolic Care. 2009. p. 22–9.
35. Kell DB. Iron behaving badly: Inappropriate iron chelation as a major contributor to the aetiology of vascular and other progressive inflammatory and degenerative diseases. BMC Med Genomics. 2009;2.
36. Braak H, Alafuzoff I, Arzberger T, Kretzschmar H, Del Tredici K. Staging of Alzheimer disease-associated neurofibrillary pathology using paraffin sections and immunocytochemistry. Acta Neuropathol. 2006 Oct 12;112(4):389–404.
37. Wayne Martin WR, Ye FQ, Allen PS, Martin WRW, Ye FQ, Allen PS. Increasing striatal iron content associated with normal aging. Mov Disord. 1998 Mar;13(2):281–6.
38. Hallgren B, Sourander P. THE EFFECT OF AGE ON THE NON-HAEMIN IRON IN THE HUMAN BRAIN. J Neurochem. 1958 Oct;3(1):41–51.

39. Apostolakis S, Kypraiou A-M. Iron in neurodegenerative disorders: being in the wrong place at the wrong time? Rev Neurosci. 2017 Nov 27;28(8):893–911.
40. Daugherty A, Raz N. Age-related differences in iron content of subcortical nuclei observed in vivo: A meta-analysis. Neuroimage. 2013 Apr;70:113–21.
41. Galazka-Friedman J, Friedman A, Bauminger ER. Iron in the brain. Hyperfine Interact. 2009;189(1–3):31–7.
42. Langkammer C, Krebs N, Goessler W, Scheurer E, Ebner F, Yen K, et al. Quantitative MR Imaging of Brain Iron: A Postmortem Validation Study 1. Radiology. 2010;257(November):455–62.
43. Krebs N, Langkammer C, Goessler W, Ropele S, Fazekas F, Yen K, et al. Assessment of trace elements in human brain using inductively coupled plasma mass spectrometry. J Trace Elem Med Biol. 2014;28(1):1–7.
44. Aquino D, Bizzi A, Grisoli M, Garavaglia B, Bruzzone MG, Nardocci N, et al. Age-related iron deposition in the basal ganglia: Quantitative analysis in healthy subjects. Radiology. 2009;252(1):165–72.
45. Péran P, Hagberg G, Luccichenti G, Cherubini A, Brainovich V, Celsis P, et al. Voxel-based analysis of R2* maps in the healthy human brain. J Magn Reson Imaging. 2007;26(6):1413–20.
46. Rodrigue KM, Haacke EM, Raz N. Differential effects of age and history of hypertension on regional brain volumes and iron. Neuroimage. 2011;
47. Magaki S, Raghavan R, Mueller C, Oberg KC, Vinters H V., Kirsch WM. Iron, copper, and iron regulatory protein 2 in Alzheimer's disease and related dementias. Neurosci Lett. 2007 May;418(1):72–6.
48. Schrag M, Mueller C, Oyoyo U, Smith MA, Kirsch WM. Iron, zinc and copper in the Alzheimer's disease brain: A quantitative meta-analysis. Some insight on the influence of citation bias on scientific opinion. Prog Neurobiol. 2011;94(3):296–306.
49. Xu X, Wang Q, Zhang M. Age, gender, and hemispheric differences in iron deposition in the human brain: An in vivo MRI study. Neuroimage. 2008 Mar 1;40(1):35–42.
50. Galazka-Friedman J, Bauminger ER, Szlachta K, Friedman A. The role of iron in neurodegeneration—Mössbauer spectroscopy, electron microscopy, enzyme-linked immunosorbent assay and neuroimaging studies. J Phys Condens Matter. 2012 Jun 20;24(24):244106.

51. Zatta P, Lucchini R, van Rensburg SJ, Taylor A. The role of metals in neurodegenerative processes: aluminum, manganese, and zinc. Brain Res Bull. 2003 Nov;62(1):15–28.
52. Liu G, Huang W, Moir RD, Vanderburg CR, Lai B, Peng Z, et al. Metal exposure and Alzheimer's pathogenesis. J Struct Biol. 2006 Jul;155(1):45–51.
53. Zecca L, Stroppolo A, Gatti A, Tampellini D, Toscani M, Gallorini M, et al. The role of iron and molecules in the neuronal vulnerability of locus coeruleus and substantia nigra during aging. Proc Natl Acad Sci U S A. 2004;101(26):9843–8.
54. Liu J-L, Fan Y-G, Yang Z-S, Wang Z-Y, Guo C. Iron and Alzheimer's Disease: From Pathogenesis to Therapeutic Implications. Front Neurosci. 2018 Sep 10;12(SEP).
55. Russo N, Edwards M, Andrews T, O'Brien M, Bhatia KP. Hereditary haemochromatosis is unlikely to cause movement disorders: A critical review. J Neurol. 2004;251(7):849–52.
56. Moos T, Nielsen TR, Skjørringe T, Morgan EH. Iron trafficking inside the brain. J Neurochem. 2007;103(5):1730–40.
57. Connor JR, Menzies SL, Martin SM St., Mufson EJ. Cellular distribution of transferrin, ferritin, and iron in normal and aged human brains. J Neurosci Res. 1990 Dec;27(4):595–611.
58. Benkovic SA, Connor JR. Ferritin, transferrin, and iron in selected regions of the adult and aged rat brain. J Comp Neurol. 1993;
59. Connor JR, Pavlick G, Karli D, Menzies SL, Palmer C. A histochemical study of iron-positive cells in the developing rat brain. J Comp Neurol. 1995 Apr 24;355(1):111–23.
60. Connor JR, Menzies SL. Relationship of iron to oligodendrocytes and myelination. Glia. 1996;17(2):83–93.
61. Todorich B, Pasquini JM, Garcia CI, Paez PM, Connor JR. Oligodendrocytes and myelination: The role of iron. Glia. 2009;57(5):467–78.
62. Bartzokis G. Schizophrenia: Breakdown in the well-regulated lifelong process of brain development and maturation. Neuropsychopharmacology. 2002;27(4):672–83.
63. Zhang P, Land W, Lee S, Juliani J, Lefman J, Sophia R, et al. Abnormal Regulation of Iron Metabolism. Biomed Eng (NY). 2006;150(2):144–53.
64. Cheepsunthorn P, Palmer C, Connor JR. Cellular distribution of ferritin subunits in postnatal rat brain. J Comp Neurol. 1998;400(1):73–86.

65. Codazzi F, Pelizzoni I, Zacchetti D, Grohovaz F. Iron entry in neurons and astrocytes: A link with synaptic activity. Front Mol Neurosci. 2015;8(June):1–6.
66. Hentze MW, Muckenthaler MU, Galy B, Camaschella C. Two to Tango: Regulation of Mammalian Iron Metabolism. Cell. 2010.
67. Wang J, Pantopoulos K. Regulation of cellular iron metabolism. Biochem J. 2011;434(3):365–81.
68. Zhou ZD, Tan EK. Iron regulatory protein (IRP)-iron responsive element (IRE) signaling pathway in human neurodegenerative diseases. Mol Neurodegener. 2017;12(1):1–12.
69. Lane DJR, Robinson SR, Czerwinska H, Bishop GM, Lawen A. Two routes of iron accumulation in astrocytes: ascorbate-dependent ferrous iron uptake via the divalent metal transporter (DMT1) plus an independent route for ferric iron. Biochem J. 2010 Nov 15;432(1):123–32.
70. Tulpule K, Robinson SR, Bishop GM, Dringen R. Uptake of ferrous iron by cultured rat astrocytes. J Neurosci Res. 2010;88(3):563–71.
71. Ransohoff RM, Perry VH. Microglial Physiology: Unique Stimuli, Specialized Responses. Annu Rev Immunol. 2009 Apr;27(1):119–45.
72. Ransohoff RM, Cardona AE. The myeloid cells of the central nervous system parenchyma. Nature. 2010 Nov 10;468(7321):253–62.
73. Mittelbronn M, Dietz K, Schluesener HJ, Meyermann R. Local distribution of microglia in the normal adult human central nervous system differs by up to one order of magnitude. Acta Neuropathol. 2001 Mar;101(3):249–55.
74. Ginhoux F, Prinz M. Origin of microglia: Current concepts and past controversies. Cold Spring Harb Perspect Biol. 2015;7(8):1–15.
75. Jara H, Sakai O, Mankal P, Irving RP, Norbash AM. Multispectral quantitative magnetic resonance imaging of brain iron stores: A theoretical perspective. Top Magn Reson Imaging. 2006 Feb;17(1):19–30.
76. Crichton RR, Declercq J-P. X-ray structures of ferritins and related proteins. Biochim Biophys Acta - Gen Subj. 2010 Aug;1800(8):706–18.
77. Harrison PM, Arosio P. The ferritins: molecular properties, iron storage function and cellular regulation. Biochim Biophys Acta. 1996 Jul 31;1275(3):161–203.
78. Blissman G, Menzies SL, Beard J, Palmer C, Connor J. The Expression of Ferritin Subunits and Iron in Oligodendrocytes in Neonatal Porcine Brains. Dev Neurosci. 1996;18(4):274–81.

79. Ferreira C, Bucchini D, Martin ME, Levi S, Arosio P, Grandchamp B, et al. Early embryonic lethality of H ferritin gene deletion in mice. J Biol Chem. 2000;275(5):3021–4.
80. Ferreira C, Santambrogio P, Martin ME, Andrieu V, Feldmann G, Hénin D, et al. H ferritin knockout mice: A model of hyperferritinemia in the absence of iron overload. Blood. 2001;
81. Theil EC. Ferritin: The Protein Nanocage and Iron Biomineral in Health and in Disease. Roach HI, Bronner F, Oreffo ROC, editors. Inorg Chem. 2013 Nov 4;52(21):12223–33.
82. Theil EC. Ferritin Protein Nanocages Use Ion Channels, Catalytic Sites, and Nucleation Channels To Manage Iron/Oxygen Chemistry: A review for: Current Opinion In Chemical Biology/Bioinorganic Chemistry: Iron Biochemistry. Curr Opin Chem Biol. 2011;15(2):304–11.
83. Jian N, Dowle M, Horniblow RD, Tselepis C, Palmer RE. Morphology of the ferritin iron core by aberration corrected scanning transmission electron microscopy. Nanotechnology. 2016 Nov 18;27(46):1–7.
84. La A, Nguyen T, Tran K, Sauble E, Tu D, Gonzalez A, et al. Mobilization of iron from ferritin: new steps and details. Metallomics. 2018;10(1):154–68.
85. Ruska E. The Development of the Electron Microscope and of Electron Microscopy (Nobel Lecture). Angew Chemie Int Ed English. 1987;26(7):595–605.
86. Smiley JF, Morrell F, Mesulam MM. Cholinergic synapses in human cerebral cortex: An ultrastructural study in serial sections. Exp Neurol. 1997;
87. GRAY EG. Electron Microscopy of Synaptic Contacts on Dendrite Spines of the Cerebral Cortex. Nature. 1959 Jun;183(4675):1592–3.
88. Mikula S, Binding J, Denk W. Staining and embedding the whole mouse brain for electron microscopy. Nat Methods. 2012;9(12):1198–201.
89. Lichtman JW, Denk W. The Big and the Small: Challenges of Imaging the Brain's Circuits. Science (80-). 2011;334(6056):618–23.
90. Briggman KL, Denk W. Towards neural circuit reconstruction with volume electron microscopy techniques. Curr Opin Neurobiol. 2006 Oct;16(5):562–70.
91. Mikula S, Denk W. High-resolution whole-brain staining for electron microscopic circuit reconstruction. Nat Methods. 2015;12(6):541–6.
92. Kleinfeld D, Bharioke a., Blinder P, Bock DD, Briggman KL, Chklovskii DB, et al. Large-Scale Automated Histology in the Pursuit of Connectomes. J Neurosci.

2011;31(45):16125–38.

93. Erni R, Rossell MD, Kisielowski C, Dahmen U. Atomic-Resolution Imaging with a Sub-50-pm Electron Probe. Phys Rev Lett. 2009 Mar 2;102(9):096101.
94. Luse SA. Electron microscopic observations of the central nervous system. J Cell Biol. 1956;2(5):531–42.
95. CRAGG BG. THE DENSITY OF SYNAPSES AND NEURONS IN NORMAL, MENTALLY DEFECTIVE AND AGEING HUMAN BRAINS. Brain. 1975;98(1):81–90.
96. Scheff SW, Price DA. Synaptic pathology in Alzheimer's disease: A review of ultrastructural studies. In: Neurobiology of Aging. 2003.
97. Domínguez-Álvaro M, Montero-Crespo M, Blazquez-Llorca L, DeFelipe J, Alonso-Nanclares L. 3D Electron Microscopy Study of Synaptic Organization of the Normal Human Transentorhinal Cortex and Its Possible Alterations in Alzheimer's Disease. Eneuro. 2019;6(4):ENEURO.0140-19.2019.
98. Lehrer J. Neuroscience: Making connections. Nature. 2009 Jan 28;457(7229):524–7.
99. White JGG, Southgate E, Thomson JNN, Brenner S. The Structure of the Nervous System of the Nematode Caenorhabditis elegans. Philos Trans R Soc B Biol Sci. 1986 Nov 12;314(1165):1–340.
100. Schalek R, Wilson a., Lichtman J, Josh M, Kasthuri N, Berger D, et al. ATUM-based SEM for High-Speed Large-Volume Biological Reconstructions. Microsc Microanal. 2012;18(S2):572–3.
101. Hayworth KJ, Morgan JL, Schalek R, Berger DR, Hildebrand DGC, Lichtman JW. Imaging ATUM ultrathin section libraries with WaferMapper: a multi-scale approach to EM reconstruction of neural circuits. Front Neural Circuits. 2014;8(June):1–18.
102. Lucia MS HK and TJDC. The big data challenges of connectomics. Nat Neurosci. 2014 Nov 28;17(11):1448–54.
103. Adrian M, Dubochet J, Lepault J, McDowall AW. Cryo-electron microscopy of viruses. Nature. 1984 Mar;308(5954):32–6.
104. Cressey D, Callaway E. Cryo-electron microscopy wins chemistry Nobel. Nature. 2017 Oct 12;550(7675):167–167.
105. Aronova MA, Kim YC, Pivovarova NB, Andrews SB, Leapman RD. Quantitative EFTEM mapping of near physiological calcium concentrations in biological

specimens. Ultramicroscopy. 2009;109(3):201–12.

106. Aronova MA, Leapman RD. Development of Electron Energy Loss Spectroscopy in the Biological Sciences. MRS Bull. 2012 Jan;37(1):53–62.
107. Lipovšek S, Letofsky-Papst I, Hofer F, Leitinger G, Devetak D. The evidence on the degradation processes in the midgut epithelial cells of the larval antlion Euroleon nostras (Geoffroy in Fourcroy, 1785) (Myrmeleontidae, Neuroptera). Micron. 2012 Apr;43(5):651–65.
108. Rhinow D, Büenfeld M, Weber N-E, Beyer A, Gölzhäuser A, Kühlbrandt W, et al. Energy-filtered transmission electron microscopy of biological samples on highly transparent carbon nanomembranes. Ultramicroscopy. 2011;111(5):342–9.
109. Hofer F, Warbichler P, Grogger W. Imaging of nanometer-sized precipitates in solids by electron spectroscopic imaging. Ultramicroscopy. 1995 Jul;59(1–4):15–31.
110. Verbeeck J, Van Dyck D, Van Tendeloo G. Energy-filtered transmission electron microscopy: an overview. Spectrochim Acta Part B At Spectrosc. 2004 Oct;59(10–11):1529–34.
111. Egerton RF. Electron Energy-Loss Spectroscopy in the Electron Microscope. 2nd editio. Boston, MA: Springer US; 1996.
112. Berger A, Kohl H. Elemental mapping using an imaging energy filter: image formation and resolution limits. Microsc Microanal Microstruct. 1992;3(2–3):159–74.
113. D'Amico F, Skarmoutsou E. Quantifying immunogold labelling in transmission electron microscopy. J Microsc. 2008;230(1):9–15.
114. Page Faulk W, Malcolm Taylor G. Communication to the editors: An immunocolloid method for the electron microscope. Immunochemistry. 1971 Nov;8(11):1081–3.
115. Bittermann AG, Knoll G, Németh A, Plattner H. Quantitative immuno-gold labelling and ultrastructural preservation after cryofixation (combined with different freeze-substitution and embedding protocols) and after chemical fixation and cryosectioning. Histochemistry. 1992;97(5):421–9.
116. Hess MW, Vogel GF, Yordanov TE, Witting B, Gutleben K, Ebner HL, et al. Combining high-pressure freezing with pre-embedding immunogold electron microscopy and tomography. Traffic. 2018;19(8):639–49.
117. Gulati NM, Torian U, Gallagher JR, Harris AK. Immunoelectron Microscopy of Viral Antigens. Curr Protoc Microbiol. 2019 Jun 20;53(1):1–18.

118. Dosemeci A, Makusky AJ, Jankowska-Stephens E, Yang X, Slotta DJ, Markey SP. Composition of the Synaptic PSD-95 Complex. Mol Cell Proteomics. 2007 Oct;6(10):1749–60.
119. Dosemeci A, Loo HK, Toy D, Winters CA, Reese TS, Tao-Cheng J-HH. FAM81A protein, a novel component of the postsynaptic density in adult brain. Neurosci Lett. 2019 Apr;699:122–6.
120. Vass A. Beyond the grave – understanding human decomposition. Microbiol Today. 2001;28(28):190–2.
121. Zhou C, Byard RW. Factors and processes causing accelerated decomposition in human cadavers - An overview. J Forensic Leg Med. 2011;18(1):6–9.
122. Zemirli N, Morel E, Molino D. Mitochondrial dynamics in basal and stressful conditions. Int J Mol Sci. 2018;19(2):1–19.
123. Henstridge CM, Jackson RJ, Kim JSM, Herrmann AG, Wright AK, Harris SE, et al. Post-mortem brain analyses of the Lothian Birth Cohort 1936: extending lifetime cognitive and brain phenotyping to the level of the synapse. Acta Neuropathol Commun. 2015;3:53.
124. Kay KR, Smith C, Wright AK, Serrano-Pozo A, Pooler AM, Koffie R, et al. Studying synapses in human brain with array tomography and electron microscopy. Nat Protoc. 2013;8(7):1366–80.
125. Krause M, Brüne M, Theiss C. Preparation of human formalin-fixed brain slices for electron microscopic investigations. Ann Anat. 2016;206:27–33.
126. Zemmoura I, Blanchard E, Raynal PI, Rousselot-Denis C, Destrieux C, Velut S. How Klingler's dissection permits exploration of brain structural connectivity? An electron microscopy study of human white matter. Brain Struct Funct. 2016;221(5):2477–86.
127. Glausier JR, Roberts RC, Lewis DA. Ultrastructural analysis of parvalbumin synapses in human dorsolateral prefrontal cortex. J Comp Neurol. 2017 Jun 15;525(9):2075–89.
128. Glausier JR, Konanur A, Lewis DA. Factors Affecting Ultrastructural Quality in the Prefrontal Cortex of the Postmortem Human Brain. J Histochem Cytochem. 2019;67(3):185–202.
129. Berlet HH, Volk B. Studies of human myelin proteins during old age. Mech Ageing Dev. 1980 Sep;14(1–2):211–22.
130. Bando Y, Nomura T, Bochimoto H, Murakami K, Tanaka T, Watanabe T, et al.

Abnormal morphology of myelin and axon pathology in murine models of multiple sclerosis. Neurochem Int. 2015 Feb;81:16–27.

131. Maneta-Peyret L, Compère P, Moreau P, Goffinet G, Cassagne C. Immunocytochemistry of lipids: Chemical fixatives have dramatic effects on the preservation of tissue lipids. Histochem J. 1999;31(8):541–7.
132. Vanhecke D, Graber W, Herrmann G, Al-Amoudi A, Eggli P, Studer D. A rapid microbiopsy system to improve the preservation of biological samples prior to high-pressure freezing. J Microsc. 2003 Oct;212(Pt 1):3–12.
133. Studer D, Humbel BM, Chiquet M. Electron microscopy of high pressure frozen samples: Bridging the gap between cellular ultrastructure and atomic resolution. Histochem Cell Biol. 2008;130(5):877–89.
134. Mcdonald KL, Auer M. Tech Insight High-Pressure Freezing , Cellular Tomography , and Structural Cell Biology Sample Preservation for Biological Electron. Biotechniques. 2006;41(2):1–4.
135. Möbius W, Nave KA, Werner HB. Electron microscopy of myelin: Structure preservation by high-pressure freezing. Brain Res. 2016;1641:92–100.
136. Korogod N, Petersen CCH, Knott GW. Ultrastructural analysis of adult mouse neocortex comparing aldehyde perfusion with cryo fixation. Elife. 2015;4(AUGUST2015):1–17.
137. Möbius W, Cooper B, Kaufmann WA, Imig C, Ruhwedel T, Snaidero N, et al. Electron microscopy of the mouse central nervous system. Vol. 96, Methods in Cell Biology. 2010. 475–512 p.
138. Kellenberger E. The Response of Biological Macromolecules and Supramolecular Structures to the Physics of Specimen Cryopreparation. In: Cryotechniques in Biological Electron Microscopy. Berlin, Heidelberg, Heidelberg: Springer Berlin Heidelberg; 1987. p. 35–63.
139. Möbius W. Cryopreparation of biological specimens for immunoelectron microscopy. Ann Anat. 2009 Jun;191(3):231–47.
140. Goldammer H, Hollergschwandtner E, Elisabeth NH, Frade PR, Reipert S. Automatized Freeze Substitution of Algae Accelerated by a Novel Agitation Module. Protist. 2016;167(4):369–76.
141. Goldammer H, Reipert S. Freeze Substitution Device. Austria; AT515423, 2015.
142. Reipert S, Goldammer H, Richardson C, Goldberg MW, Hawkins TJ, Hollergschwandtner E, et al. Agitation Modules: Flexible Means to Accelerate

Automated Freeze Substitution. J Histochem Cytochem. 2018;66(12).

143. Tsang TK, Bushong EA, Boassa D, Hu J, Romoli B, Phan S, et al. High-quality ultrastructural preservation using cryofixation for 3d electron microscopy of genetically labeled tissues. Elife. 2018;7:1–23.
144. Sosinsky GE, Crum J, Jones YZ, Lanman J, Smarr B, Terada M, et al. The combination of chemical fixation procedures with high pressure freezing and freeze substitution preserves highly labile tissue ultrastructure for electron tomography applications. J Struct Biol. 2008 Mar;161(3):359–71.
145. Braak H, Braak E. Neuropathological stageing of Alzheimer-related changes. Acta Neuropathol. 1991;82(4):239–59.
146. Sele M, Wernitznig S, Lipovšek S, Radulović S, Haybaeck J, Birkl-Toeglhofer AM, et al. Optimization of ultrastructural preservation of human brain for transmission electron microscopy after long post-mortem intervals. Acta Neuropathol Commun. 2019;7(1):144.
147. Sridharan G, Shankar A. Toluidine blue: A review of its chemistry and clinical utility. J Oral Maxillofac Pathol. 2012;16(2):251.
148. Ghnenis AB, Czaikowski RE, Zhang ZJ, Bushman JS. Toluidine Blue Staining of Resin-Embedded Sections for Evaluation of Peripheral Nerve Morphology. J Vis Exp. 2018;(137):1–7.
149. Wernitznig S, Reichmann F, Sele M, Birkl C, Haybäck J, Kleinegger F, et al. An Unbiased Approach of Sampling TEM Sections in Neuroscience. J Vis Exp. 2019 Apr 13;(146):1–9.
150. Schinagl M. Localising Ferritin and Iron in Human Brain Tissue using Immuno-Electron Microscopy. Graz University of Technology; 2018.
151. Huendler M. Isolating the iron storage protein ferritin from human brain tissue and characterizing its iron core via electron microscopic techniques. Graz University of Technology; 2019.
152. Jones TR, Kang IH, Wheeler DB, Lindquist RA, Papallo A, Sabatini DM, et al. CellProfiler Analyst: data exploration and analysis software for complex image-based screens. BMC Bioinformatics. 2008 Nov 15;9:482.
153. Mcdonald KL, Webb RI. Freeze substitution in 3 hours or less. J Microsc. 2011;243(3):227–33.
154. Howard C V., Reed MG. Unbiased Steriology. Oxford: BIOS Scientific Publishers Limited; 1998.

155. Chomiak T, Hu B. What is the optimal value of the g-ratio for myelinated fibers in the rat CNS? A theoretical approach. PLoS One. 2009;4(11).
156. Zhang P, Land W, Lee S, Juliani J, Lefman J, Smith SR, et al. Electron tomography of degenerating neurons in mice with abnormal regulation of iron metabolism. J Struct Biol. 2005 May;150(2):144–53.
157. Kopek BG, Paez-Segala MG, Shtengel G, Sochacki KA, Sun MG, Wang Y, et al. Diverse protocols for correlative super-resolution fluorescence imaging and electron microscopy of chemically fixed samples. Nat Protoc. 2017;12(5):916–46.
158. Burette AC, Lesperance T, Crum J, Martone M, Volkmann N, Ellisman MH, et al. Electron tomographic analysis of synaptic ultrastructure. J Comp Neurol. 2012;520(12):2697–711.
159. Thelwall PE, Shepherd TM, Stanisz GJ, Blackband SJ. Effects of temperature and aldehyde fixation on tissue water diffusion properties, studied in an erythrocyte ghost tissue model. Magn Reson Med. 2006;56(2):282–9.
160. McDonald KL. Out with the old and in with the new: Rapid specimen preparation procedures for electron microscopy of sectioned biological material. Protoplasma. 2014;251(2):429–48.
161. Dubochet J. The Physics of Rapid Cooling and Its Implications for Cryoimmobilization of Cells. Methods Cell Biol. 2007;2007(79):7–21.
162. Schwab M, Bauer R, Zwiener U. The distribution of normal brain water content in Wistar rats and its increase due to ischemia. Brain Res. 1997 Feb 21;749(1):82–7.
163. Buser C, Walther P. Freeze-substitution: The addition of water to polar solvents enhances the retention of structure and acts at temperatures around -60°C. J Microsc. 2008;230(2):268–77.
164. McDonald K. Cryopreparation methods for electron microscopy of selected model systems. Methods Cell Biol. 2007;79(79):23–56.
165. McDonald K, Schwarz H, Müller-Reichert T, Webb R, Buser C, Morphew M. “Tips and Tricks” for High-Pressure Freezing of Model Systems. In: Methods in Cell Biology. Elsevier Inc.; 2010. p. 671–93.
166. Weibull C, Villiger W, Carlemalm E. Extraction of lipids during freeze-substitution of Acholeplasma laidlawii-cells for electron microscopy. J Microsc. 1984 May;134(Pt 2):213–6.
167. Echlin P. The Process of Interpreting Images Obtained by Scanning Electron Microscopy. Microsc Microanal. 2005 Aug 1;11(S02):1320–1.

168. Leal NS, Dentoni G, Schreiner B, Kämäräinen OP, Partanen N, Herukka SK, et al. Alterations in mitochondria-endoplasmic reticulum connectivity in human brain biopsies from idiopathic normal pressure hydrocephalus patients. Acta Neuropathol Commun. 2018;6(1):102.
169. Xu M, Zhang H. Death and survival of neuronal and astrocytic cells in ischemic brain injury : a role of autophagy. Nat Publ Gr. 2011;32(9):1089–99.
170. Liu X, Schumann CM. Optimization of electron microscopy for human brains with long-term fixation and fixed-frozen sections. Acta Neuropathol Commun. 2014 Dec 11;2(1):42.
171. Emma P-C, Melendez-Ferro M, Roberts. RC. Microscopy techniques and the study of synapses. Mod Res Educ Top Microsc. 2007;(May):164–70.
172. Dean B. Using CNS Autopsy Tissue in Psychiatric Research: A Practical Guide. Dean B, Kleinmann J, Hyde T, editors. Using CNS issue in psychiatric research. CRC Press; 2014. 127–40 p.
173. King MV. Dimensional changes in cells and tissues during specimen preparation for the electron microscope. Cell Biophys. 1991 Feb;18(1):31–55.
174. Pan YH, Sader K, Powell JJ, Bleloch A, Gass M, Trinick J, et al. 3D morphology of the human hepatic ferritin mineral core: New evidence for a subunit structure revealed by single particle analysis of HAADF-STEM images. J Struct Biol. 2009;166(1):22–31.
175. Leapman RD. Detecting single atoms of calcium and iron in biological structures by electron energy-loss spectrum-imaging. J Microsc. 2003;210(1):5–15.
176. Shuman H, Somlyo AP. Electron energy loss analysis of near-trace-element concentrations of calcium. Ultramicroscopy. 1987 Jan;21(1):23–32.
177. Leapman RD, Hunt JA, Buchanan RA, Andrews SB. Measurement of low calcium concentrations in cryosectioned cells by parallel-EELS mapping. Ultramicroscopy. 1993 Feb;49(1–4):225–34.
178. Kothleitner G, Hofer F. Optimization of the Signal to Noise Ratio in EFTEM Elemental Maps with Regard to Different Ionization Edge Types. Micron. 1998 Oct;29(5):349–57.
179. Grogger W, Hofer F, Kothleitner G. Quantitative chemical phase imaging by means of energy filtering transmission electron microscopy. Mikrochim Acta. 1997 Mar;125(1–4):13–9.
180. Hofer F, Grogger W, Kothleitner G, Warbichler P. Quantitative analysis of EFTEM

elemental distribution images. Ultramicroscopy. 1997 Jun;67(1–4):83–103.

181. Pun T, Ellis JR, Eden M. Optimized acquisition parameters and statistical detection limit in quantitative EELS. J Microsc. 1984 Sep;135(3):295–316.
182. Lozano-Perez S, Titchmarsh JM. EFTEM assistant: A tool to understand the limitations of EFTEM. Ultramicroscopy. 2007;
183. Heil T, Kohl H. Optimization of EFTEM image acquisition by using elastically filtered images for drift correction. Ultramicroscopy. 2010 Jun;110(7):745–50.
184. Cai S, Tsui YP, Tam KW, Shea GKH, Chang RSK, Ao Q, et al. Directed Differentiation of Human Bone Marrow Stromal Cells to Fate-Committed Schwann Cells. Stem Cell Reports. 2017 Oct;9(4):1097–108.
185. Wong FK, Fei JF, Mora-bermúdez F, Taverna E, Haffner C, Fu J, et al. Sustained pax6 expression generates primate-like basal radial glia in developing mouse neocortex. Khaitovich P, editor. PLoS Biol. 2015 Aug 7;13(8):e1002217.
186. Alamir H, Alomari M, Salwati AAA, Saka M, Bangash M, Baeesa S, et al. In situ characterization of stem cells-like biomarkers in meningiomas. Cancer Cell Int. 2018;18(1):1–14.
187. Orlova KA, Parker WE, Heuer GG, Tsai V, Yoon J, Baybis M, et al. STRADα deficiency results in aberrant mTORC1 signaling during corticogenesis in humans and mice. J Clin Invest. 2010 May 3;120(5):1591–602.
188. Riquelme D, Silva I, Philp AM, Huidobro-Toro JP, Cerda O, Trimmer JS, et al. Subcellular localization and activity of TRPM4 in medial prefrontal cortex layer 2/3. Front Cell Neurosci. 2018 Jan 30;12(January):1–13.
189. Shi M, Bradner J, Bammler TK, Eaton DL, Zhang J, Ye Z, et al. Identification of Glutathione S -Transferase Pi as a Protein Involved in Parkinson Disease Progression. 2009;175(1):54–65.
190. Xia Y, Zhang G, Han C, Ma K, Guo X, Wan F, et al. Microglia as modulators of exosomal alpha-synuclein transmission. Cell Death Dis. 2019;10(3).
191. Magalhaes J, Gegg ME, Migdalska-Richards A, Schapira AH. Effects of ambroxol on the autophagy-lysosome pathway and mitochondria in primary cortical neurons. Sci Rep. 2018;8(1):1–12.
192. Zhitomirsky B, Assaraf YG. Lysosomal accumulation of anticancer drugs triggers lysosomal exocytosis. Oncotarget. 2017;8(28):45117–32.
193. Schrag M, Dickson A, Jiffry A, Kirsch D, Vinters H V., Kirsch W. The effect of formalin fixation on the levels of brain transition metals in archived samples.

BioMetals. 2010 Dec 26;23(6):1123–7.

194. Ferrer I, Armstrong J, Capellari S, Parchi P, Arzberger T, Bell J, et al. Effects of formalin fixation, paraffin embedding, and time of storage on DNA preservation in brain tissue: A brainnet Europe study. Brain Pathol. 2007;17(3):297–303.
195. Bussolati G, Annaratone L, Medico E, D'Armento G, Sapino A. Formalin Fixation at Low Temperature Better Preserves Nucleic Acid Integrity. Wong C-M, editor. PLoS One. 2011 Jun 15;6(6):e21043.
196. Bush VJ, Moyer TP, Batts KP, Parisi JE. Essential and toxic element concentrations in fresh and formalin-fixed human autopsy tissues. Clin Chem. 1995;41(2):284–94.
197. Gellein K, Flaten TP, Erikson KM, Aschner M, Syversen T. Leaching of Trace Elements from Biological Tissue by Formalin Fixation. Biol Trace Elem Res. 2008 Mar 19;121(3):221–5.
198. Bischoff K, Lamm C, Erb HN, Hillebrandt JR. The effects of formalin fixation and tissue embedding of bovine liver on copper, iron, and zinc analysis. J Vet Diagnostic Investig. 2008;20(2):220–4.
199. Langkammer C, Krebs N, Goessler W, Scheurer E, Yen K, Fazekas F, et al. Susceptibility induced gray–white matter MRI contrast in the human brain. Neuroimage. 2012 Jan;59(2):1413–9.
200. Langkammer C, Schweser F, Krebs N, Deistung A, Goessler W, Scheurer E, et al. Quantitative susceptibility mapping (QSM) as a means to measure brain iron? A post mortem validation study. Neuroimage. 2012 Sep;62(3):1593–9.
201. Harrison WW, Netsky MG, Brown MD. Trace elements in human brain: Copper, zinc, iron, and magnesium. Clin Chim Acta. 1968 Jul;21(1):55–60.
202. Goldberg WJ, Allen N. Determination of Cu, Mn, Fe, and Ca in six regions of normal human brain, by atomic absorption spectroscopy. Clin Chem. 1981;27(4):562–4.
203. DEXTER DT, CARAYON A, JAVOY-AGID F, AGID Y, WELLS FR, DANIEL SE, et al. ALTERATIONS IN THE LEVELS OF IRON, FERRITIN AND OTHER TRACE METALS IN PARKINSON'S DISEASE AND OTHER NEURODEGENERATIVE DISEASES AFFECTING THE BASAL GANGLIA. Brain. 1991;114(4):1953–75.
204. van Duijn S, Bulk M, van Duinen SG, Nabuurs RJA, van Buchem MA, van der Weerd L, et al. Cortical Iron Reflects Severity of Alzheimer's Disease. J Alzheimer's Dis. 2017 Nov 7;60(4):1533–45.

205. Schenck JF. Imaging of brain iron by magnetic resonance: T2 relaxation at different field strengths. J Neurol Sci. 1995;
206. Anderson CM, Kaufman MJ, Lowen SB, Rohan M, Renshaw PF, Teicher MH. Brain T2 relaxation times correlate with regional cerebral blood volume. Magn Reson Mater Physics, Biol Med. 2005;18(1):3–6.
207. Jensen JH, Tang H, Tosti CL, Swaminathan S V, Nunez A, Hultman K, et al. Separate MRI quantification of dispersed (ferritin-like) and aggregated (hemosiderin-like) storage iron. Magn Reson Med. 2010 May;63(5):1201–9.
208. Ding B, Chen KM, Ling HW, Sun F, Li X, Wan T, et al. Correlation of iron in the hippocampus with MMSE in patients with alzheimer's disease. J Magn Reson Imaging. 2009;29(4):793–8.
209. Zhu W-ZZ, Zhong W De, Wang W, Zhan C-JJ, Wang C-YY, Qi J-PP, et al. Quantitative MR phase-corrected imaging to investigate increased brain iron deposition of patients with Alzheimer disease. Radiology. 2009;253(2):497–504.
210. Kirsch W, McAuley G, Holshouser B, Petersen F, Ayaz M, Vinters H V., et al. Serial Susceptibility Weighted MRI Measures Brain Iron and Microbleeds in Dementia. J Alzheimer's Dis. 2009 Jul 1;17(3):599–609.
211. Watanabe H, Ito M, Fukatsu H, Senda J, Atsuta N, Kaga T, et al. Putaminal magnetic resonance imaging features at various magnetic field strengths in multiple system atrophy. Mov Disord. 2010 Sep 15;25(12):1916–23.
212. Schrag A. Clinical usefulness of magnetic resonance imaging in multiple system atrophy. J Neurol Neurosurg Psychiatry. 1998;65(1):65–71.
213. Kraft E, Schwarz J, Trenkwalder C, Vogl T, Pfluger T, Oertel WH. The Combination of Hypointense and Hyperintense Signal Changes on T2-Weighted Magnetic Resonance Imaging Sequences. Arch Neurol. 1999 Feb 1;56(2):225.
214. Matsusue E, Fujii S, Kanasaki Y, Sugihara S, Miyata H, Ohama E, et al. Putaminal lesion in multiple system atrophy: postmortem MR-pathological correlations. Neuroradiology. 2008 Jul 8;50(7):559–67.
215. Kaindlstorfer C, Jellinger KA, Eschlböck S, Stefanova N, Weiss G, Wenning GK. The Relevance of Iron in the Pathogenesis of Multiple System Atrophy: A Viewpoint. J Alzheimer's Dis. 2018 Jan 23;61(4):1253–73.
216. Nandwana V, Ryoo S-R, Kanthala S, Kumar A, Sharma A, Castro FC, et al. Engineered ferritin nanocages as natural contrast agents in magnetic resonance imaging. RSC Adv. 2017;7(55):34892–900.

217. Sana B, Johnson E, Sheah K, Poh CL, Lim S. Iron-based ferritin nanocore as a contrast agent. Biointerphases. 2010 Sep;5(3):FA48–52.

218. Braak E, Braak H. Staging of Alzheimer ' s Disease-Related Neurofibrillary Changes. Neurobiol Aging. 1995;16(3):271–8.

219. Connor JR, Menzies SL, St. Martin SM, Mufson EJ. A histochemical study of iron, transferrin, and ferritin in Alzheimer's diseased brains. J Neurosci Res. 1992 Jan;31(1):75–83.

220. Tao Y, Wang Y, Rogers JT, Wang F. Perturbed Iron Distribution in Alzheimer's Disease Serum, Cerebrospinal Fluid, and Selected Brain Regions: A Systematic Review and Meta-Analysis. J Alzheimer's Dis. 2014 Aug 28;42(2):679–90.

221. Hare DJ, Raven EP, Roberts BR, Bogeski M, Portbury SD, McLean CA, et al. Laser ablation-inductively coupled plasma-mass spectrometry imaging of white and gray matter iron distribution in Alzheimer's disease frontal cortex. Neuroimage. 2016 Aug;137:124–31.

Appendix

Mass spectrometry

The trace element results determined by mass spectrometry for all measured brain samples are shown in Table 15.

Table 15: Sample overview of all measured mass spectrometry results for the human brain samples of this study; samples marked with question mark mean that Braak staging still under investigation.

Case	Brain region	PMI [h]	Braak & Braak NFT stage	Fe [mg/kg]	Mg [mg/kg]	Ca [mg/kg]	Cu [mg/kg]	Zn [mg/kg]
Fe270217	FGM	9	I	36.4	98.4	55.7	3.8	10.5
	FWM	9	I	75.8	151.9	48.7	5.0	10.6
	OGM	9	I	54.7	120.2	55.4	4.7	12.5
	OWM	9	I	63.4	132.3	41.7	3.9	9.8
	Put	9	I	175.8	146.1	49.8	7.7	14.6
	GP	9	I	115.5	152.4	52.4	5.7	10.7
Fe171031	FGM	16	I	19.6	65.8	86.7	2.0	9.2
	FWM	16	I	81.7	193.7	96.0	4.3	16.3
	OGM	16	I	76.5	106.3	63.1	6.4	14.3
	OWM	16	I	41.1	122.1	73.3	2.4	10.8
	Put	16	I	61.3	127.3	87.9	4.7	13.4
	GP	16	I	90.8	85.5	57.9	3.7	10.9
	SN	16	I	176.5	118.7	81.1	7.5	13.6
	CN	16	I	139.2	134.3	86.8	5.0	14.0
	PGM	16	I	30.2	93.5	134.3	2.9	13.4
	PWM	16	I	40.2	104.9	68.1	2.6	9.4
	TGM	16	I	21.1	78.9	58.3	2.3	12.5
	TWM	16	I	29.4	83.7	45.2	1.8	6.4
Fe171103	FGM	18	I	19.7	82.6	46.3	2.8	8.4
	FWM	18	I	35.3	104.5	38.7	2.8	6.5
	OGM	18	I	29.1	81.2	59.0	3.4	8.7
	OWM	18	I	34.0	94.4	33.4	2.6	5.2
	Put	18	I	59.6	123.6	52.8	5.1	11.2
	GP	18	I	40.4	101.7	46.5	5.0	6.1
	SN	18	I	44.0	64.1	54.2	4.7	4.7
	CN	18	I	20.8	82.8	37.5	3.3	4.4

	PGM	18	I	21.6	72.2	52.2	2.7	8.5
	PWM	18	I	34.5	107.0	56.2	2.8	5.6
	TGM	18	I	19.6	85.0	37.7	2.6	9.4
	TWM	18	I	34.0	99.4	33.2	2.5	5.7
Fe180223	FGM	24	VI	107.7	104.5	87.7	3.4	21.6
	FWM	24	VI	51.5	100.0	77.8	2.6	9.9
	OGM	24	VI	36.0	69.9	38.5	2.8	8.1
	OWM	24	VI	53.7	100.6	31.8	1.9	6.6
	Put	24	VI	146.6	118.5	48.5	5.0	13.3
	GP	24	VI	166.8	104.5	51.5	4.5	11.8
Fe180323	FGM	20	IV	32.9	90.1	51.1	3.7	12.2
	FWM	20	IV	44.7	122.1	45.9	3.0	8.5
	OGM	20	IV	43.1	100.9	48.8	4.3	13.4
	OWM	20	IV	55.3	119.1	41.7	3.0	10.0
	Put	20	IV	189.4	101.4	37.2	4.8	14.3
	GP	20	IV	54.8	127.1	45.2	3.9	9.7
	RN	20	IV	65.9	113.3	46.9	2.6	12.7
Fe180326	FGM	15.5	II	27.9	86.9	66.6	2.7	10.6
	FWM	15.5	II	53.2	117.8	45.7	3.1	8.8
	OGM	15.5	II	40.9	67.4	225.2	2.8	9.4
	OWM	15.5	II	40.3	84.8	44.0	1.7	6.2
	Put	15.5	II	144.4	117.4	80.4	5.8	15.0
	CN	15.5	II	145.6	107.4	47.8	4.3	12.1
Fe180615	FGM	19	I	23.3	56.8	46.7	2.0	10.4
	FWM	19	I	55.8	97.1	25.6	2.6	10.2
	OGM	19	I	47.2	77.3	41.1	3.9	13.1
	OWM	19	I	35.4	80.6	23.0	2.1	7.5
	GP	19	I	143.6	101.5	30.3	4.9	14.2
	SN	19	I	90.3	68.5	0.0	5.3	13.0
Fe181126	FGM	14.5	?	22.1	65.1	38.9	2.8	9.3
	FWM	14.5	?	22.9	96.3	50.7	2.8	6.9
	OGM	14.5	?	24.3	58.0	32.8	3.3	8.3
	OWM	14.5	?	22.6	81.3	34.4	2.3	5.8
	Put	14.5	?	122.1	104.2	42.3	5.0	11.8
	GP	14.5	?	271.6	96.6	43.7	5.5	13.0
	Th	14.5	?	32.6	98.0	50.3	4.3	9.2
Fe190215	FGM	19	?	34.7	78.7	32.8	3.7	9.6
	FWM	19	?	48.2	115.3	28.7	3.9	7.9

	OGM	19	?	48.8	144.2	45.0	4.7	9.0
	OWM	19	?	110.8	75.3	17.9	5.8	8.5
	Put	19	?	77.6	95.6	27.4	5.4	10.8
	GP	19	?	59.0	74.3	19.2	4.3	10.4
	Th	19	?	57.3	104.2	33.7	3.4	10.0
Fe190314	FGM	6.5	?	25.3	71.3	32.0	4.8	11.4
	FWM	6.5	?	52.0	100.9	38.7	5.9	10.6
	OGM	6.5	?	37.1	61.2	23.2	5.0	9.2
	OWM	6.5	?	31.0	90.5	40.5	5.4	8.8
	Put	6.5	?	91.2	79.4	33.1	5.3	11.8
	GP	6.5	?	38.4	58.1	8.2	4.9	7.6
	Th	6.5	?	64.5	109.2	35.0	6.6	13.4

EFTEM Images for evaluation

In Table 16 all used images for the evaluation of iron particles are listed. Excluded were images which were not located in the overview image, showed heavy drift, holes or parts of the grid, or overlap.

Table 16: List of all used images for the evaluation.

Case	Point	In overlay	Area b	Area c	Area l	Area r	Area t	Sum	Total
Fe270217 FGM	P1	5x	b		l	r	t	4	38
	P2	5x	b		l	r	t	4	
	P3	5x	b		l	r		3	
	P4	5x	b		l	r	t	4	
	P5	5x	b		l	r	t	4	
	P6	5x	b		l	r	t	4	
	P7	5x	b		l		t	3	
	P8	5x	b		l	r	t	4	
	P9	5x	b		l	r	t	4	
	P10	5x	b		l	r	t	4	
Fe270217 FWM	P1	1x	b					1	5
	P2	0x						0	
	P3	0x						0	
	P4	0x						0	
	P5	2x	b	c				2	
	P6	1x	b					1	
	P7	1x	b					1	
	P8	0x						0	
	P9	0x						0	
	P10	0x						0	
Fe270217 Put	P1	4x	b	c		r	t	4	39
	P2	0x						0	
	P3	5x	b		l	r	t	4	
	P4	5x	b		l	r	t	4	
	P5	5x	b		l	r	t	4	
	P6	5x	b		l	r	t	4	
	P7	5x	b		l	r	t	4	
	P8	5x	b		l	r	t	4	

	P9	5c	b			r	t	3	
	P10	5x	b		l	r	t	4	
	P11	1x	b					1	
	P12	5x	b		l	r		3	
Fe270217 GP	P1	5x	b	c	l	r	t	5	48
	P2	5x	b		l	r	t	4	
	P3	5x	b		l	r	t	4	
	P4	4x	b		l		t	3	
	P5	5x	b		l	r	t	4	
	P6	5x	b		l	r	t	4	
	P7	5x	b		l	r	t	4	
	P8	5x	b		l	r	t	4	
	P9	5x	b	c	l	r	t	5	
	P10	4x	b		l	r	t	4	
	P11	3x	b		l		t	3	
	P12	4x	b		l	r	t	4	
Fe171031 FGM	P1	4x	b		l	r	t	4	34
	P2	1x	b					1	
	P3	1x	b					1	
	P4	4x	b		l	r	t	4	
	P5	4x	b		l	r	t	4	
	P6	4x	b		l	r	t	4	
	P7	4x	b		l	r	t	4	
	P8	4x	b		l	r	t	4	
	P9	4x	b		l	r	t	4	
	P10	4x	b		l	r	t	4	
Fe171031 FWM	P1	3x			l	r		2	21
	P2	3x				r		1	
	P3	0x						0	
	P4	0x						0	
	p5	3x			l	r	t	3	
	P6	3x			l	r	t	3	
	P7	2x				r	t	2	
	P8	0x						0	
	P9	3x			l		t	2	
	P10	4x			l	r	t	3	
	P11	3x			l	r	t	3	
	P12	3x			l		t	2	

Fe171031 Put	P1	3x		c		r	t	3	35
	P2	4x		c	l	r	t	4	
	P3	4x	b		l	r	t	4	
	P4	4x		c		r	t	3	
	P5	0x						0	
	P6	5x	b		l	r	t	4	
	P7	5x	b	c		r	t	4	
	P8	0x						0	
	P9	5x	b		l	r	t	4	
	P10	5x	b		l	r	t	4	
	P11	1x		c				1	
	P12	5x	b		l	r	t	4	
Fe171031 GP	P1	5X	b		l	r	t	4	34
	P2	5x			l	r		2	
	P3	5x	b		l	r	t	4	
	P4	5x	b		l	r	t	4	
	P5	5x	b		l	r	t	4	
	P6	4x	b		l		t	3	
	P7	5x	b		l	r	t	4	
	P8	0x						0	
	P9	5x	b		l	r	t	4	
	P10	3x	b		l		t	3	
	P11	0x						0	
	P12	4x	b				t	2	
Fe171103 FGM	P1	5x	b		l	r	t	4	45
	P2	5x	b		l	r		3	
	P3	5x	b		l	r	t	4	
	P4	4x	b		l	r	t	4	
	P5	5x	b		l	r	t	4	
	P6	5x	b		l	r	t	4	
	P7	4x	b		l	r		3	
	P8	5x	b		l	r	t	4	
	P9	5x			l	r	t	3	
	P10	5x	b		l	r	t	4	
	P11	5x	b		l	r	t	4	
	P12	5x	b		l	r	t	4	
Fe171103	P1	0x						0	34

FWM	P2	5x		c		r	t	3	
	P3	5x	b		l	r	t	4	
	P4	5x	b		l	r	t	4	
	P5	5x	b	c		r	t	4	
	P6	5x	b		l	r	t	4	
	P7	5x	b		l	r	t	4	
	P8	0x						0	
	P9	5x	b		l	r	t	4	
	P10	5x	b	c		r	t	4	
	P11	0x						0	
	P12	5x	b		l			3	
Fe171103 Put	P1	5x	b		l		t	3	36
	P2	5x		c				1	
	P3	5x				r		1	
	P4	5x		c		r		2	
	P5	5x	b			r	t	3	
	P6	5x	b			r	t	3	
	P7	4x	b	c	l			3	
	P8	5x	b		l	r	t	4	
	P9	5x	b		l	r	t	4	
	P10	5x	b		l	r	t	4	
	P11	5x	b		l	r	t	4	
	P12	5x	b		l	r	t	4	
Fe171103 GP	P1	5x	b		l	r	t	4	48
	P2	5x	b		l	r	t	4	
	P3	5x	b	c		r	t	4	
	P4	5x	b	c		r		4	
	P5	5x	b	c		r	t	4	
	P6	5x	b		l	r	t	4	
	P7	5x	b		l	r	t	4	
	P8	5x	b		l	r	t	4	
	P9	5x	b		l	r	t	4	
	P10	5x	b		l	r	t	4	
	P11	4x	b		l	r	t	4	
	P12	5x	b		l	r	t	4	
Fe180323 FGM	P1	1x				r		1	26
	P2	5x			l	r	t	3	
	P3	5x	b		l	r	t	4	

	P4	5x	b	c		r		3	
	P5	5x	b		l	r	t	4	
	P6	5x	b		l	r	t	4	
	P7	4x	b		l		t	3	
	P8	0x						0	
	P9	4x					t	1	
	P10	5x	b		l	r		3	
Fe180323 FWM	P1	5x	b		l		t	3	14
	P2	0x						0	
	P3	0x						0	
	P4	0x						0	
	P5	0x						0	
	P6	0x						0	
	P7	4x			l	r	t	3	
	P8	5x	b		l	r	t	4	
	P9	5x	b		l	r	t	4	
	P10	5x						0	
Fe180323 Put	P1	0x						0	8
	P2	0x						0	
	P3	0x	b	c	l	r	t	5	
	P4	5x			l	r	t	3	
	P5	0x						0	
	P6	0x						0	
	P7	0x						0	
	P8	0x						0	
	P9	0x						0	
	P10	0x						0	
Fe180323 GP	P1	0x						0	24
	P2	3x					t	1	
	P3	3x	b	c		r		3	
	P4	2x	b		l			2	
	P5	2x	b	c				2	
	P6	4x			l	r	t	3	
	P7	3x			l	r		2	
	P8	5x	b		l	r	t	4	
	P9	4x	b		l	r		3	
	P10	5x	b		l	r	t	4	

Fe180326 FGM	P1	5x	b		l	r	t	4	29
	P2	1x	b					1	
	P3	5x	b		l	r	t	4	
	P4	0x						0	
	P5	5x	b		l	r	t	4	
	P6	5x	b		l	r	t	4	
	P7	5x	b		l	r	t	4	
	P8	5x	b		l	r	t	4	
	P9	0x						0	
	P10	5x	b		l	r	t	4	
Fe180326 FWM	P1	3x	b	c			t	3	35
	P2	5x	b		l	r	t	4	
	P3	4x	b	c		r	t	4	
	P4	5x	b	c		r	t	4	
	P5	5x	b		l	r	t	4	
	P6	5x	b		l	r	t	4	
	P7	5x			l	r	t	3	
	P8	5x				r	t	2	
	P9	5x	b			r	t	3	
	P10	5x	b	c		r	t	4	
Fe180326 Put	P1	0x							22
	P2	0x							
	P3	5x	b		l		t	3	
	P4	5x	b		l	r		3	
	P5	3x	b	c				2	
	P6	5x			l	r	t	3	
	P7	5x	b				t	2	
	P8	5x			l	r	t	3	
	P9	5x	b		l		t	3	
	P10	5x			l	r	t	3	
Fe180326 GP	P1	0X						0	25
	P2	5X	b		l	r	t	4	
	P3	5x	b			r	t	3	
	P4	0x						0	
	P5	0x						0	
	P6	5x	b	c	l	r		4	
	P7	5x	b	c		r	t	4	

	P8	2x		c			t	2	
	P9	5x	b		l	r	t	4	
	P10	5x	b		l	r	t	4	
Fe181126 FGM	P1	5x	b	c	l	r	t	5	37
	P2	5x	b		l	r	t	4	
	P3	5x	b		l	r	t	4	
	P4	2x			l		t	2	
	P5	5x	b		l	r	t	4	
	P6	5x	b		l	r	t	4	
	P7	5x	b		l	r	t	4	
	P8	5x	b		l	r	t	4	
	P9	5x	b		l		t	3	
	P10	5x			l	r	t	3	
Fe181126 FWM	P1	5x						0	35
	P2	5x	b	c	l	r	t	5	
	P3	5x	b		l		t	3	
	P4	5x	b		l	r	t	4	
	P5	5x	b		l		t	3	
	P6	5x	b		l	r	t	4	
	P7	5x	b	c	l	r		4	
	P8	5x	b		l	r	t	4	
	P9	5x	b		l	r	t	4	
	P10	5x	b		l	r	t	4	
Fe181126 Put	P1	5x	b		l	r	t	4	37
	P2	5x	b		l	r	t	4	
	P3	4x			l	r		2	
	P4	5x	b		l		t	3	
	P5	5x	b		l	r	t	4	
	P6	5x	b		l	r	t	4	
	P7	5x	b		l	r	t	4	
	P8	5x	b		l	r	t	4	
	P9	5x	b		l	r	t	4	
	P10	5x	b		l	r	t	4	
Fe181126 GP	P1	5x	b		l	r		3	24
	P2	5x	b		l	r	t	4	
	P3	5x	b		l	r		3	
	P4	5x	b		l	r	t	4	

	P5	5x						0	
	P6	3x						0	
	P7	5x	b		l		t	3	
	P8	5x						0	
	P9	5x	b		l		t	3	
	P10	5x	b		l	r	t	4	
Fe190314 FGM	P1	5x				r	t	2	18
	P2	5x			l		t	2	
	P3	5x	b			r	t	3	
	P4	5x				r	t	2	
	P5	5x				r		1	
	P6	5x						0	
	P7	5x				r	t	2	
	P8	5x	b			r	t	3	
	P9	5x					t	1	
	P10	5x	b				t	2	
Fe190314 FWM	P1	1x	b					1	11
	P2	3x		c	l			2	
	P3	5x						0	
	P4	5x	b					1	
	P5	4x						0	
	P6	4x						0	
	P7	4x	b					1	
	P8	5x	b			r		2	
	P9	5x	b			r		2	
	P10	5x	b				t	2	
Fe190314 Put	P1	5x	b		l		t	3	23
	P2	5x	b			r	t	3	
	P3	5x	b			r	t	3	
	P4	5x	b				t	2	
	P5	5x	b			r	t	3	
	P6	5x	b					1	
	P7	5x	b		l	r	t	4	
	P8	5x					t	1	
	P9	5x					t	1	
	P10	5x				r	t	2	
Fe190314	P1	5x				r	t	2	14

GP	P2	5x	b			r	t	3	
	P3	3x		c	l	r		3	
	P4	5x	b			r	t	3	
	P5	5x			l			1	
	P6	4x						0	
	P7	5x	b					1	
	P8	1x		c				1	
	P9	0						0	
	P10	0						0	
Total									799

Blinded ultrastructural study

In a double-blinded approach, four different people rated every sample. The questionnaire used for the evaluation of ultrathin-sections can be found in Table 17 and for semi-thin sections in Table 18.

Table 17: Questionnaire for evaluation of ultra-thin sections

No	Questions ultra-thin	Answers				Good	bad
UD1	Is the sample evaluable?	Yes	No			2	1
UD2	Are knife marks visible?	Yes	No			1	2
UD3	Are there many holes in the resin (quality)?	1 no holes	2 some holes	3 many holes		1	3
UD4	Are there freezing damages (ice crystals)?	1 no ice crystals	2 some ice crystals	3 many ice crystals		1	3
UD5	Are there any contrast agent deposits?	1 no deposits	2 some deposits	3 many deposits		1	3
UD6	Can cell nuclei be seen?	Yes	No			2	1
UD7	Can myelin sheaths be seen?	Yes	No			2	1
UD8	Are blood vessels available?	Yes	No			2	1
UD9	Are lamellae of the myelin sheaths recognizable?	Yes	No			2	1
UD10	Are holes in myelin sheaths visible?	Yes	No			2	1
UD11	Myelin sheaths are majority	1 intact	2 partly disbanded	3 mostly disbanded		1	3
UD12	The condition of the chromatin is?	1 Hetero-chromatin fine crumbly	2 crumbly	3 chromatin coarse cloddy		1	3
UD13	The condition of the mitochondria is?	1 Cristae, double membrane intact	2 swollen, not that dense	3 serve swollen	4 no cristae visible	1	4
UD1	The condition of the blood vessels is?	1	2	3		1	3

4		endotheli a visible	endothel ia disbande d	cell borders disbande d			
UD1 5	The condition of the ER is?	1 normal	2 extended	3 not visible		1	3
UD1 6	Are there many empty areas/washouts?	1 no	2 few	3 some	4 many	1	4
UD1 7	Is glycogen recognizable?	Yes	No			2	1
UD1 8	Are free ribosomes recognizable?	Yes	No			2	1
UD1 9	Are lysosomes present?	Yes	No			1	2
UD2 0	Are vacuoles visible in the cytoplasm?	Yes	No			1	2
UD2 1	Are phagosomes visible?	Yes	No			1	2
UD2 2	Are autophagosomes visible?	Yes	No			1	2
UD2 3	Are autolysosomes visible?	Yes	No			1	2
UD2 4	Are telolysosomes/residual bodies visible?	Yes	No			1	2
UD2 5	Overall assessment of lysis?	1 no lysis	2 some lysis	3 much lysis		1	3
UD2 6	Is the synaptic cleft recognizable?	Yes	No			2	1
UD2 7	Are vesicles recognizable?	Yes	No			2	1
UD2 8	Is a postsynaptic condensation visible?	Yes	No			2	1
Sum						39	57

Table 18: Questionnaire for evaluation of semi-thin sections

No	Questions semi-thin	Answers				Good	bad
SD1	Is the sample evaluable?	Yes	No			2	1
SD2	Are knife marks visible?	Yes	No			1	2
SD3	Are processing damages to be recognized?	Yes	No			1	2
SD4	Can cell nuclei be seen?	Yes	No			2	1

SD5	Can myelin sheaths be seen?	Yes	No			2	1
SD6	Are blood vessels available?	Yes	No			2	1
SD7	Are there many empty areas / washouts?	1 no	2 few	3 some	4 many	1	4
SD8	Are there gaps around cell bodies?	1 no	2 few	3 some		1	3
SD9	Overall assessment lysis?	1 no lysis	2 some lysis	3 much lysis		1	3
SD10	Processing problems? (Resin problems, fixation gradient, dehydration)	1 no	2 few	3 some		1	3
Sum						14	21

CellProfiler™ pipeline

The CellProfiler™ pipeline, which was used for the identification and automatic counting of the iron particles in the EFTEM images, is described in detail in Table 19.

Table 19: The detail description of the pipeline with the values for every step.

Step	Step Name	Input	Output	Filter Method to distinguish	Object	Dimensions	Operation	Multi-player	Threshold	Smoothing scale Correction factor Lower upper bounds	format
	NamesandTypes	Images	MAP								
1	Smooth	MAP	Smooth_IMG	Gaussian		5 px					
2	Smooth	MAP	Smooth_IMG_10	Gaussian		10 px					
3	Smooth	MAP	Smooth_IMG_30	Gaussian		30 px					
4	ImageMath	Smooth_IMG Smooth_IMG_30	IMG_WO_BG				Subtract	1.0 1.0			
5	IdentifyPrimaryObjects	IMG_WO_BG	Ferritin_OBJ	Intensity		Min 8 px, Max 15 px			Adaptive Otsu Two classes	1.3488 1.0 0.2, 1.0 50	
6	MeassureObjectSizeShap	Ferritin_OBJ									

	e										
7	FilterObjects	Ferritin_OBJ	Ferritin_filtered_OBJ	Measurement		Min 7, Max 30	AreaShape MinFeretDiameter				
8	ExpandorShrinkObjects	Ferritin_filtered_OBJ	Ferritin_centerpoints				Shrink objects to a point				
9	ConvertObjectstoImage	Ferritin_centerpoints	Centerpoints								Binary
10	MeassureObjectSizeShape	Ferritin_filtered_OBJ									
11	ImageMath	Smooth_IMG_10 Smooth_IMG_30	Smooth_WO_BG					1.0 0.8			
12	IdentifySceondaryObjects	Smooth_WO_BG	Ferritin_centerpoints	Watershed Image	Ferritin				Adaptive Otsu Two classes	0 1.0 0.14, 1.0 100	
13	ConvertObjectstoImage	Ferritin	Ferritin_IMG								Binary
14	IdentifyPrimaryObjects	Ferritin_IMG			Ferritin_OBJ_BIG	Min10 px, Max 40 px			Global Manual 0.001		
15	MeassureObjectSizeShape	Ferritin_OBJ_BIG									
16	FilterObjects		Ferritin_filtered_O	Measurement	Ferritin_OBJ_	Min	AreaShape				

			BJ_BIG		BIG	30, Max 1000	MaxFretDiameter				
17	MeassureObjectSizeShape				Ferritin						
18	FilterObjects		Ferritin_final	Measurement	Ferritin	Min 0.8, 7 Max 25	AreaShape Eccentricity MaxFretDiameter MinFretDiameter				
19	MaskObjects	Ferritin_filtered_OBJ_BIG	Ferritin_WO		Ferritin_final						
20	MeasureObjectIntensity	Smooth_IMG	Ferritin_WO								
21	ExpandorShrinkObjects		Ferritin_WO_Expand				Expand objects by a specified number of pixels, 5				
22	MeasureObjectIntensityDistribution	MAP			Ferritin_WO_Expand Center: Ferritin_WO	Max Zernike 9					
23	FilterObjects	Image: Smooth_IMG	Ferritin_intense	Measurement Limit MeanIntensity	Ferritin_WO	Min 0.33					
24	FilterObjects	Image: MAP Ferritin_WO_Expand	Ferritin_Expand_filtered	Measurement Limit RadialDistrib		Min 0.015 Scale 4_0					

				ution ZernikeMagnitude							
25	MaskObjects	Ferritin_intense Ferritin_Expand_filtered	Ferritin_corrected								
26	OverlayOutlines	Image: MAP		Overlay	Ferritin_final Ferritin_centerpoints Ferritin_intense Ferritin_corrected						
27	DisplayDataOnImage	Ferritin_WO_Expand Image: MAP	Overlay_Data	RadialDistribution ZernikeMagnitude		Scale 4_0					
28	SaveImage	MAP	MAP_orig								
29	SaveImage	Overlay_Data	MAP_overlay								
30	ConvertObjectsToImage	Ferritin_corrected	Ferritin_object_IMG								Binary
31	SaveImage	Ferritin_object_IMG	MAP_binary								
32	ExportToSpreadsheet										

Manual for EFTEM acquisition

- **General**
  - Load the samples into the TEM
  - Aperture from 100 µm to 200 µm
  - Microscope setting: 200 kV, Emission 3
  - Load alignments for 200 kV
  - Do daily alignments in EFTEM Mode and with Emission 1 and cooking
  - Save position of a hole in the sample (for EFTEM tuning and illumination threshold)

- **Get points of acquisition**
  - Select LM 75x magnification
  - Check if Camera is **not** inserted
  - Start SerialEM and open project
  - Setup cooker: Task-> Setup cooker-> Expose for time 30 min-> **Close** (NOT go!)
  - Open Navigator
  - Check settings for camera (View and Record)
  - Make **Corner Map** of section
    - Add points
    - Set corner points at the edges of ultra-thin section
    - Assign "C" to corner points in navigator and save navigator
    - Start corner montage (Navigator-Grid montage-setup corner montage)
  - Choose add **Polygon** in Navigator
    - Outline the section
    - Choose "add grid of point" in navigator (distance between points 10 µm)
  - **Shift** to marker
    - Choose prominent feature and "add Point"
    - Find prominent feature in SA magnification
    - Record in SerialEM
    - Mark position in the new picture (left click)
    - Navigator "Shift to marker"
    - Magnification back to 75x
  - Script
    - Number of all grid points
    - Number of acquisition points (**10**)
    - Check illumination and remember value (first hole, tissue, ¼ grid -> control in DM)
    - Enter threshold illumination value (first hole-tissue, then tissue-grid)
    - Wait until the points are selected and then you can review them and **save positions**
    - Cooking of samples starts

- **Tuning of GIF Filter**
  - Operate the microscope at RT
  - Switch to EFTEM mode in TIA/DM and select CCD Camera in DM
  - User Mode: DM-HELP-user mode-Power user
  - Filter control: DM-Window-Floating Window-GIF Quantum SE control-Filter Control (Slit with should be 10 eV, sometimes it is 1 eV), AutoFilter Window
  - Board Error: Ignore Error message!
  - Go to the hole in the sample for GIF tuning
  - Spot size 2 and C2 48 %, exposure 0.2 sec
  - Choose magnification for EFTEM (80'000x) and beam should be positioned at ~ 7 o'clock Focus beam carefully until the edges can be seen and centre the beam in the image
  - Align Zero loss peak
  - Tuning: Properties- (check everything available)- Full tune

- **EFTEM elemental analysis**
  - Realign ZLP every 4 points
  - Move to the first acquisition point, Emission 3
  - Focus in bright field
  - Focus: Energy loss at 60 eV, slit 40 eV, exposure time at 0.4 sec and binning 4
  - Centre beam: 600 eV, slit 40 eV and centre the beam in the image
  - Start view and focus image
  - Get elemental map with elemental specific settings:
    - Fe L-edge (measurement): Post: 718 eV, Pre1: 633 eV, Pre2: 673 eV, Slit 40 eV,
      Exposure 30 s, Binning: 2x, Sum: 1
  - Repeat measurement for all shifted point (at each acquisition point (10) 4 further images should be done, follow the script)
  - Bright field image at 80'000x
  - Repeat measurement for all acquisition points

- **BF montages of points**
  - do 3x3 montages at 6500x magnification for each acquisition point

SerialEM Script for EFTEM

```
#########################################################################
########################################
#macro for EFTEM aquisition with SerialEM in combination with Digital
Micrograph (Gatan, Inc.)
#########################################################################
########################################
# Stefan Wernitznig, Daniel Kummer, Mariella Sele, Medical University
Graz, Austria
# Anna-Sophie Wittgenstein, Graz University of Technology, Austria
ScriptName EFTEMSerialEM V_4_tested_aquisition_May_2019 Mariella
#########################################################################
########################################
# Build Global Variables

Verbose 1

Pause ATTENTION! Insert Objective lense!-------------EFTEMSerialEM V_4---
----------

montageMagnification = 8000
overviewMagnification = 20000
eftemMagnification = 80000
detectionMagnification = 10000
cookingMagnification = 5000

EnterOneNumber Number of NavItems in the Navigator(Polygon):
count = $ReportedValue1
randomlistcount = $count - 1

EnterOneNumber Enter number of Items before the grid points:
gridshift  = $ReportedValue1

EnterOneNumber Number of Positions for Image Aquisition:
subsetcount = $ReportedValue1

ratio = $count / $subsetcount
If ( $ratio < 3 )
      Pause Set of NavItems too small for selected !!!
      Exit
Endif

UserSetDirectory Choose Working Directory
#SetDirectory $ReportedValue1

EnterOneNumber Do You want to measure illumination threshold for GRID
detection?(1 for Yes 0 for No)

if ( $ReportedValue1 == 1)
      SetMag $detectionMagnification
      SelectCamera 1
                        Pause Move Stage to a Position with a hole
      R
      ImageProperties A recXsize recYsize
      ReportMeanCounts A
      holeMean = $repVal1
      Pause $holeMean
      Pause Move Stage to a Position without a Grid
      R
```

```
      ImageProperties A recXsize recYsize
      ReportMeanCounts A
      nogridMean = $repVal1
      Pause $nogridMean
      Pause Move Stage to a Position with a quarter covered by the Grid
      R
      ImageProperties A recXsize recYsize
      ReportMeanCounts A
      gridMean = $repVal1
      Pause $gridMean
      EnterOneNumber Set upper illumination threshold for GRID detection:
    upthreshold = $ReportedValue1
    EnterOneNumber Set lower illumination threshold for GRID detection:
    lowthreshold = $ReportedValue1
else
EnterOneNumber Set upper illumination threshold for GRID detection:
upthreshold = $ReportedValue1
EnterOneNumber Set lower illumination threshold for GRID detection:
lowthreshold = $ReportedValue1
SetMag $detectionMagnification
SelectCamera 1
endif

#*************************************************************************
****************************************
# Loop through Nav Items measure Mean illumination and build array of
accepted positions


poscounter = 0
Loop $subsetcount

      Loop $count
            random = RAND
            randomposition = NEARINT ($random * ($count - 1)) + 1 +
$gridshift

            IsVariableDefined positionlist

            if ( $ReportedValue1 == 0 )
                  positionlist = { $randomposition }
            else
            alreadypicked = 0
                  Loop $#positionlist loopcounter
                        if      (      $positionlist[$loopcounter]      ==
$randomposition )
                              alreadypicked = 1
                              Break
                        Endif
                  EndLoop
                  if ( $alreadypicked == 0 )
                        positionlist = { $positionlist $randomposition }
                  else
                        Continue
                  Endif
            Endif

            MoveToNavItem $randomposition
                                          R
                                          ImageProperties   A   recXsize
recYsize
```

```
                                          ReportMeanCounts A
            refMean = $repVal1

            if ( $refMean > $lowthreshold AND $refMean < $upthreshold  )
                  IsVariableDefined acceptedpositionlist
                  if ( $ReportedValue1 == 0 )
                        acceptedpositionlist = { $randomposition }

poscounter = 1
                  else
                        acceptedpositionlist   =   {$acceptedpositionlist
$randomposition}

poscounter = $poscounter + 1
                  Endif
                  Break
            Endif
            echo    ------------------------    ACCEPTED    POSITIONS    :
$poscounter  ----------------------------------

                     EndLoop

EndLoop

echo $acceptedpositionlist
echo $positionlist

#*************************************************************************
****************************************
# Check Accepted positionlist

Pause  Check  the  accepted  Positions  and  save  them  to  the  TIA  User-
Interface?

      Loop $subsetcount checkloopcount
            MoveToNavItem $acceptedpositionlist[$checkloopcount]
                R
            Pause       Position       $checkloopcount       Nav       Item
$acceptedpositionlist[$checkloopcount] and save to TIA User-Interface!!!
      EndLoop

#EnterOneNumber Do you want to redefine Positions?
#if ( $ReportedValue1 == 1)
#     CallFunction PickPositions
#     CallFunction CheckPositions
#endif


#*************************************************************************
****************************************
# Cook Accepted positionlist

Pause Are you ready to start Specimen Cooking?

SetMag $cookingMagnification

Loop $subsetcount cookloopcount

      MoveToNavItem $acceptedpositionlist[$cookloopcount]

                     SetPercentC2 51
```

```
      AutocenterBeam
      CookSpecimen

EndLoop

#*************************************************************************
****************************************
# engage  microscope sleepmode

RetractCamera
ScreenDown
SetColumnOrGunValve 0

Pause Are you ready to start EFTEM Aqusition?
SetColumnOrGunValve 1
ScreenUp

#*************************************************************************
****************************************
# Aquire images of Accepted positionlist

SetMag $eftemMagnification
RetractCamera
SelectCamera 2

Pause Please check EFTEM Tuning

Loop $subsetcount aquisitionloopcount

      Pause       Moving       to       Position       $aquisitionloopcount
$acceptedpositionlist[$aquisitionloopcount]
      MoveToNavItem $acceptedpositionlist[$aquisitionloopcount]
                     Pause Aquire center EFTEM Image in DM and continue
      MoveToNavItem $acceptedpositionlist[$aquisitionloopcount]
                              MoveStage 0 0.6
                              Pause  Aquire  top  EFTEM  Image  in  DM  and
continue
      MoveToNavItem $acceptedpositionlist[$aquisitionloopcount]
                              MoveStage 0 -0.6
                              Pause Aquire bottom EFTEM Image in DM and
continue
      MoveToNavItem $acceptedpositionlist[$aquisitionloopcount]
                              MoveStage -0.6 0
                              Pause  Aquire  left  EFTEM  Image  in  DM  and
continue
      MoveToNavItem $acceptedpositionlist[$aquisitionloopcount]
                              MoveStage 0.6 0
                              Pause  Aquire  right  EFTEM  Image  in  DM  and
continue
EndLoop


#*************************************************************************
****************************************
# Aquire Montage of Accepted positionlist


#SetMag $montageMagnification
#SelectCamera 1

Loop $subsetcount aquisitionloopcount
```

```
echo Montage Position $aquisitionloopcount : NavigatorItem $acceptedpositionlist[$aquisitionloopcount]

EndLoop

Pause FINISHED, Please aquire Montages manually!
```